MASTER THESIS

HØGSKOLEN
I ÅLESUND

Aalesund University College

TITLE:
CFD Investigation in Scale Effects on Propellers with Different Blade Area Ratio

CANDIDATE NAME:
Zicheng Chen

DATE:	COURSE CODE:	COURSE TITLE:	RESTRICTION:
29/5/2015	IP501909	MSc Thesis	

STUDY PROGRAM:	PAGES/APPENDIX:	LIBRARY NO.:
MSc-Ship Design	63/3	

SUPERVISOR(S):
Karl Henning Halse

ABSTRACT:

The performance prediction of marine propulsor has long been assessed by means of model test. Due to the larger difference in Reynolds number between model and full scale, the traditional extrapolation of measured force to full scale may be questionable, which implies knowledge investment into the scale effect on propellers. In the report, a number of propellers with blade area ratio variation were analyzed systematically by a RANSE method, the obtained numerical results agreed with the towing tank test fairly well. Parts Based Meshing technique is utilized for the highly automated mesh generation in model and full scale. The concerning scale effects due to blade area ratio variation are demonstrated and explained by comparing open water characteristics including thrust, torque, and pressure distribution, etc. The study indicates that trailing edge radial flow behavior contributes a lot to the propeller scale effect.

PREFACE

This report is the result of my Master's thesis project for the two-year MSc program Ship Design at Ålesund University College (HIÅ).

The motivation for me to cover this topic is to fully develop the capability of dealing with marine engineering problems with the state-of-the-art CFD (Computational Fluid Dynamics) tools. In this report, a number of systematically varied propellers were analyzed numerically and validated against experimental results, with primary focus on the problem of scale effect.

This MSc thesis is originated from the research project PROPSCALE (Full Scale Performance Prediction for Energy Efficient Ship Design), 2013-2016. Led by MARINTEK, the project involves research partners including CSSRC, NTNU, HIÅ and TUHH, in collaboration with the leading Norwegian industrial partners like Rolls-Royce Marine AS, etc. Its primary objective is to acquire theoretical knowledge and develop practical methods for the accurate prediction of vessels equipped with novel energy efficient propulsion systems in full scale, and to quantify scale effect on propulsive characteristics of these vessels through the development and application of CFD methods.

I wish to express my sincere gratitude to my supervisor, Professor Karl Henning Halse, for providing suggestion and help throughout the project. I am also very grateful to Dr. Vladimir Krasilnikov, manager of the project PROPSCALE. Maine application of CFD method requires large amount of best practices, I have greatly benefited from his generous support and valuable comments during the research.

Ålesund, May 25, 2015.

Zicheng Chen

ABSTRACT

The performance prediction of marine propulsor has long been assessed by means of model test. Due to the larger difference in Reynolds number between model and full scale, the traditional extrapolation of measured force to full scale may be questionable, which implies knowledge investment into the scale effect on propellers. In the report, a number of propellers with blade area ratio variation were analyzed systematically by a RANSE method, the obtained numerical results agreed with the towing tank test fairly well. Parts Based Meshing technique is utilized for the highly automated mesh generation in model and full scale. The concerning scale effects due to blade area ratio variation are demonstrated and explained by comparing open water characteristics including thrust, torque, and pressure distribution, etc. The study indicates that trailing edge radial flow behavior contributes a lot to the propeller scale effect.

Keywords
Propeller, Scale effect, Blade area ratio, RANSE

Tables of contents

TERMINOLOGY

Symbols

Γ	Circulation
β_i	Section hydrodynamic pitch angel [deg]
T	Propeller thrust [N]
Q	Propeller torque [N · m]
ε	Lift to Drag ratio
Z	Number of blades
η_0	Propeller efficiency
D	Propeller diameter [m]
n	Propeller rotational speed [Hz]
V_A	Advance speed [m/s]
ρ	Water density [kg/m³]
μ	Water dynamic viscosity [Pa·s]
υ	Water kinematic viscosity $[\text{m}^2 \cdot \text{s}^{-1}]$
K_T	Propeller thrust coefficient
K_T	Propeller torque coefficient
J	Advance Coefficient
Re	Reynolds number
div	Vector operator
$\vec{U}$	Velocity vector
ϕ	General scalar conserved property
f_o	Maximum section camber
x_r	Propeller section rake
b_r	Chord length
e_o	Max thickness
T_s	Propeller section skew
C_p	Pressure Coefficient
$\zeta_x, \zeta_y, \zeta_z$	Vorticity component in three direction
δ	Boundary layer thickness [m]

Abbreviations

BAR	Blade area ratio
DNS	Direct Numerical Simulation
LES	Large eddy simulation
RANS	Reynolds Averaged Navier-Stokes
CPP	Controllable pitch propeller
FPP	Fixed pitch propeller
TKE	Turbulent kinetic energy
CFL	Courant number

1. INTRODUCTION

The global shipping transportation has been increased significantly in the past decades. This raises significant concerns in the society regarding the environmental impact of sea operations. As a result, the shipbuilding industry is facing an ever more challenging regulatory leading to drastic reductions of emissions of pollutants. Therefore, it requires further development of new energy efficient designs of vessels and propulsion systems. This, in its turn, requires accurate prediction of vessels equipped with novel energy efficient propulsion systems in full scale.

Nowadays, the performance prediction of propulsion system is still mainly based on the results of towing tests, open water tests and self-propulsion tests in model scale. Due to the larger difference in Reynolds number between model and full scale, the traditional extrapolation procedure may be inadequate to capture the scale effect on characteristics of propellers, which can be extremely complicated by propeller geometry and the interaction among blades, duct and hull structure in some cases.

In recent years, significant progress has been made in the scale effect on marine propulsor by means of CFD methods. Krasilnikov et al. [1], has studied the influence of blade skew on scale effect using FLUENT solver with the SST k-ω model. Investigations on the scale effect of ducted propellers was carried out in Abdel-Maksoud et al. [2] and Krasilnikov et al. [3].

In the present study, numerical simulation with systematically varied propellers are performed in the commercial code STAR-CCM+, which solves RANS equations in their integral form, by means of Finite Volumes methods. Highly automatically mesh generation is also realized, due to the Parts Based Operation functionality in STAR-CCM+. The numerical simulation is performed as implicit unsteady, velocities and pressures are solved in a segregated flow, and then coupled by means of the SIMPLE algorithm. SST k-ω turbulence model is selected for its better performance compared to other two-equation models when boundary layer flow is under adverse pressure gradients (e.g. separation), which is expected under heavy loading condition.

Scale effect on propeller open water characteristics were studied in this project, nevertheless open water characteristics are not always sufficient for an adequate propeller design which should account for the interaction between propeller and ship hull, however this is not addressed in this paper. When applying CFD methods with assumption of fully turbulent flow to predict propeller performance in model scale, one should be aware that laminar flow zone can exist during model test, this will contribute to the difference between numerical and experimental results. It requires more advanced transition model to capture this effect. When applying the numerical results in full scale to practice use, one has to take consideration of roughness effects. Besides, other effects like propeller cavitation has a considerable impact on the propeller performance under certain conditions, this requires additional investigation in future.

2. BACKGROUND AND THEORETICAL BASIS

The propeller, whose name comes from the Latin "propellare" (to drive forward) is a very old idea. It was however at the beginning of the 19th century, when a suitable power source-the steam engine-was developed that an efficient screw propeller was produced, AB Volvo Penta [4]. Most marine vessels are fitted with propulsor to overcome resistance as it moves forward. Meanwhile, operations like maneuvering and station-keeping also require this kind of robust driving source.

2.1 Propeller theory
2.1.1 Working Principles
A propeller creates pulling power by moving water and creating a column of water behind it. Hence, the accelerated water will generate a counterforce on the blade, which forms the so-called blade force. As shown in Fig.2.1, the propeller's blade force which is caused by the pressure difference between the blade's pressure and suction side, can be split into two parts. Axial component makes up the thrust, and the other tangential component constitutes the torque. The thrust and torque in their non-dimensional form are among the most important values describing the propeller's performance.
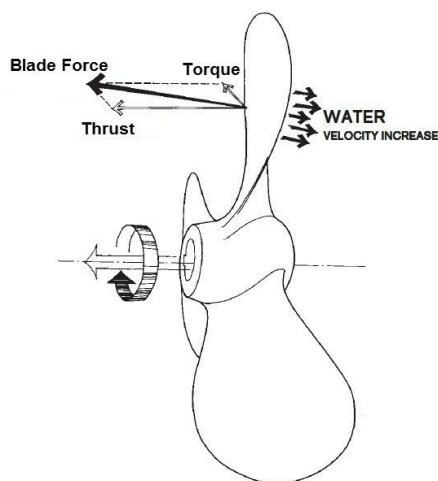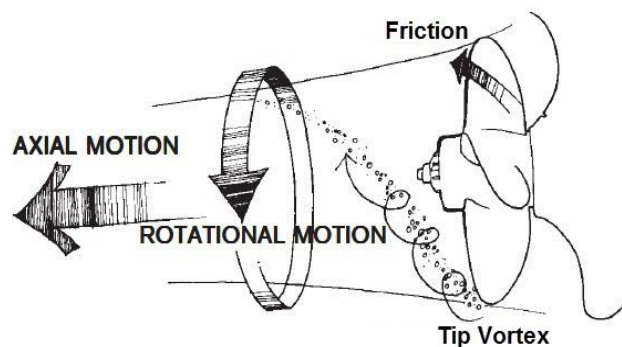

Figure 2.1 Blade force diagram   **Figure 2.2 Water column in propeller slipstream**

Behind the propeller, the increased water cylinder moves both axially (equivalent to the propeller's thrust) and in a rotational direction (equivalent to the propeller's torque). Hence, the water cylinder or column has a kinetic energy. See Fig.2.2. The kinetic energy in the outgoing column is an important part of the propeller's energy diss. Other losses are friction when the blades cut through the water, flow separation due to vortex and cavitation bubbles at the blade.

There are several terminologies to define the propeller's characteristics such as: diameter, pitch, blade area ratio, rake, skew etc. All these characteristics are calculated and optimized to design the propeller accordingly to specific needs of the customer and the ship characteristics. The propeller's blade area ratio BAR is a parameter used to relate the size of a blade to its diameter, see Figure 2.3. It is a term used to denote the ratio of expanded area A_E to disc area A_o. If one knows the blade width at 70% of the propeller radius then the blade area ratio is expressed as:

$$BAR = \frac{A_E}{A_o} = 0.43 \times No.\,blades \times \frac{Blade\ width}{Diameter} \qquad (2.1.1)$$

BAR is critical to the control of cavitation and changes of BAR affect propeller's efficiency a lot. In the present paper, three types of propellers with systematically varied BAR will be investigated.
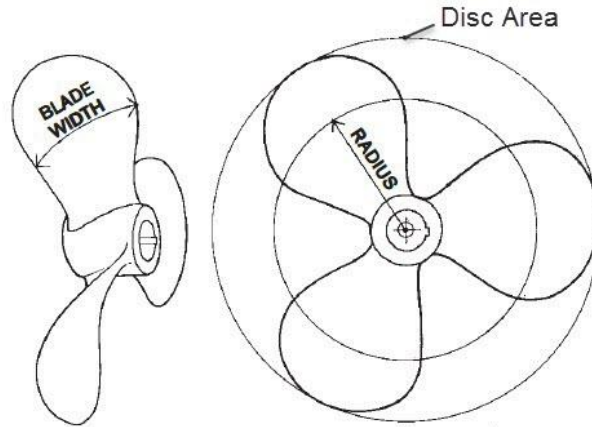

Figure 2.3 Blade area and disc area

2.1.2 Blade element theory

Blade element theory is a mathematical process originally designed to determine the behavior of propellers. It involves breaking a blade down into several small sections then determining the forces on each of these small blade elements.

The lift force generated on each blade section due to the pressure differential on the suction and pressure side of propeller, can be derived from the famous Kutta–Joukowski theorem:

$$dL = \rho V_R \Gamma_{(r)} dr \qquad (2.1.2)$$

where Γ is the circulation, V_R is the flow velocity. At the same time, there will be a drag force with the direction normal to the lift force and coincident with incoming flow. The Drag component is caused by viscosity and will be affected greatly by Reynolds number. According to blade element theory, a typical propeller blade section at the radius *r* and the corresponding velocity diagram are shown blow.
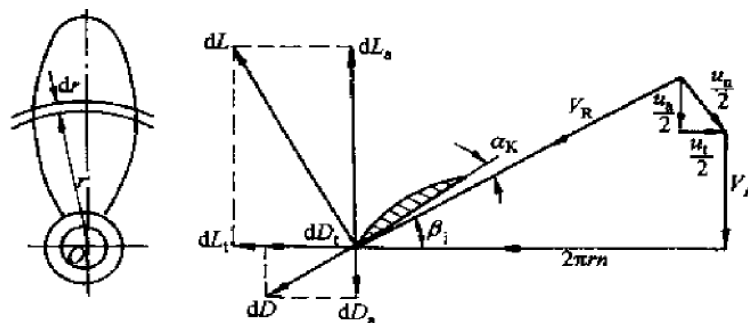

Figure 2.4 Blade element theory

From the plot, one can easily find the lift force d_L and drag force d_D with their components in axial and tangential direction. The resulting thrust and torque can be expressed as:

$$dT = dL_a - dD_a = dL\cos\beta_i - dD\sin\beta_i \qquad (2.1.3)$$
$$dF = dL_t + dD_t = dL\sin\beta_i + dD\cos\beta_i \qquad (2.1.4)$$

where $dL = \rho V_R \Gamma_{(r)} dr$, β_i is the section hydrodynamic pitch angel. The related torque for the blade section $dQ = rdF$. Finally, the total thrust of the propeller will be the integration of axial lift vectors for the sections from root to tip.

$$T = Z \cdot \int_{r_H}^{R} F_L \cdot \cos \beta_i \cdot (1 - \varepsilon \tan \beta_i) \cdot dr \qquad (2.1.5)$$

$$Q = Z \cdot \int_{r_H}^{R} F_L \cdot \sin \beta_i \cdot (1 + \varepsilon \cot \beta_i) \cdot r \cdot dr \qquad (2.1.6)$$

where ε is the lift to drag ratio, $\varepsilon = F_D/F_L$ and Z is the number of blades.

When propeller is operating at the advance speed of V_A with rotational speed of n, the effective power is $T \cdot V_A$, and the received power from engine is defined as $2\pi nQ$. Therefore propeller efficiency is :

$$\eta_0 = \frac{TV_A}{2\pi nQ} \qquad (2.1.7)$$

2.1.3 General open water characteristics

As we may know, the thrust and torques produced by the propeller are expressed in their most fundamental form in terms of a series of non-dimensional characteristics. To establish these expressions, the principle of dimensional similarity can be applied to geometrically similar propellers. One can imagine, the hydrodynamic performance (thrust and torque) of a propeller is depend upon the following parameters:

(a) The propeller diameter (*D*).

(b) The rotational speed (*n*).

(c) The speed of advance (*V_A*).

(d) The density of the fluid (*ρ*).

(e) The dynamic viscosity of the fluid (*μ*).

(f) The gravity (*g*).

Therefore, the thrust (*T*) can be assumed to be proportional to *D, n, V_A, ρ, μ* and *g*.

$$T = kD^a \, n^b \, V_A^{\ c} \, \rho^d \, \mu^e \, g^f \qquad (2.1.8)$$

where *k* is proportional coefficient, and *a, b, c, d, e, f* are unknown index.

Since the above equation must be dimensionally correct, and the parameters involved can be replaced by equating indices for M (mass), L (length) and T (time).

$$\frac{ML}{T^2} = kL^a \; (\frac{1}{T})^b \; (\frac{L}{T})^c \; (\frac{M}{L^3})^d \; (\frac{L^2}{T})^e \; (\frac{L}{T^2})^f \qquad (2.1.9)$$

From the above

$$\left.\begin{array}{l} M: \; 1 = d \\ L: \; 1 = a + c - 3d + 2e + f \\ T: \; -2 = -b - c - e - 2f \end{array}\right\} \rightarrow \left.\begin{array}{l} d = 1 \\ a = 4 - c - 2e - f \\ b = 2 - c - e - 2f \end{array}\right\} \qquad (2.1.10)$$

Further

$$T = kD^{4-c-2e-f} \, n^{2-c-e-2f} \, V_A^{\ c} \, \rho^1 \, \mu^e \, g^f = k\rho n^2 D^4 (\frac{V_A}{nD})^c (\frac{\upsilon}{nD^2})^e (\frac{gD}{n^2D^2})^f \qquad (2.1.11)$$

One more universal format of the above equation is

$$T = \rho n^2 D^4 \cdot f_1(\frac{V_A}{nD}, \frac{nD^2}{\upsilon}, \frac{n^2D^2}{gD}) \qquad (2.1.12)$$

These non-dimensional groups are known by the following:

Thrust coefficient K_T

$$K_T = \frac{T}{\rho n^2 D^4} = f_1(\frac{V_A}{nD}, \frac{nD^2}{\upsilon}, \frac{n^2 D^2}{gD})$$

(2.1.13)

where $\frac{V_A}{nD}$ is the advance coefficient J, $\frac{nD^2}{\upsilon}$ and $\frac{n^2 D^2}{gD}$ are Reynolds number Re and Froude number

Fr respectively.

From experience, when a marine propeller is working sufficiently far away from the free surface so as not to cause surface waves, the influence of Froude number on propeller thrust can be ignored. In conclusion, if the propeller is submerged deeply enough, the open water characteristics are depend only upon advance coefficient J and Reynolds number Re.

$$K_T = f_1(J, Re)$$

(2.1.14)

2.1.4 Propeller Scale effects

To be able to accurately predict a ship's the propulsion efficiency, a good understanding of scale effects is a prerequisite. Traditionally, prediction of open water characteristics of a propeller design has been assessed by model scale tests. The experimental methodology is based on the similarity theory, which postulates that two propellers with geometric and dynamic similarity will have the identical hydrodynamic characteristics. The premise of dynamic similarity requires the equivalence of advance coefficient J, and Reynolds number Re of the target two propellers.

Assuming $V_{As}, n_s, D_s, \upsilon_s$ an $V_{Am}, n_m, D_m, \upsilon_m$ represents the advance speed, rotational speed, diameter and dynamic viscosity of the fluid of the full-scale and mode-scale propeller respectively. λ is the scale factor and $\lambda = D_s/D_m$.

To keep J and Re to be identical for model and full scale propeller, two equations must be fulfilled at the same time.

$$\left.\begin{array}{l} \frac{V_{Am}}{n_m D_m} = \frac{V_{As}}{n_s D_s} \\ \frac{n_m D_m^2}{\upsilon_m} = \frac{n_s D_s^2}{\upsilon_s} \end{array}\right\}$$

(2.1.15)

Obviously, the requirements above can't be realized in reality due to the unrealistic rotational speed and advance speed for the model propeller. Hence, in model test only the advance coefficient J is kept identical, whilst $R_e > R_{ec}$.

The different propeller performance characteristics between model and full scale resulted from different Reynolds number, is so-called scale effects.

2.1.5 Scaling method

The scale effects affecting performance characteristics are essentially viscous in nature, and as such are primarily due to boundary layer phenomena dependent on Reynolds number. Due to the methods of testing model propellers and the consequent changes in Reynolds number between model and full scale, there can arise a different boundary layer structure to the flow over the blades. Whilst it is generally recognized that most full-scale propellers will have a primarily turbulent flow over the blade

surface this need not be the case for the model where characteristics related to laminar flow can prevail over significant parts of the blade. In order to quantify the effect of scale on the performance characteristics of a propeller, the 1978 ITTC recommended scaling procedure is presented.

$$\left.\begin{array}{l} K_{T_s} = K_{T_m} - \Delta K_T \\ K_{Q_s} = K_{Q_m} - \Delta K_Q \end{array}\right\}$$

(2.1.16)

where the scale corrections ΔK_T and ΔK_Q are given by

$$\Delta K_T = -0.3\Delta C_D(\frac{P}{D})(\frac{cZ}{D})$$

(2.1.17)

$$\Delta K_Q = 0.25\Delta C_D(\frac{cZ}{D})$$

(2.1.18)

The term ΔC_D relates to the change in drag coefficient introduced by the differing flow regimes at model and full scale, and is formally written as

$$\Delta C_D = C_{Dm} - C_{Ds}$$

(2.1.19)

where

$$C_{Dm} = 2\left(1 + \frac{2t}{C}\right)\left[\frac{0.044}{R_{nx}^{1/6}} - \frac{5}{R_{nx}^{2/3}}\right]$$

(2.1.20)

$$C_{Ds} = 2\left(1 + \frac{2t}{C}\right)\left[1.89 + 1.62\log_{10}(\frac{c}{K_p})\right]^{-2.5}$$

(2.1.21)

In these relationships *t/c* is the section thickness to chord ratio; P/D is the pitch ratio; c is the section chord length and R_{nx} is the local Reynolds number, all relating to the section located 0.75R. The blade roughness K_p is taken as 30×10^{-6}m.

It is well acknowledged that the ITTC-procedure method can provide a reliable and practical solution to propeller testing. However, the ITTC-procedure is unable to consider the local flow condition. In the meantime, it do not reflect correctly the effect of Reynolds number on propeller characteristics, in particular, as far as high skew and balanced skew propeller designs are concerned.

2.2 CFD introduction

Computational fluid dynamics, or CFD, is a computational technology that enables scientists and engineers to perform numerical experiment in a virtual laboratory. It employs numerical methods and algorithms to solve the equations that describe fluid flow. CFD method has being widely applied in marine industry for the prediction of ship performance in waves, design and analysis of propulsion system, investigation on behaviors of floating structure, as well as for many other applications. For the study of scale effects on marine propellers, CFD method can provide an insight into detailed flow patterns that are difficult, expensive or impossible to study using traditional experimental techniques. Before the investigation, it is necessary to introduce the underlying physical problems and mathematical principles employed by the CFD method.

2.2.1 Governing equation

The equations that describe the dynamics of fluid represent fundamental laws of physics stating conservation of mass, momentum end energy. It should be noted that energy equation is normally not included in the marine CFD as water temperature is assumed to be fixed.

Mass conservation

For any studied elemental fluid volume, the mass conservation law states that the mass of fluid is conserved, i.e. rate of increase of mass in fluid element equals to the net rate of mass flow into the fluid element. Based on this law, the continuity equation can be derived as:

$$\frac{\partial \rho}{\partial t} + \frac{\partial (\rho u)}{\partial x} + \frac{\partial (\rho v)}{\partial y} + \frac{\partial (\rho w)}{\partial z} = 0 \tag{2.2.1}$$

or in the mathematical definition for div of a vector property:

$$\frac{\partial \rho}{\partial t} + div(\rho \vec{U}) = 0 \tag{2.2.2}$$

The incompressible isothermal flow is the model we adopt in the marine CFD simulation for the majority of applications. Under this definition, the continuity equations becomes:

$$\frac{\partial u}{\partial x} + \frac{\partial v}{\partial y} + \frac{\partial w}{\partial z} = div\vec{U} = 0 \tag{2.2.3}$$

Momentum conservation

According to the Newton's second law, the net force applied on the fluid element equals its mass time the acceleration of the element. For a moving fluid element, the momentum equation in x, y and z-direction can be written as:

$$\rho \frac{Du}{Dt} = -\frac{\partial p}{\partial x} + \frac{\partial \tau_{xx}}{\partial x} + \frac{\partial \tau_{yx}}{\partial y} + \frac{\partial \tau_{zx}}{\partial z} + \rho f_x$$

$$\rho \frac{Dv}{Dt} = -\frac{\partial p}{\partial y} + \frac{\partial \tau_{xy}}{\partial x} + \frac{\partial \tau_{yy}}{\partial y} + \frac{\partial \tau_{zy}}{\partial z} + \rho f_y \tag{2.2.4}$$

$$\rho \frac{Dw}{Dt} = -\frac{\partial p}{\partial z} + \frac{\partial \tau_{xz}}{\partial x} + \frac{\partial \tau_{yz}}{\partial y} + \frac{\partial \tau_{zz}}{\partial z} + \rho f_z$$

For the isotropic Newtonian fluids, the viscous stress in the momentum equation can be related to the rates of linear deformations of the fluid element, and the latter are expressed through the velocity components. The viscous stress are given as:

$$\tau_{xx} = 2\mu \frac{\partial u}{\partial x}; \ \tau_{yy} = 2\mu \frac{\partial v}{\partial y}; \ \tau_{zz} = 2\mu \frac{\partial w}{\partial z}; \tau_{xy} = \tau_{yx} = \mu \left(\frac{\partial v}{\partial x} + \frac{\partial u}{\partial y}\right);$$

$$\tau_{xz} = \tau_{zx} = \mu \left(\frac{\partial u}{\partial z} + \frac{\partial w}{\partial x}\right); \ \tau_{yz} = \tau_{zy} = \mu \left(\frac{\partial w}{\partial y} + \frac{\partial v}{\partial y}\right) \tag{2.2.5}$$

Then substitute the above equations for viscous stress into momentum equation. For the x-, y- and z-momentum, one can write down:

$$\rho \frac{Du}{Dt} = -\frac{\partial p}{\partial x} + \frac{\partial}{\partial x}\left(2\mu \frac{\partial u}{\partial x}\right) + \frac{\partial}{\partial y}\left[\mu \left(\frac{\partial v}{\partial x} + \frac{\partial u}{\partial y}\right)\right] + \frac{\partial}{\partial z}\left[\mu \left(\frac{\partial u}{\partial z} + \frac{\partial w}{\partial x}\right)\right] + S_{Mx}$$

$$\rho \frac{Dv}{Dt} = -\frac{\partial p}{\partial y} + \frac{\partial}{\partial x}\left[\mu \left(\frac{\partial u}{\partial y} + \frac{\partial v}{\partial x}\right)\right] + \frac{\partial}{\partial y}\left(2\mu \frac{\partial v}{\partial y}\right) + \frac{\partial}{\partial z}\left[\mu \left(\frac{\partial u}{\partial z} + \frac{\partial w}{\partial x}\right)\right] + S_{My} \tag{2.2.6}$$

$$\rho \frac{Dw}{Dt} = -\frac{\partial p}{\partial z} + \frac{\partial}{\partial x}\left[\mu \left(\frac{\partial u}{\partial z} + \frac{\partial w}{\partial x}\right)\right] + \frac{\partial}{\partial y}\left[\mu \left(\frac{\partial v}{\partial z} + \frac{\partial w}{\partial y}\right)\right] + \frac{\partial}{\partial z}\left(2\mu \frac{\partial w}{\partial z}\right) + S_{Mz}$$

The above three equations are the x, y and Z components, respectively, of the momentum equation.

They are scalar equations and are called *Navier-Stokes Equations* in honor of the two men-the Frenchman M.Navier and the Englishman G.Stokes-who independently obtained the equations in the first half of the nineteenth century, J.D Anderson [5].

2.2.2 Governing equations in conservative and integral forms

Using the unfolded expressions for the substantive derivative, mathematical definition of *div* and *grad*, the governing transport equations for the mass and momentum can be written as follows:

$$div\vec{U} = 0$$

$$\rho \frac{\partial u}{\partial t} + \rho div(u\vec{U}) = -\frac{\partial p}{\partial x} + \mu div(gradu) + S_{Mx}$$

$$\rho \frac{\partial v}{\partial t} + \rho div(v\vec{U}) = -\frac{\partial p}{\partial y} + \mu div(gradv) + S_{My} \qquad (2.2.7)$$

$$\rho \frac{\partial w}{\partial t} + \rho div(w\vec{U}) = -\frac{\partial p}{\partial z} + \mu div(gradw) + S_{Mz}$$

The equations are in the so-called conservative or divergence form. In view of obvious commonalities of these equations, one can write a general conserved form for fluid property ϕ:

$$\rho \frac{\partial \phi}{\partial t} + \rho div(\phi\vec{U}) = div(\Gamma_\phi grad\phi) + S_\phi \qquad (2.2.8)$$

The conservation forms the basis of computational procedure in the finite volume method. It clearly reflects different contributions into the transport of a fluid property. In the left-hand side, the first term expresses the rate id change of ϕ the fluid element, and the second term expresses the net of flow ϕ due to convection. In the right-hand side, the first term expresses the rate of change of ϕ due to diffusion with the corresponding diffusion coefficient Γ_ϕ, and the second term expresses the rate of increase of ϕ due to sources. The key procedure in development of the finite volume method is the integration of Eq.2.2.8 over a 3D control volume *CV*, this can be written as follows:

$$\rho \int_{CV} \frac{\partial \phi}{\partial t} dV + \rho \int_{CV} div(\phi\vec{U})dV = \int_{CV} div(\Gamma_\phi grad\phi)dV + \int_{CV} S_\phi dV \qquad (2.2.9)$$

The volume integrals of the convective and diffusive terms can be transformed into the surface integrals over the surface *A* bounding the control volume using the divergence theorem by Gauss-Ostrogradsky which states

$$\int_{CV} div\vec{a}dV = \int_{A} \vec{n}\vec{a}\, dA \qquad (2.2.10)$$

Where $\vec{a}$ is an arbitrary vector property and $\vec{n}$ is the normal to the surface element dA. In worlds, the divergence theorem states that the outward flux of a vector field through a closed surface is equal to the volume integral of the divergence of this vector field on the volume boundary by the surface. After the application of the divergence theorem and changing the order of integration and differentiation in the rate of the change term, the integral form of the transport equations can be derived:

$$\rho \frac{\partial}{\partial t}\left(\int_{CV} \phi dV \right) + \rho \int_{A} \vec{n} \cdot (\phi\vec{U})dA = \int_{A} \vec{n} \cdot (\Gamma_\phi grad\phi)dA + \int_{CV} S_\phi dV \qquad (2.2.11)$$

The integral form of the transport equations represents the statement of conservation of a fluid property for a finite size control volume. This is the principle difference of the integral form from the conservative from which expresses the same conservation principle for an infinitely small fluid element.

2.2.3 Discretization and Solution

Discretization method

To solve the transport equations in the computer, one has to transfer them into discretized form. This process is so-called discretization. The typical discretization methods are finite difference, finite element and finite volume methods. Due to limited space, only finite volume method is discussed here, because of its widely application in the CFD commercial solver.

In finite volume method, discretization schemes are used for the approximation of surface and volume integrals that represent different terms of the equations governing transport of solution variables. Such an approximation allows one to convert a general scalar transport equation to an algebraic equation that can be solved numerically. For a general scalar conserved property ϕ, the integral form of the transport equation has been written in Eq.2.2.9. After the computational mesh is built and each control volume (CV) is defined, this governing equation can be integrated about each CV, resulting in discrete equations that conserve property ϕ on a control-volume base. The integral transport equation applies to each CV, as well as to the whole solution domain. Therefore, if one sums the discrete equations for all CVs, one obtains the global transport equations, because the surface integrals over inner CV faces cancel out.

Equation Solution method

Pressure-based segregated algorithm

The pressure-based solver uses a solution algorithm where the governing equations are solved sequentially (i.e., segregated from one another). Because the governing equations are non-linear and coupled, the solution loop must be carried out iteratively in order to obtain a converged numerical solution. In the segregated algorithm, the individual governing equations for the solution variables (e.g. u, v, w, p, k, e etc.) are solved one after another. Each governing equation, while being solved, is "decoupled" or "segregated" from other equations, hence its name. The segregated algorithm is memory-efficient, since the discretized equations need only be stored in the memory one at a time. However, the solution convergence is relatively slow, inasmuch as the equations are solved in a decoupled manner.

Pressure-based coupled algorithm

In a coupled algorithm, the momentum and continuity equations are solved in a closely coupled manner. Hence, the rate of solution convergence significantly improves when compared to the segregated algorithm. However, the memory requirement increases by 1.5 - 2 times that of the segregated algorithm since the discrete system of all momentum and pressure-based continuity equations needs to be stored in the memory when solving for the velocity and pressure fields.

2.2.4 Computation mesh and boundary

The discretization scheme of finite volume method implies that the control volume (CV) is the prerequisite for the numerical computation. These control volume or subdomains of the computation domain are often called elements or cells, and the collection of all elements or cells is called a mesh or grid. Modern mesh generation technique have evolved to the point where very complex computation domains can be meshed efficiently with a variety of mesh types to ensure high quality simulation. Based upon the connectivity of the mesh, the mesh can be classified into three types.

Structured Meshes

A structured mesh is characterized by regular connectivity that can be expressed as a two or three dimensional array. This restricts the element choices to quadrilaterals in 2D or hexahedra in 3D. It is robust in calculation, however obviously not effective for very complicated geometry.
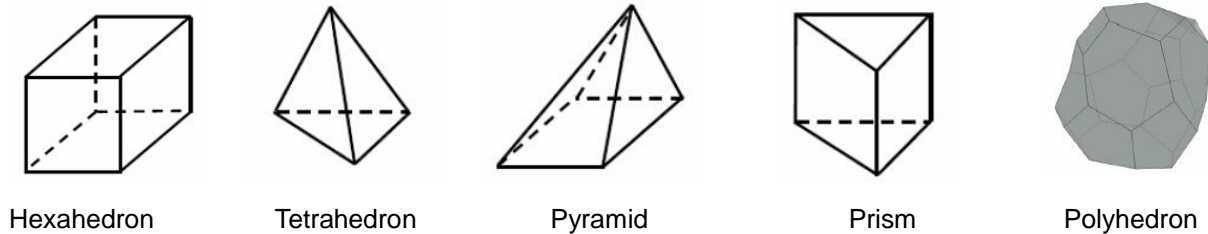
| Hexahedron | Tetrahedron | Pyramid | Prism | Polyhedron |

Figure 2.5 Cell types used in modern CFD codes

Unstructured Meshes

An unstructured mesh is characterized by irregular connectivity is not readily expressed as a two or three dimensional array in computer memory. Compared to structured meshes, the storage requirements for an unstructured mesh can be substantially larger since the neighborhood connectivity must be explicitly stored.

Hybrid Meshes

A hybrid mesh is a mesh that contains structured portions and unstructured portions. Those parts of the geometry that are regular can have structured grids and those that are complex can have unstructured grids. It combines both of merits of structured mesh and unstructured mesh.

Boundary condition

The equations of fluid motion are solved for a certain computation domain. In view of the nature of the problems solved and equations that describe them, as discussed in Section 2.2.1 and 2.2.2, this domain has to be restricted by boundaries. On the boundaries one has to specify the boundary condition and initial conditions under which the equations are solved. These conditions will tell the solver what physical processes take place and should be accounted for at the boundaries of computation domain. The typical boundary conditions in CFD are Wall condition, Symmetrical boundary condition, Inlet, outlet boundary condition and Periodic boundary condition.

● Wall represent the impenetrable surfaces that bound the fluid. The most common type is No-slip boundary condition in viscous flow simulation which ensure that fluid sticks to the wall and moves with the same velocity as the wall.

● The inlet and outlet boundary are the surface through which fluid enters and leaves the computation domain. The most common inlet condition include velocity inlet, pressure inlet and mass flow inlet. The condition imposed on the outlet boundaries can be of pressure outlet, pressure far-field and outflow.

● Symmetry boundaries allow one to take benefit of physical flow symmetry, in order to reduce the size of computation domain thus save memory and time.

● Periodic boundaries allow for the account of periodically repeating nature of the flow in the simulation. This boundary condition is often introduced in the case of propeller.
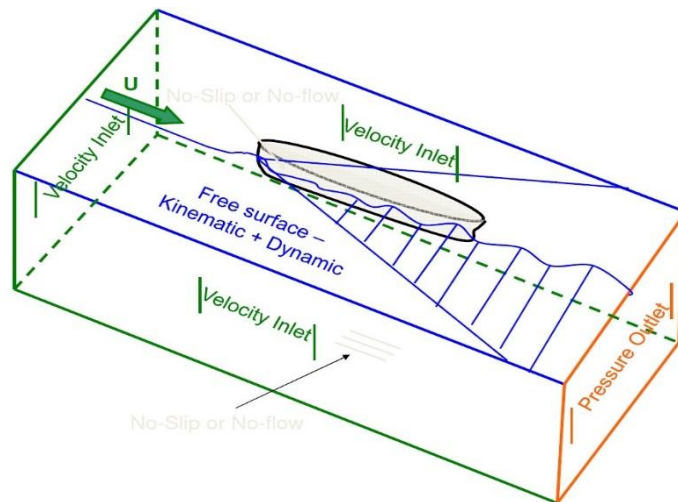
Figure 2.6 Typical boundaries in the CFD simulation of vessel

2.2.5 Turbulence modelling approach

Turbulent flow is the most likely flow condition that can be met in the simulation of marine tasks. In CFD, the random nature of turbulent flow complicates their numerical simulation greatly. Extensive theoretical and experimental research in the mechanisms of turbulence has been made in recent decades. Due to the complexity of these work and related results, only key features of turbulent flow and its numerical models are included in this part.

Phenomenon of turbulence

The phenomenon of turbulence was discovered by Osborne Reynolds. In 1883 he performed a very illustrative experiment with the water flow in a pipe where he injected a painted jet in the middle of the pipe. The observed views show that there is a laminar-turbulent transition between laminar and turbulent flow, and this is affected by the Reynolds number. The majority of industrial flows are high-Reynolds-number flows and are, consequently, turbulent. Turbulent flow has the following features, according to Krasilnikov [6].

● Turbulent flow are unsteady, their properties are random function of time.
● Turbulent flows are three dimensional, even if the averaged velocity field has a dominant 2D direction, the instantaneous field fluctuates in 3D space.
● Turbulent flows are chaotic vertical flows. In which, vortices (eddies) move in a chaotic fashion.
● Turbulent flows fluctuate on a broad range of length and time scales.
● The large eddies in the turbulent flow carry the main portion of turbulent kinetic energy.

Approaches to turbulence
Direct Numerical Simulation (DNS)
DNS methods solve the Navier-Stokes equations directly for all scales of turbulent motions without any turbulence modeling. At the initial step of the solution, the solver generates small disturbances which begin to grow in strength and amplitude as solution proceeds. So, in fact, in the numerical solution, just like in the experiment, one can obtain transition from laminar to turbulent flow regime. Thus, the chaotic motion and interaction of turbulent eddies of different scales is simulated by mathematical principles. However turbulent eddies can vary significantly in scale, and a great part of them, especially in the

beginning are of microscopic length scale. In order to capture such vortices in the numerical solution, the grid resolution must be so fine that only supercomputers can handle it. Thus, it can hardly be expected that DNS will become an engineering tool.

Large eddy simulation (LES)

LES methods provide solution for the largest scale motions of turbulent flow. In other words, the largest and energetically most important turbulence eddies are computed directly, while the effect of smaller eddies, which are not resolved is accounted for through additional stresses obtained from the turbulence theory. The expressions for these stress are much simpler compared to turbulence models in RANS, and for them it is easier to build a consistent theory, because small-scale turbulence is isotropic. The large eddies carry the main portion of turbulent kinetic energy, and in LES they are computed directly, which is a big advantage. Nowadays, LES methods did not find wide use in engineering application, basically the same reasons as DNS. While only the large-scale eddies are calculated, LES methods still require great computational resources.
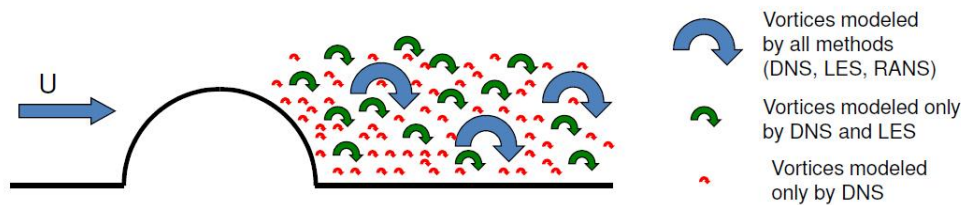
Figure 2.7 Illustration of turbulence scales resolved by DNS, LES and RANS method

Reynolds Averaged Navier-Stokes (*RANS*)

RANS methods are the most commonly used at present for practical calculations of viscous turbulent flows in marine CFD. The RANS approach is based on time averaging of general transport equations and representation of total flow characteristics (velocity and pressure) as a sum of averaged and fluctuating values. The turbulent stresses are modeled by turbulence model, either empirical or semi-empirical using experimental and statistical data. The RANS method resolves only the vortices of largest scale comparable with the size of flow domain, while the rest of turbulence is accounted for through a turbulence model. The RANS method provides the main tool for the engineering simulation of turbulent flows. In Reynolds averaging, the solution variables in the instantaneous Navier-Stokes equations are decomposed into the mean (ensemble-averaged or time-averaged) and fluctuating components. For the velocity components:

$$u_i = \bar{u}_i + u_i{'} \tag{2.2.12}$$

where $\bar{u}_i$ and $u_i{'}$ are the mean and fluctuating velocity components($i = 1,2,3$)

Likewise, for pressure and other scalar quantities:

$$\phi = \bar{\phi} + \phi{'} \tag{2.2.13}$$

where ϕ denotes a scalar such as pressure, energy, or species concentration. Substituting expressions of this form for the flow variables into the instantaneous continuity and momentum equations and taking a time average yields the ensemble-averaged momentum equations. They can be written in Cartesian tensor form as:

$$\frac{\partial \rho}{\partial t} + \frac{\partial (\rho u_i)}{\partial x_i} = 0 \tag{2.2.14}$$

$$\frac{\partial (\rho u_i)}{\partial t} + \frac{\partial (\rho u_i u_j)}{\partial x_j} = -\frac{\partial \rho}{\partial x_i} + \frac{\partial}{\partial x_j}\left[\mu\left(\frac{\partial u_i}{\partial x_j} + \frac{\partial u_j}{\partial x_i} - \frac{2}{3}\delta_{ij}\frac{\partial u_l}{\partial x_l}\right)\right] + \frac{\partial}{\partial x_j}(-\rho \overline{u_i' u_j'}) \tag{2.2.15}$$

These equations are called Reynolds-averaged Navier-Stokes (RANS) equations. They have the same general form as the instantaneous Navier-Stokes equations, with the velocities and other solution variables now representing ensemble-averaged (or time-averaged) values. Additional terms now appear that represent the effects of turbulence. These turbulent stresses, $-\rho \overline{u_i' u_j'}$ must be modeled in order to close equation.

Turbulence model for RANS method

The Reynolds-averaged approach to turbulence modeling requires that the turbulent stresses be appropriately modeled. How to relate the turbulent stress to the dynamic of the flow is one of the central problems of the RANS method and it constitutes the subject of turbulence model development.

A common method employed by many turbulence models is the Boussinesq hypothesis, which implies the analogy between the process of turbulent mixing and molecular diffusion, which is the cause of viscous stresses. According to the hypothesis, a parameter named turbulent or eddy viscosity μ_T is introduced by direct analogy with conventional dynamic viscosity μ, and the components of turbulent stress are expressed as a product of μ_T and rates of linear deformations.

$$-\rho \overline{u_i' u_j'} = \mu_T\left(\frac{\partial u_i}{\partial x_j} + \frac{\partial u_j}{\partial x_i}\right) - \frac{2}{3}\left(\rho k + \mu_t \frac{\partial u_k}{\partial x_k}\right)\delta_{ij} \tag{2.2.16}$$

The Boussinesq hypothesis is used in the Spalart-Allmaras model, the *k-ε* turbulence models, and the *k-ω* models. In the case of the Spalart-Allmaras model, only one additional transport equation (representing turbulent viscosity) is solved. In the case of *k-ε* and *k-ω* models (two-equation model), two additional transport equations are solved for turbulent kinetic energy k$[m^2/s^2]$ and its dissipation rate ε and ω $[m^2/s^2]$. The first variable, k, determines the energy in the turbulence, whereas the second variable can be thought of as the variable that determines the scale of the turbulence (length-scale or time-scale). Advantage of this approach is the relatively low computational cost associated with the computation of the turbulent viscosity. Disadvantage of this hypothesis is that it assumes an isotropic scalar quantity, which is not strictly true. When it comes to complex flows, like flows with strong curvature, or strongly accelerated or decelerated flows the Boussinesq assumption is simply not valid. This give two equation models inherent problems to predict the flow separation and even attached flow with adverse pressure gradients.

SST k-ω turbulence model

The SST *k-ω* model was introduced in 1994 by F.R. Menter to deal with the strong free stream sensitivity of the *k-ω* turbulence model and improve the predictions of adverse pressure gradients, Reference [7]. The model combines both of the merits of *k-ω* and *k-ε* turbulence model. The use of a *k-ω* formulation in the inner parts of the boundary layer makes the model directly usable all the way down to the wall through the viscous sub-layer, hence the SST *k-ω* model can be used as a low-Re turbulence model without any extra damping functions. The SST formulation switches to a *k-ε* behavior in the free-stream and thereby avoids the common *k-ω* problem that the model is too sensitive to the inlet free-stream turbulence properties.

2.2.6 Near-Wall Treatment

Turbulent flows are significantly affected by the presence of walls. Numerous experiments have shown that the viscous-affected region can be largely made up of three layers with their corresponding wall y^+, namely the:

- Viscous sublayer ($y^+ < 5$)
- Buffer layer or blending region ($5 \leq y^+ \leq 30$)
- Fully turbulent or log-law region ($y^+ > 30$ to 60)

The wall y^+ is the distance to the way, made dimensionless with the friction velocity U_t and kinematic viscosity v, y^+ is similar to local Reynolds number.

$$y^+ = \frac{y \cdot U_t}{v} \tag{2.2.17}$$

Very close to the wall, viscous damping reduces the tangential velocity fluctuations, while kinematic blocking reduces the normal fluctuations. Toward the outer part of the near-wall region, however, the turbulence is rapidly augmented by the production of turbulence kinetic energy due to the large gradients in mean velocity. Finally, the interim buffer region between the viscous sublayer and the fully turbulent layer where the effects of molecular viscosity and turbulence are equally important. Detailed flow measurements and DNS calculation indicate that the values of y^+ parameter of the buffer layer lie in the range $5 \leq y^+ \leq 30$.

Traditionally, there are two approaches to modeling the near-wall region. In one approach, the viscosity-affected inner region (viscous sublayer and buffer layer) is not resolved. Instead, semi-empirical formulas called "wall functions" are used to bridge this region between the wall and the fully-turbulent region. In another "near-wall modeling" approach, the turbulence models are modified to enable the viscosity-affected region to be resolved with a mesh all the way to the wall, including the viscous sublayer. In most high-Re-number flows, the wall function approach substantially saves computational resources. In the viscosity-affected near-wall region, in which the solution variables change most rapidly, does not need to be resolved. The wall function approach is popular because it is economical, robust, and reasonably accurate. It's a practical option for the near-wall treatments for industrial flow simulations.

2.3 STAR-CCM+

STAR-CCM+ is one of the largest commercial CFD solver in the world, with its unrivalled ability to tackle problems involving multi-physics and complex geometries, it provides an entire engineering process for solving problems involving flow (of fluids or solids), heat transfer and stress. The solver come packaged with pre- and post-processors which provide everything a user needs to go from the raw CAD geometry to a final flow analysis and visualization. The result is a code that offers outstanding ease-of-use delivered through an object-based tree-structured GUI, which guides even the most novice user through the set-up and analysis of a CFD problem. Utilizing the latest numerical algorithms, physical models and state-of-the-art software coding, it provides the user with a toolset capable of tackling the most complex multi-disciplinary engineering problems without compromising ease-of-use over capability or accuracy. To ensure that users are constantly updated with the very latest advances throughout the product, there are three major releases of STAR-CCM+ every year, Reference [8].

3. METHODOLOGY

Commercial code STAR-CCM+ has been used for the investigation in the scale effects on propellers with systematically varied blade area ratio. Highly automated mesh generation for model and full scale is realized, due to Parts Based Operation functionality in STAR-CCM+. The CFD code solves RANS equations in their integral form, by means of Finite Volumes methods. The spatial discretization of the convective terms is done with a second order upwind based scheme, whereas the diffusive terms are discretized with second order central scheme. The numerical simulation is performed as implicit unsteady, velocities and pressures are solved in a segregated flow, and then coupled by means of the SIMPLE algorithm. The SST k-ω turbulence model is chosen for turbulence closure. The rotation of the propeller is modelled used a moving reference frame system. The numerical results will be compared to the experimental data.

3.1 Propeller geometry

To be able to carry out the numerical simulations in STAR-CCM+, one has to obtain the systematically varied propeller geometry first. This section will introduce the basic modeling procedures for parent propeller P1374 and its variants.

3.1.1 Systematically varied propellers

In the PROPSCALE project, the original parent propeller P1374 in model tests is a controllable pitch propeller (CPP), with its parameters can be found in Table 3.1. In the systematic CFD analyses, propellers derived from P1374 are divided into the four series: "CPP Pitch Series", "Blade Area Ratio Series"," Skew Series", and "Blade Number Series". In all series, except the first one ("CPP Pitch Series"), propellers are considered as fixed-pitch propellers (FPP). "Blade Area Ratio Series" with varied blade area ratio including 0.4, 0.6 and 0.8 are investigated in this paper.

Table 3.1 Parameters of parent propeller P1374

Blades	Diameter	P(0.7)/D	BAR	Skew	Hub ratio
4	0.25 [m]	1.1	0.6	23 [deg]	0.24

Preliminary calculations done with the parent propeller P1374 have shown quite heavy loading on the outer blade sections, resulting in strong tip vortex. This result is thought to be related to the radial distributions of chord length and pitch at the outer blade sections, which may not be typical for conventional open propeller designs (it should be remembered that propeller P1374 was conceived as a compromise design to be used in the tests with both open and ducted propulsors). Obviously, the aforementioned phenomena may have considerable influence on scale effects. Therefore, it is planned to include in the investigations one alternative distribution of chord length.

3.1.2 Geometry modeling

The GAMBIT software is used to produce the initial blade model as a solid (Parasolid format). Then, this initial model can be re-meshed in STAR-CCM+ by a special Java macro, in order to fix minor surface flaws and ensure a better quality of subsequent Boolean operations with geometry parts. Table 3.2 lists all the geometrical elements used to model the parent propeller P1374, using cylindrical section definition.

When generating the geometry of fixed pitch series propellers the following conditions apply:

- Distributions of max section camber f_o/R and rake x_r/R are kept unchanged through series;
- Chord length distribution b_r/b(0.7) is kept unchanged through series;
- Distribution of max thickness to chord length ratio e_o/b_r is kept unchanged through series (whereas e_o//R varies according to given A_E/A_o and Z);
- Distributions of pitch P_r/P(0.7) and skew T_s/T_s(max) are based on the parent propeller.

Table 3.2 Geometrical elements of parent propeller P1374

r/R	b_r/R	e_o/R	cs/R	P_r/R	f_o/R
0.240	0.2668	0.0761	0.0000	2.1560	0.0024
0.250	0.2827	0.0750	0.0036	2.1579	0.0074
0.300	0.3599	0.0694	0.0217	2.1667	0.0141
0.350	0.4327	0.0640	0.0393	2.1745	0.0175
0.400	0.5008	0.0588	0.0557	2.1813	0.0196
0.500	0.6208	0.0490	0.0814	2.1917	0.0216
0.600	0.7151	0.0400	0.0899	2.1979	0.0214
0.700	0.7758	0.0318	0.0707	2.2000	0.0198
0.800	0.7879	0.0244	0.0115	2.1764	0.0169
0.900	0.7128	0.0178	-0.1014	2.0753	0.0125
0.975	0.4903	0.0134	-0.2302	1.9322	0.0065
0.990	0.3674	0.0125	-0.2612	1.8958	0.0041
1.000	0.1500	0.0120	-0.2829	1.8700	0.0000
r/R	b_r/b(0.7)	e_o/b_r	T_s [deg]	P_r/P(0.7)	T_s/T_s(max)
0.240	0.3439	0.2852	0.0000	0.9800	0.00000
0.250	0.3644	0.2653	0.4856	0.9809	0.02111
0.300	0.4639	0.1928	2.7202	0.9849	0.11827
0.350	0.5577	0.1479	4.5747	0.9884	0.19890
0.400	0.6455	0.1174	6.0255	0.9915	0.26198
0.500	0.8002	0.0789	7.6501	0.9962	0.33261
0.600	0.9217	0.0559	7.4164	0.9991	0.32245
0.700	1.0000	0.0410	5.1755	1.0000	0.22502
0.800	1.0156	0.0310	0.7558	0.9893	0.03286
0.900	0.9188	0.0250	-6.0601	0.9433	-0.26348
0.975	0.6319	0.0273	-12.9012	0.8783	-0.56092
0.990	0.4736	0.0340	-14.4602	0.8617	-0.62870
1.000	0.1933	0.08000	-15.5355	0.8500	-0.67546

Fig.3.1-3.4 present the characteristics of the propeller P1374, including maximum camber distribution, pitch distribution, etc. For propellers having alternative chord length distribution, maximum thickness to chord length ratio e_o/b is modified compared to the parent propeller, in order to ensure a more realistic blade geometry at the outer blade sections; Fig.3.3 and 3.4 plots the difference. Detailed geometrical data of this variant propeller can be found in Appendix A.
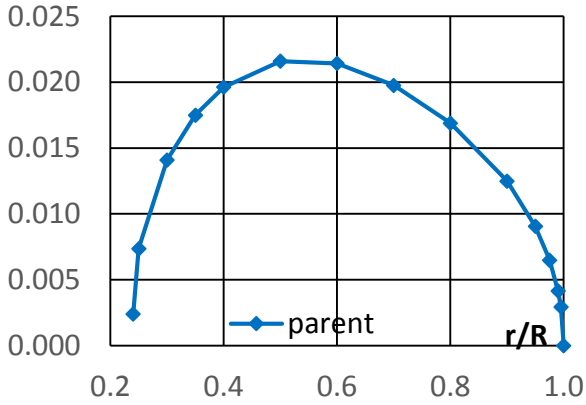
Figure 3.1 Max camber distribution
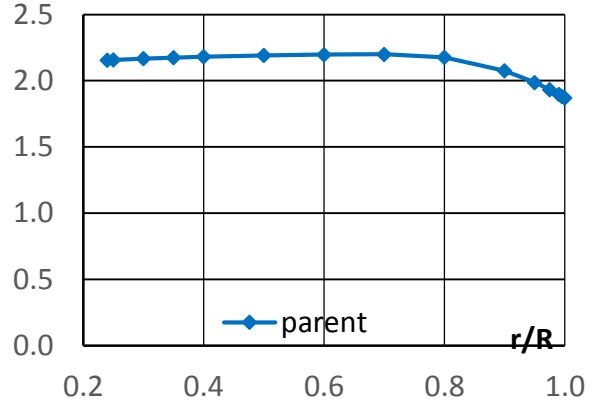
Figure 3.2 Pitch distribution
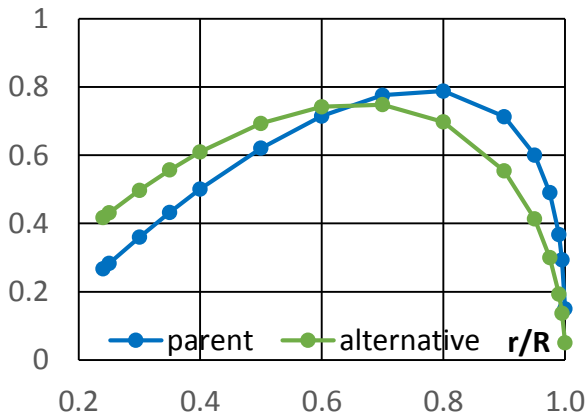
Figure 3.3 Chord length distribution
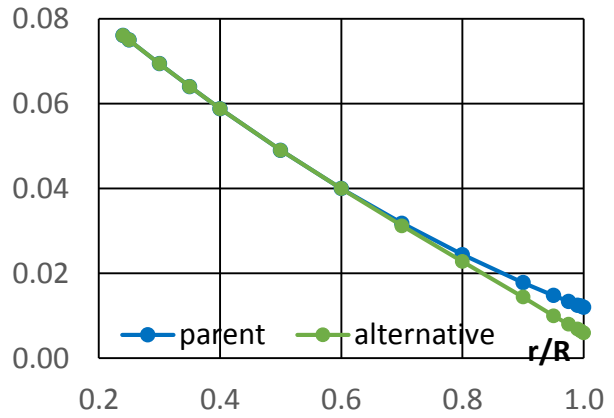
Figure 3.4 Max thickness distribution

Propellers with varied BAR are derived by changing the chord length to radius ratio b_r/R. Max thickness is altered, however max thickness to chord length ratio e_o/b is same through the series. Apart from these, all other geometrical elements were kept identical. The obtained geometry of the series propellers in a general view can be found in Table 3.3.

Table 3.3 General view of propeller with varied blade area ratio
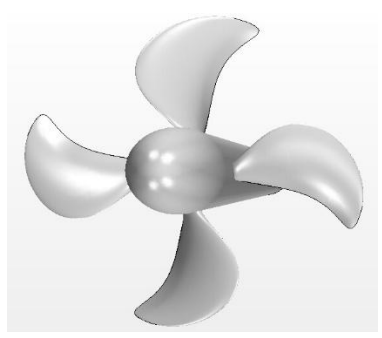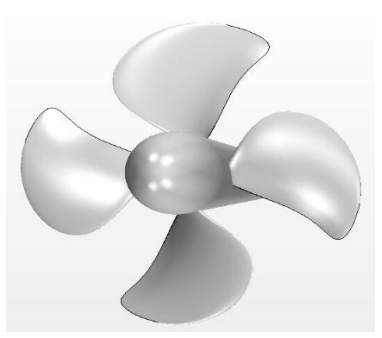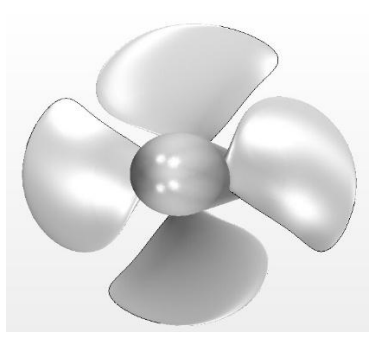
BAR=0.4	BAR=0.6	BAR=0.8
D=0.25m; Z=4; Sew 23°; P(0.7)/D=1.1		

Figure 3.5 presents the geometry of parent propeller and its variant with alternative chord length distribution, one can easily tell the difference between the two propellers.
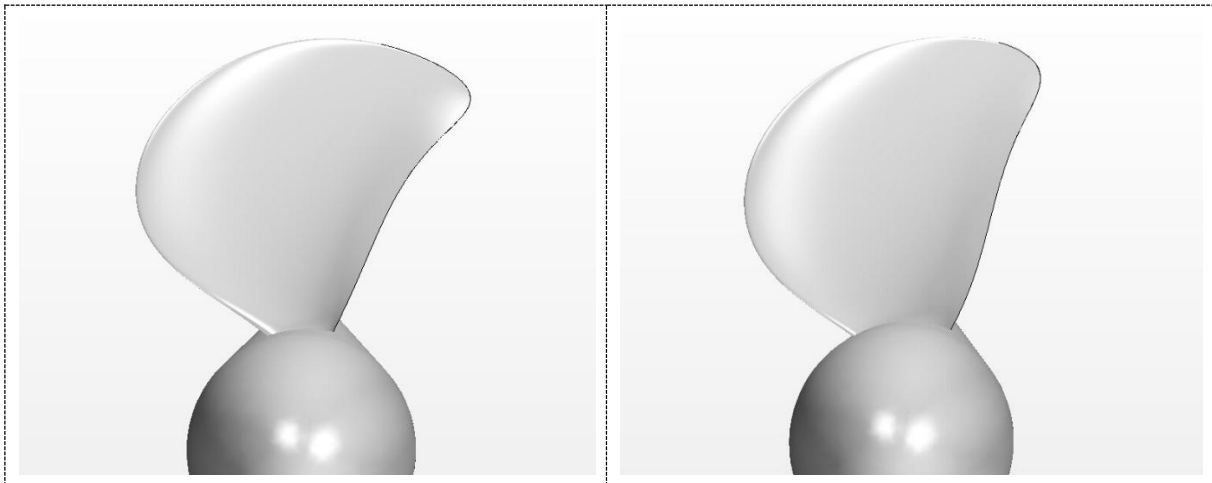
Figure 3.5 Parent propeller with BAR 0.6 and Propeller with alternative chord length distribution

Blade Tip

As one can find in Fig.3.6, there is a sharp edge in the blade tip area marked by feature curves. This is because the blade tip used in the simulations is just the cylindrical blade section at the radius 1.0R. For realistic propellers, the blade tip is normally faired to round off sharp edges. However, since the definition of such rounding is quite uncertain (and will surely be different for propellers having different blade area ratio and skew) the initial tip geometry is used in these systematic calculations. The feature curves describing the sharp edge is critical to control the mesh quality in the blade tip area. It will be discussed later in Part 3.2.2 meshing->feature curve.
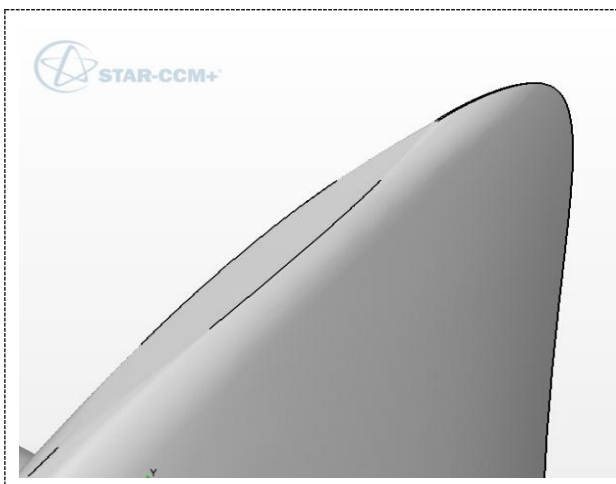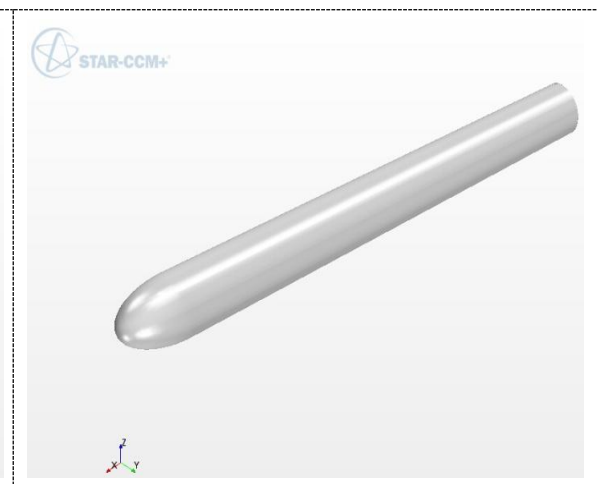
| Figure 3.6 Blade tip | Figure 3.7 Propeller hub |

Propeller Hub

The propeller hub is defined according to the hub ratio with diameter D=0.06m in model scale. In order to ensure correct intersection between blade and hub, the blade was extended towards inner radii on purpose. One can find the hub geometry in Figure 3.7.

3.2 Simulation setup

This section covers the procedure for carrying out simulations of the series propellers. Great thanks to Vladimir, from MARINTEK, who provided many necessary guidelines and advices in this part.

3.2.1 Domain modeling

When modelling propeller in straight flow in open water conditions, one can take advantage of flow axial symmetry, and use only one blade passage domain with appropriate periodic boundaries. The most straightforward setup for one blade passage flow simulation implies the use of a sector, having angular dimension 360/Z deg. (where Z is the number of propeller blades), which is cut from a cylinder and includes one whole blade, as shown in Fig.3.8. Such a setup is also simplest for post-processing. However, if propeller blades are wide, they may not be entirely accommodated in the domain as described above.
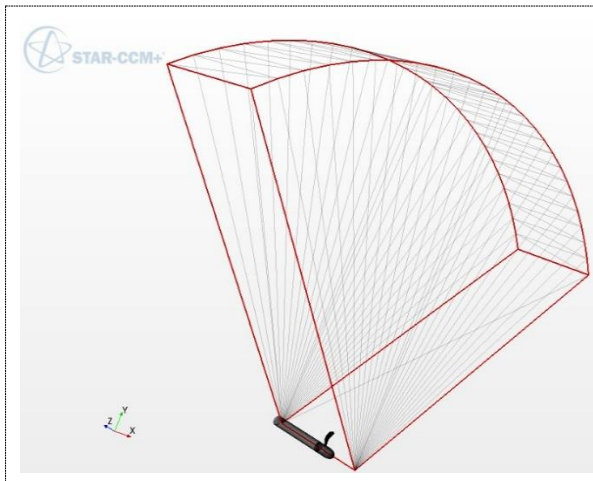
| Figure 3.8 One-blade-passage domain | Figure 3.9 Two-blades-split domain |
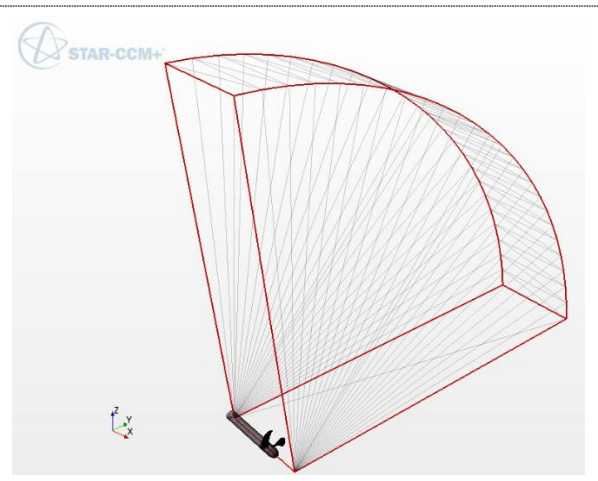
The simplest way to solve the problem is to use an alternative one blade passage setup that includes the same cylindrical sector, but instead splits two neighbouring blades, as shown in Fig.3.9. Such a setup will ensure that complete blade geometry will be accommodated in the one blade passage domain, and flow periodicity will be observed. The present work utilized One-blade-passage domain to simulate all the cases. At the same time, for comparison, propeller with BAR 0.6 in model scale will be simulated once again in the Two-blades-split domain.

A gap between propeller hub and shaft was created to replicate the physical setup of the open water model test. Practice shows that only by including the gap between the rotating propeller hub and stationary shaft housing one can achieve adequate prediction of the axial force acting on the hub. In the present simulations, propeller thrust includes blade thrust and hub thrust, exactly as measured in the tests. Blade thrust is less dependent on whether one includes the gap in the simulation or not. However, hub force may not be predicted correctly in the setup without gap (blades on shaft, part of which is separated to form the hub surface) because of the uncertainty in the definition of gauge pressure on open surface.

3.2.2 Meshing

A mesh is the discretized representation of the computational domain. STAR-CCM+ provides meshers and tools that can be used to generate a quality mesh for various geometries and applications, Reference [9]. In the present simulation, the Surface Remesher, Polyhedral Mesher, Prism Layer Mesher and Extruder are applied to generate the volume mesh. Base size in model scale is set to 0.25m equals to propeller diameter. While in full scale, it has to be augmented by the scale factor 20.

The idea behind the base size is that one can set other meshing values like surface minimum / target size, Prism layer thickness e.g. proportionally to the base value. All the mesh values which are defined by the ratio to the base size will be changed automatically in full scale.

Surface Remesher

In order to improve the overall quality of an existing surface and optimize it for the volume mesh models, the surface remesher was used to re-triangulate the surface. Parameters including relative target size and relative minimum size are used to control the surface mesh size in particular region.

Table 3.4 Parameters of surface remesher (% to base size)

	Relative target size	Relative minimum size
Blade surface	0.5%	0.125%
Tip	0.125%	0.125%
Trailing edge	0.125%	0.125%
Hub and Shaft	3%	1%

Polyhedral Mesher

It generates a volume mesh that is composed of polyhedral-shaped cells. The polyhedral meshing model utilizes an arbitrary polyhedral cell shape in order to build the core mesh. The polyhedral core mesh density can be increased or decreased by using the volume mesh blending factor, which is set to be 0.5 at the present case.

Prism Layer Mesher

The prism layer mesh model is used with a core volume mesh to generate orthogonal prismatic cells next to wall surfaces or boundaries. Prism layers are mainly used to resolve flow boundary layers and they are critical to improve the accuracy of the flow solution.

Table 3.5 Parameters of Prism layer mesh

Base size	Prism layer thickness	Number of prism layers	Prism layer stretching
0.25m	0.25% base size	10	1.4

The near wall y^+ is very sensitive to the prism layer mesh setting. The automatic mesh setup used in the simulations should allow for adequate near-wall (boundary layer) flow treatment in both the model scale and full scale conditions without modification of Prism Layer Mesher setting. In model scale, it will result in wall $y^+<5$, while in full scale, it will result in wall $30<y^+300$. For this reason, the present mesh

is called High-Re mesh, referring to wall y^+ values provided in full scale. One can find the resulted y^+ plots of model and full scale in Figure 4.3 and 4.4, Chapter 4. As far as near-wall treatment is considered, it will be discussed further in the Part 3.2.5 Physics.

Extruder

Regarding the simulation domain it should be noted that the initial domain created in the simulation is a short one. When generating volume mesh, the Inlet and Outlet boundaries of this initial domain shall be extruded using the Extruder meshing tool, in order to place the final Inlet and Outlet boundaries at a sufficient distance from propeller. The use of Extruder helps to reduce the total cell count without compromising mesh quality by using the prismatic mesh in the extrusion domains. The parameters of extruder mesh in model scale can be found in Table 3.6. While in full scale, the magnitude shall be changed according to the scale factor.

Table 3.6 Parameters of Extruder mesh

	Inlet	Outlet
Magnitude	1.25 m	3.75 m
Numbers of layers	15	30
Stretching	20	40

Feature curve

The Two-blades-split domain setup introduced earlier may have its own pitfalls. One issue is related to the intersection of blade surface with periodicity boundaries, minor surface flaws may occur at the intersection of the blade with periodic boundaries. The surface remesher tries to repair these flaws, often resulting in unnecessary locally increased mesh density and higher overall cell count, if special treatment is not applied to the blade surface mesh.
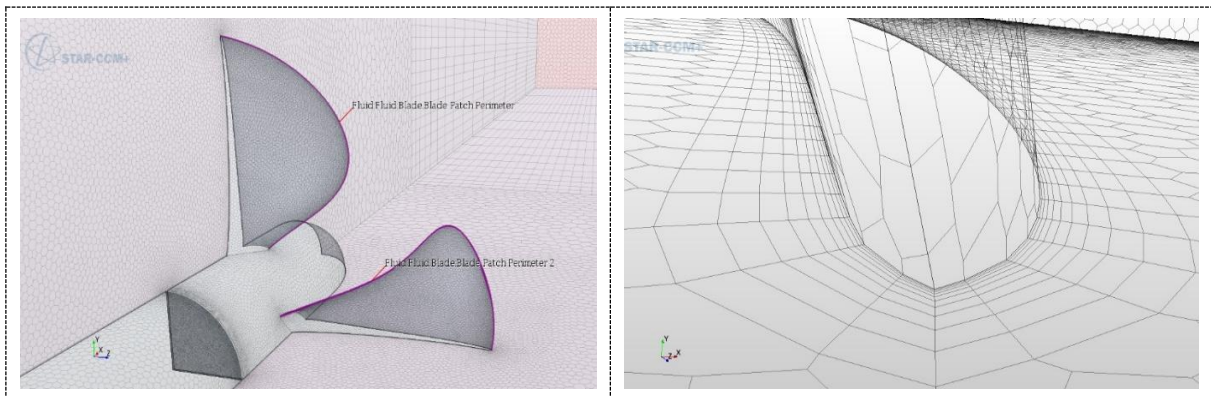
Figure 3.10 Introduction of blade patch perimeter feature curves

One remedy is to make use of feature curves. The setup with the first variant of one blade passage domain allows in principal only one (combined) feature curve for all geometry parts. Surface remeshing on the blade is then entirely guided by the values of target size and minimum surface size set up for blade, tip and TE (Trailing Edge) boundaries. Such meshing model may result in the aforementioned issues when using the alternative setup with two blades split. To remedy this one can, at the stage of

preparation of geometry parts, produce a separate set of feature curves describing blade patch perimeters and following the blade edges, as shown in Fig.3.10. The blade edges and tip region are the areas where finer mesh is needed. Then one can set up both the target size and minimum size for the blade surface to the same desired value and instruct Surface remesher to do mesh refinement only along the Blade Patch Perimeter feature curves, on the blade tip and blade TE. The rest of the blade surface and regions on the periodic boundaries where they intersect with the blade will be unaffected, resulting in uniform, good quality mesh.

Volumetric control

The volumetric control is used to specify the mesh density in a specific zone. The settings given in Table 3.7 are the best practices from MARINTEK for propeller open water test.

Table 3.7 Dimensions and positions of cylindrical control

VC	Upstream	Downstream	Radius	Mesh size
VC_Cylinder-1	0.8D	0.5D	1.12R	0.01D
VC_Cylinder-2	0.5D	1.0D	1.28R	0.02D
VC_Cylinder-3	Through the whole domain		1.8R	0.04D
VC_Cylinder-4	Through the whole domain		2.4R	0.08D
VC_Cylinder-5	Through the whole domain		3.2R	0.12D
VC_Cylinder-6	Through the whole domain		4.2R	0.18D
VC_Cylinder-7	Through the whole domain		8.0R	0.25D

The cylindrical volumetric control serve the purposes of mesh refinement around propeller and smooth transition in cell size from the areas with finer mesh to the areas with coarser mesh. Cylinder-1 in the domain is shown in Fig.3.11. The gap between shaft and hub is also need to be refined, one can see the result of this region after volumetric control in Fig.3.12.
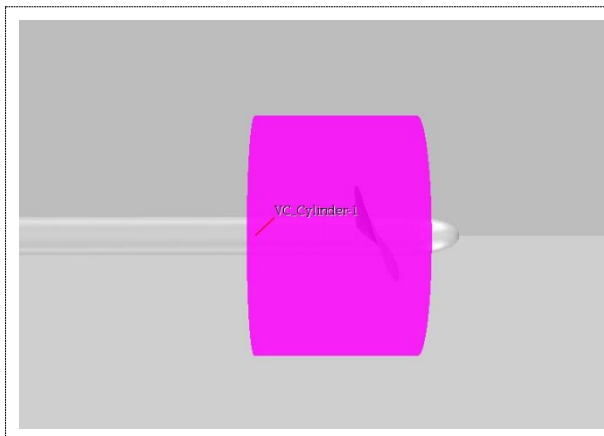
Figure 3.11 Volumetric control cylinder-1   **Figure 3.12 Refined mesh in gap area**
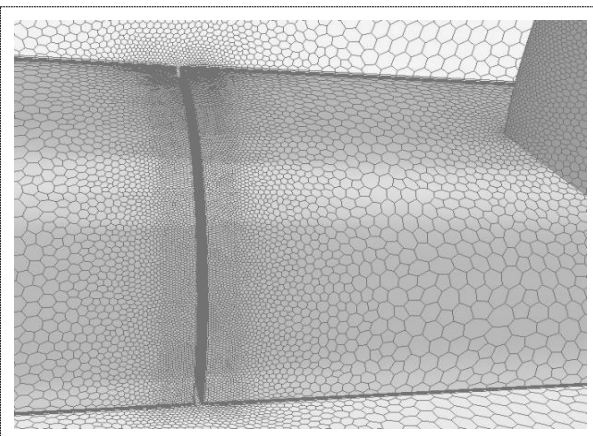
The general view of generated volume mesh after the all these procedures is shown in Figure 3.13. Total cell number is around 1.2-1.4 million.
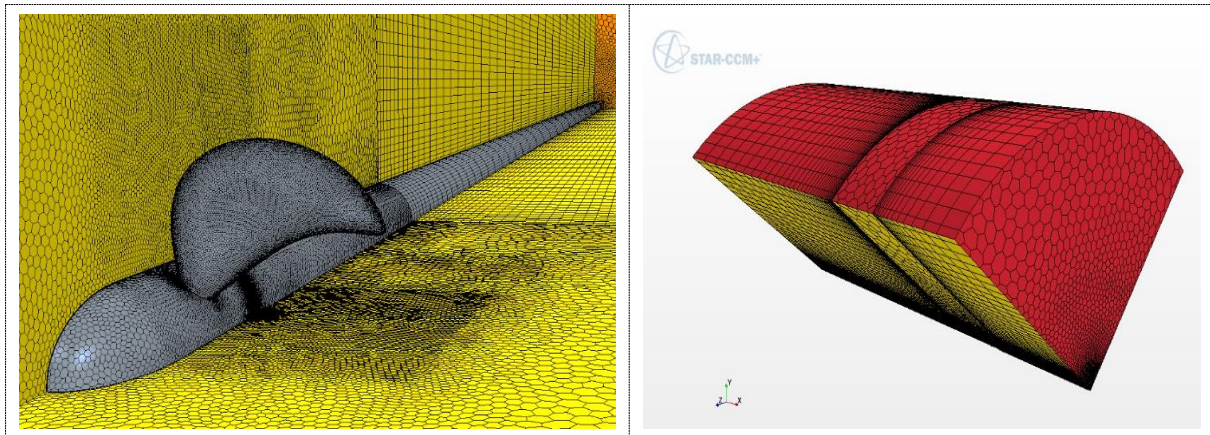
Figure 3.13 General view of volume mesh

3.2.3 Boundary condition

In order to close up the equations of system, one has to provide the boundary of the domain with necessary information, which is called boundary condition. The definition of boundary condition including boundary type and physical model employed is largely guided by physical arguments and success of simulations in earlier cases. The boundary type in the present simulation can be seen in Fig.3.14.

The velocity inlet and pressure outlet boundary are placed in the upstream and downstream respectively, with its position defined in Part 3.2.2 Mesh->Extruder. Periodical boundary is set to take advantage of flow axial symmetry. Finally, Wall condition applies to the surface of imported propeller and hub geometry.
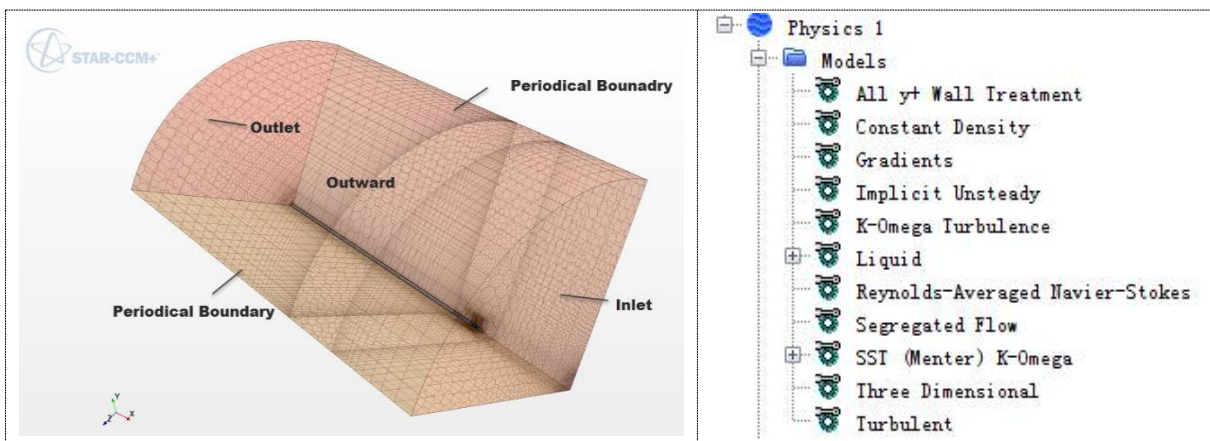
Figure 3.14 Boundary condition   **Figure 3.15 Physics model**

3.2.4 Initial condition

For the equations to be solved, each cell has to be initialized by setting up preliminary solution data to the primary variables associated with the model at the time step zero. Normally, the simulation domain is initialized by supplying the values of gauge pressure, temperature, velocity components and turbulence characteristics. In the beginning of simulation, the solution should be initialized for the entire computation domain.

Turbulence characteristics

Table 3.8 Turbulence characteristics

Turbulence intensity	Turbulent velocity scale	Turbulent viscosity ratio
0.1	1 m/s	10

Velocity component

The RPS in full scale is derived from Froude number identity

$$\frac{\pi \cdot n_M \cdot D_M}{\sqrt{g \cdot D_M}} = \frac{\pi \cdot n_S \cdot D_S}{\sqrt{g \cdot D_S}} \rightarrow n_S = n_M \cdot \sqrt{\frac{D_M}{D_S}} = \frac{n_M}{\sqrt{M}} \tag{3.1}$$

In which, subscript of "M" and "S" denotes a quantity in model and full scale respectively. Scale factor M=20. According to the formation for Advance Coefficient, the inlet velocity V_A in model and full scale are tabulated as:

Table 3.9 Velocity component in [m/s]

J	0.1	0.3	0.5	0.7	0.9	1.1
Model scale V_A	0.375	1.125	1.875	2.625	3.375	4.125
Full scale V_A	1.67705	5.03115	8.38525	11.73936	15.09346	18.44756

The above J values are customized for the calculations with the propeller at the pitch setting P(0.7)/D=1.1. For different pitch settings, the J values corresponding to free sailing operation conditions may be adjusted, so that one point is located below the point of maximum efficiency, one point is close to the point of maximum efficiency, and one point is behind the point of maximum efficiency.

3.2.5 Physics

In Fig.3.15, one can find the selected physics model, which represents materials in the CFD domain. Water flow is assumed to be fully turbulent and unsteady. All y^+ Wall Treatment is utilized to tackle the near wall region. The water properties are the same in model scale and full scale calculations.

Wall Treatment

A "Wall Treatment" in STAR-CCM+ is the set of assumptions for modeling near-wall turbulence quantities such as wall shear stress, turbulent production and turbulent dissipation, Reference [9]. Traditionally, the three basic types of wall treatment are:

High y^+ Wall Treatment: equivalent to the traditional wall function approach, in which the near-wall cell centroid should be placed in the log-law region (30 ≤y^+ ≤ 100). The wall functions used in the modern CFD solvers are the enhanced wall functions, which are different from the standard wall log-law equations and they are designed to cope with adverse pressure gradients such as occur in separated flows. The accuracy of such wall functions is of course still lower than that of the low-Re method applied on a good quality mesh, but they are quite capable of reproducing correctly the integral forces (such as for instance propeller K_T and K_Q).

Low y^+ Wall Treatment: suitable only for low-Re turbulence models in which the mesh is sufficient to resolve the viscous sublayer ($y^+ \approx 1$) and 10-20 cells within the boundary layer.

All y^+ Wall Treatment is a hybrid approach that seeks to represent the behaviors of the previous two

wall treatments in the limit of very fine or very coarse meshes. It is a design goal that this wall treatment should give results similar to the Low y^+ treatment as $y^+ \rightarrow 1$ and to the High y^+ treatment for $y^+>$ 30. It will also give reasonable results for intermediate meshes where the cell centroid falls in the buffer layer. The All y^+ wall treatment is the most general, and should be used whenever available. Figure 3.16 shows the distribution of appropriate range of y^+ for different wall treatment.
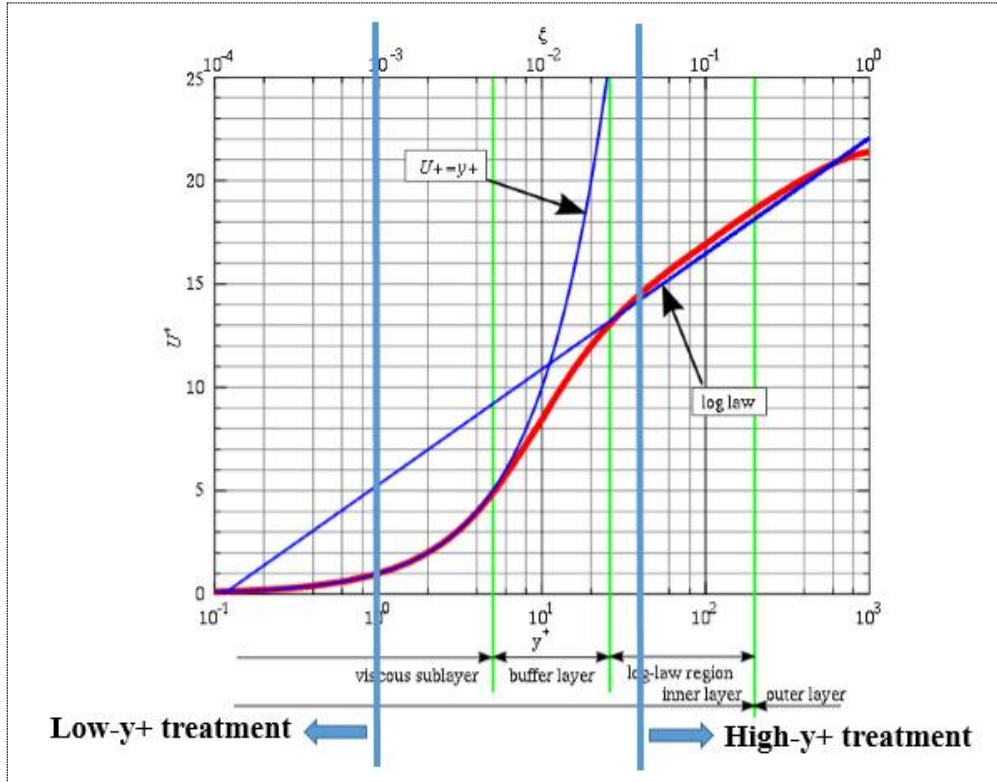
Figure 3.16 Subdivisions of turbulent near-wall region

The *All y^+ method* blends turbulence quantities (TQ) such as dissipation, production, stress tensor, etc. calculated by the High y^+ approach or by the Low y^+ approach using an exponential weighing function. The final value for the turbulence quantity is calculated as:

$$\mathrm{TQ} = g \cdot TQ_{low} + (1-g)TQ_{high} \qquad (3.2)$$

where g is given by the following function:

$$g = \exp(-\frac{Re_y}{11}) \qquad (3.3)$$

where $Re_y = \sqrt{K}y/\upsilon$, y is the normal distance from the wall to the wall-cell centroid, K is the turbulent kinetic energy, and υ is the kinematic viscosity. It is designed when the wall y^+ is small the contribution of the wall function is negligible.

To check the quality of prism layer mesh, it is beneficial to introduce the term *Turbulent Viscosity Ratio.* From first principle, it would be fair to say that while any laminar flow would have shear stress owing to its viscosity and velocity gradients, the reason of "turbulence" is the additional shear stresses (Reynolds stresses) that arise due to random fluctuating velocity components, which are realized through the definition of turbulent viscosity. Essentially, the ratio of turbulent viscosity to molecular viscosity gives an indication about how strong the Reynolds stresses are, as compared to molecular stresses. So it sounds reasonable to use this ratio as a measure of turbulence.
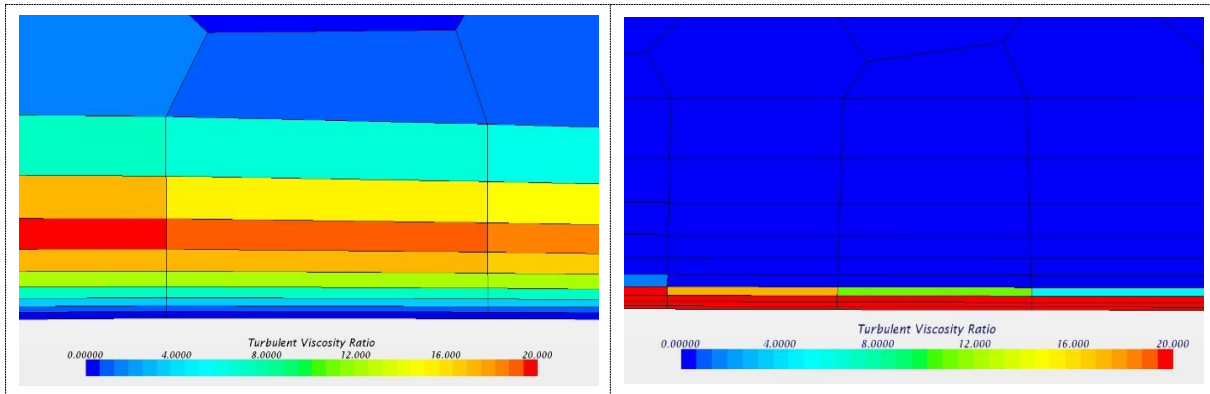
Figure 3.17 Turbulent Viscosity Ratio distribution in prism layer mesh at the section of 0.7R in model and full scale

Figure 3.17 presents the resulted prism layer mesh with scalar field of *Turbulent Viscosity Ratio* at the section of 0.7R in model and full scale simulation. The diagram on the left hand indicates a good mesh for a low-Re turbulence model. One can observe that the transition in size from the first prism layer to the free stream core elements has been regulated well. Since the first cell locates in the laminar sublayer which exhibits laminar flow characteristics thereby resulting in no turbulent viscosity. As it gradually moves through the buffer region and into the log region a large rise in the turbulent viscosity ratio can be found before it dissipates into the free stream. This maximum turbulent ratio will generally occur near the middle of the boundary layer, which also gives an indication of the physical boundary layer thickness (twice the location of the maximum turbulent viscosity ratio gives the boundary layer edge).   In the case of full scale (right-handed) the y^+ we have prescribed at the first cell indicates they are in the logarithmic region of the turbulent boundary region, which is the region largely dominated by inertial forces and thus high levels of turbulent viscosity ratio is expected. The turbulence gradually dissipates as we approach free stream conditions.

The general recommendations that being followed in the simulations is to aim at y^+<5 in model scale simulations, and 30<y^+<300 in full scale simulations. Using the All y^+ treatment method relaxes the above limits. This means that, if some surface areas fall in the "buffer" range (5<y^+30), it is possible to go on with the simulation and expect reasonable results. Since the special wall functions are used in the All y^+ Treatment method, it is still better to ensure that the zones where y^+ appears in the buffer layer are relatively small (or less significant) compared to the zone where y^+ is in main "good" range.

For example, in case of full scale with the scale factor 10, the greatest part of the blade is actually in the range y^+>20, while the most important outer blade sections r/R>0.6 are well in the range of y^+>30. See Figure 3.18.Therefore, it is believed that even with the default prism layer mesh settings, it is absolutely adequate to do the calculations at the scale factor 10. A few simulations has been done earlier by MARINETEK when part of the blade was in the "buffer" range of y^+ and they showed consistent results. In conclusion, it is just important to control that most of important blade surface domain is in the intended "good" range of y^+.
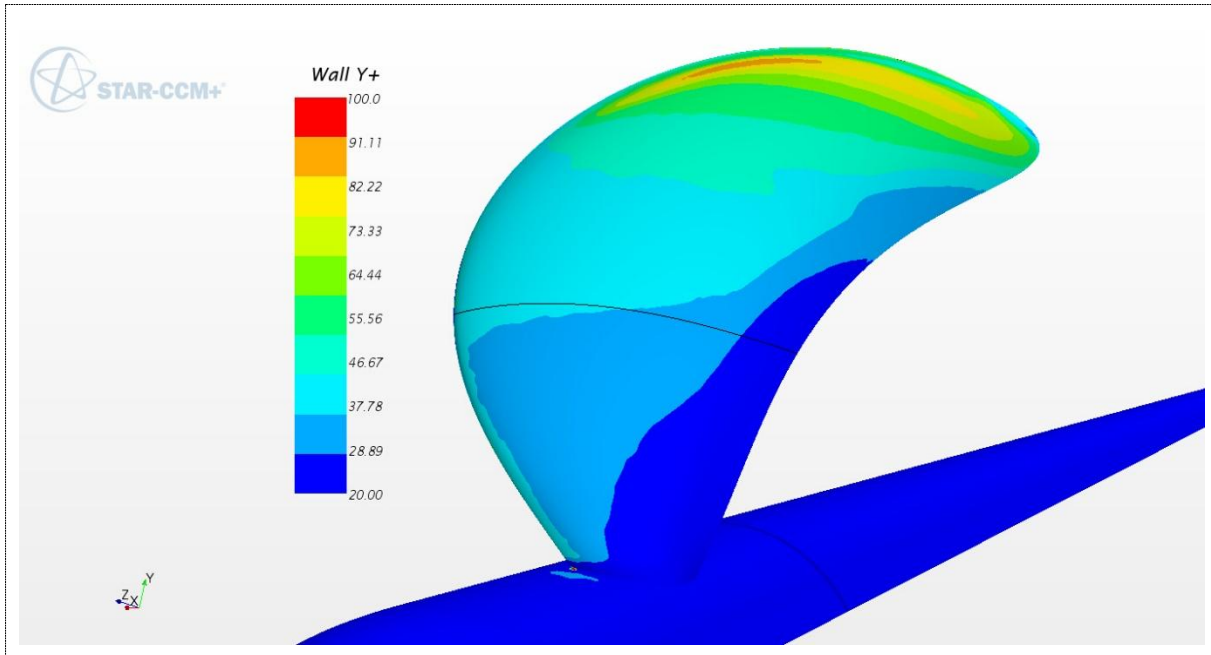
Figure 3.18 Wall y^+ of full scale simulation with scale factor 10

Implicit unsteady

In the Implicit Unsteady approach, each physical time-step involves some number of inner iterations to converge the solution for that given instant of time. These inner iterations can be accomplished using implicit spatial integration or explicit spatial integration schemes. One can specify the physical time-step size that is used in the outer loop. The integration scheme marches inner iterations using optimal pseudo-time steps that are determined from the Courant number. With the Implicit Unsteady approach, one has to set the physical time-step and the number of inner iterations at each physical time-step.

Table 3.11 Implicit unsteady solver setting

Time Step	No. inner iterations	Maximum Physical Time
Propeller turn to 2 degrees	5	30 complete propeller revolutions

Liquid

Density: ρ=999.1 [kg/m^3]

Dynamic viscosity: μ=0.00114 [Pa·s]

Kinematic viscosity: υ=1.141$\times 10^{-6}$ [m$^2 \cdot$ s^{-1}]

3.2.6 Moving Reference Frames

CFD program solves the equations of fluid flow, by default, in a stationary reference frame. However, there are many problems where it is advantageous to solve the equations in a moving reference frame. Such problems typically involve moving parts (such as rotating blades in the present case), and it is the flow around these moving blades that is of interest. When a moving reference frame is activated, the equations of motion are modified to incorporate the additional acceleration terms which occur due to the transformation from the stationary to the moving reference frame, see Reference [10].

In the case of a propeller operating in a straight uniform flow, the flow around propeller will be unsteady in the laboratory reference. However, by introducing a rotating reference frame fixed on propeller, participating together with the propeller, then in such reference frame. The problem will be rendered steady. There are several immediate benefits of such transformation. Firstly, there is no need to introduce any mesh motion and to apply time stepping solution. Secondly, time and memory can be further saved by modeling only one blade passage with periodic boundaries instead of the whole 360-degrees domain. In this case, the MRF should theoretically give exactly the same results as the complete time dependent simulation. In practice, difference will occur caused by numerical sources, but they are negligible small. The MRF therefore is an excellent approach to the prediction of propeller open water characteristics. Figure 3.19 gives an illustration of MRF involves rational motion.
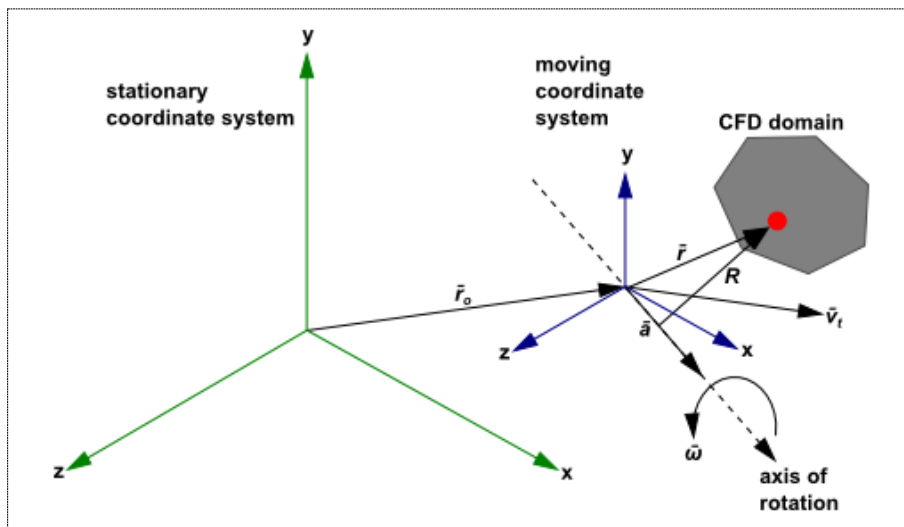
Figure 3.19 Illustration of a Moving Reference Frame participating in rotational motion

3.2.7 Parts based operation

In the present simulation, all domain geometry manipulations are performed at the Parts level, one can simply replace the Blade part in the Parts list with a new blade surface. Additional operations (copying, transforming) will be needed after importing a new blade part in the simulation according to the setup with blade split, to create the neighbouring blade. When done, one has to simply Update the resulting Fluid part and proceed with meshing. These steps are made automatically due to the Parts Based Operation functionality and Assign Parts to Region functionality of STAR-CCM+.

However in the used version of STAR-CCM+, the Extruder option is not supported by the Parts Based Meshing (PBM), and for that reason one has to modify the extrusion settings for the Inlet and Outlet boundaries under Boundaries-Inlet(/Outlet)->Mesh Values ->Normal Extrusion Parameters. The Magnitude of extrusion should be changed according to the scale factor

3.2.8 Reports and Post-processing

The report summaries allow engineering quantities such as drag, lift, torque, or mass flow to be computed. It is very necessary to create a report for the desired propeller force coefficient, then the propeller open water characteristics can be allocated for varied loading conditions.

The default force coefficient definition in STAR-CCM+ is given as:

$$C_F = \frac{F}{1/2 \cdot \rho \cdot V^2 \cdot S}$$ (3.4)

It has no be noted the measured force in the numerical simulation is only a quarter of total force, due to periodical boundary setting. The form of propeller thrust coefficient is given as:

$$K_T = \frac{T}{\rho \cdot n^2 D^4}$$ (3.5)

Reference velocity V is the value of blade tip velocity (n*D) in [m/s]. By keeping the two equations identical, thus reference area S can be derived. Based on the same method, the report for propeller torque coefficient can prepared. When estimating scale effect on propeller characteristics, it is also very useful to identify the respective Pressure and Friction (Shear) contribution in propeller thrust and torque, which can be also outputted by the Reports.

The powerful post-processing capability in STAR-CCM+ allows one to obtain a detailed insight into flow behaviors that are difficult, expensive or impossible to study using traditional experimental techniques. The present simulation utilized some basic post-processing instructions in STAR-CCM+. In particular, it contains scenes for visualizing wall Y+ distribution, pressure coefficient in certain section section, constrained streamlines on propeller blades, boundary layer flow visualization, and Vorticity field around propeller by Volume Rendering, etc. One can find these results in chapter 4.

3.2.9 Running

So far, all the setup have been clarified and the simulation is ready for the final calculation. During iteration, one can judge the convergence of solution by checking residuals plot, which are created automatically within every simulation. While it is true that the residual quantity tends toward a small number when the solution is converged, it cannot be relied on as the only measure of convergence.

Residuals plot
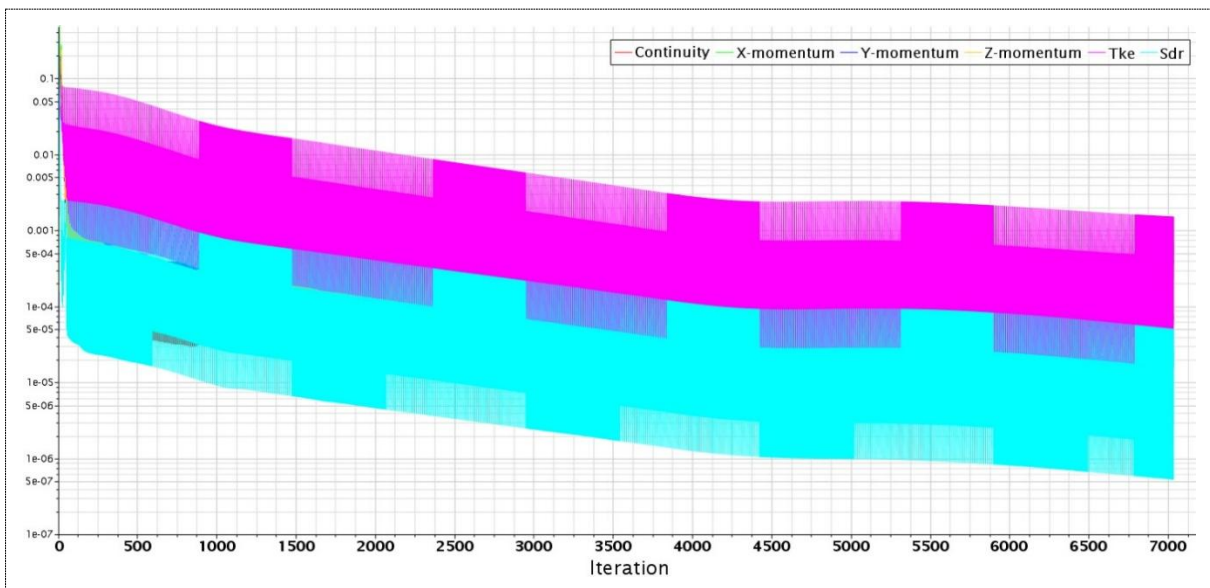
Figure 3.20 Residuals plot of BAR 0.4, J=1.1

The residual in each cell represents the degree to which the discretized equation is satisfied. It has to be noted that the present simulations are performed as unsteady, using implicit solver which performs a number of inner iterations with respect to solution residuals, at each time step. Therefore, at each time step, the first iteration always results in a higher value of residuals, which reduces as iterations progress. Therefore, one can judge solution convergence by the values of residuals from the last inner iterations (lowest values) and overall residual decay pattern. In the plot above, both show very much satisfactory behavior and levels. In such a condition, the simulation time can be reduced significantly.
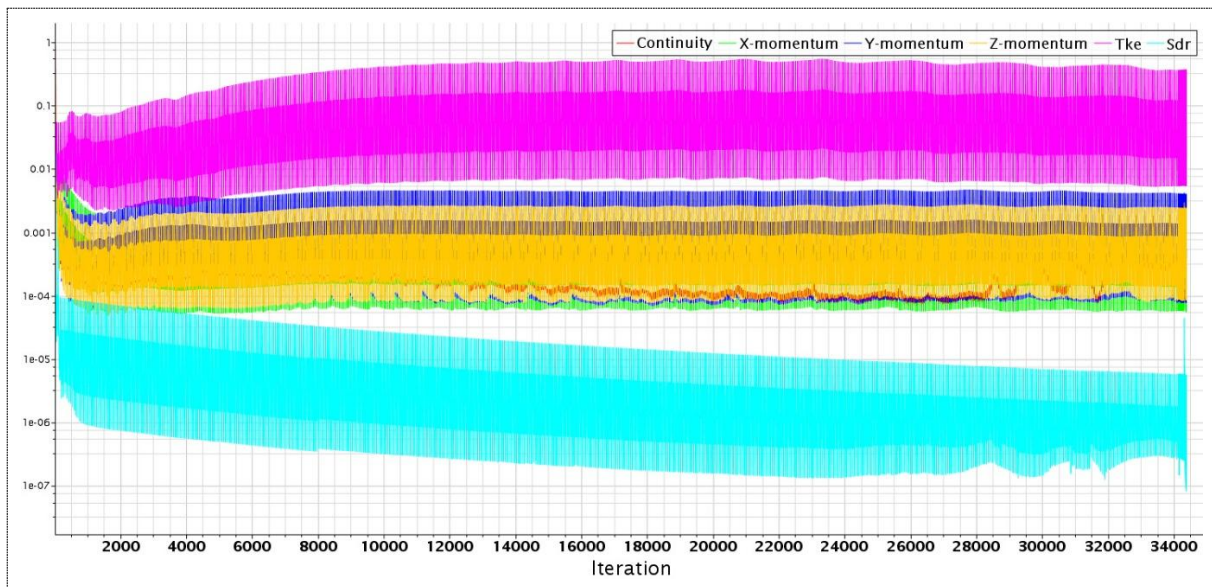
Figure 3.21 Residuals plot of BAR0.4, J=0.1

Figure 3.21 shows the typical residuals plot at J=0.1, when comparing with Figure 3.20 of higher J values, residuals quantities in heavy loading condition didn't have an obvious decay, especially with component 'TKE' keeps increasing. Based on the experience from MARINTEK, this is primarily caused by the leading edge vortex separation phenomenon occurring on this propeller at heavy loading condition. Generation and separation of leading edge vortices is an unsteady phenomenon, associated with increase and time dependent fluctuations of turbulent kinetic energy (TKE) in the domain. That is why the effect is most pronounced in the TKE residual. By using a setup with periodicity condition, and by assigning a fixed (and fairly large) time step we capture unsteadiness only up to a certain time-size scale, while other, smaller scales appear "lost" or "smeared out" from the solution, which causes rise of residuals and their heavy oscillations. The separation phenomenon is expected to be reduced at lower loading condition, hence, residuals part can be found to decrease steadily in Fig.3.20.

The only way to improve the behavior of residuals is to refrain from using periodicity conditions (i.e. use the model of the whole 360 degrees domain), increase mesh fineness to resolve smaller scale vortices, and adjust the time step so that Courant number (CFL) matches that of vortex shedding frequency. However, such a solution would be quite expensive for running systematic calculations.

In the case of heavy loading condition, one can judge the convergence instead by the force prediction, as shown in Part 4.1.1. In conclusion, if one obtains good convergence of propeller force one may

consider the simulation successful and use K_T and K_Q values with good confidence, as long as one is not interested in unsteady flow phenomena in detail.

Warning message

There are two kinds of warning messages in the monitor dialogue during iteration at heavy loading for part of cases.

First, the message "Turbulent viscosity limited on N cells in fluid" is due to the limits set in the solver for the ratio between the turbulent viscosity and dynamic viscosity. If this ratio is too high, the solution will become numerically diffusive, and may occasionally diverge. Note that it does not have much to do with physical effect, but rather a limitation of numerical algorithm, most typical for the class of k-ω turbulence models. The turbulent viscosity ratio tends to increase in high-Re (full scale) flows, at the conditions where vorticity production and separation are greatest (that is why this warning message shows up at low J in full scale). When increasing the limit to a reasonable level, one may avoid the warning message, but it actually affects the results very little. On the cautious side, one is not advised to increase it too high, as this may lead to large numerical diffusion. Practice shows that it is best to keep the original default limits set in the solver, as these are the model parameters which the solver has been validated and tuned with. The limit is found under Solvers->K-Omega Turbulent Viscosity->Maximum Ratio. Alternative way to "help" the solution is to low down the under relaxation factor in the same property group from 1.0 to, for example, 0.7-0.8. But again, no obvious effect on the final solution results.

The other message "Reversed flow on N faces on Outlet boundary" is, on the contrary, a reflection of a physical phenomenon. At low J, where propeller loading is heavy, propeller gives great acceleration to the flow in its slipstream, whereas outside of slipstream, the flow speed is very low. Naturally, due to shear forces between the fluid layers, it may results in reversed flow in the "border zone" between the slipstream and the outer domain. When the reversed flow is detected at the domain Outlet, the solver returns a default warning message, since such reversed fluxes are against the very concept of the "pressure outlet" boundary condition. However, one should not worry too much about it, because these effects are very local, and they are found very far downstream of propeller, so they do not affect flow solution around propeller. This is one reason why the Outlet boundary is placed so far away from propeller.

4. RESULTS

4.1 Plot and Scene

4.1.1 K_T & K_Q plot

The K_T and K_Q plot presented below represents the typical pattern of the force prediction. As shown, both of coefficients monotonically converged to a certain value after a physical time, which seems to be a correct trend. During the iterations, there is a considerable force oscillation at heavy loading condition (J=0.1, 0.3), while at higher J value the predicted force coefficient shows a very stable convergence. The flow separation phenomenon at heavy loading condition is responsible for this.
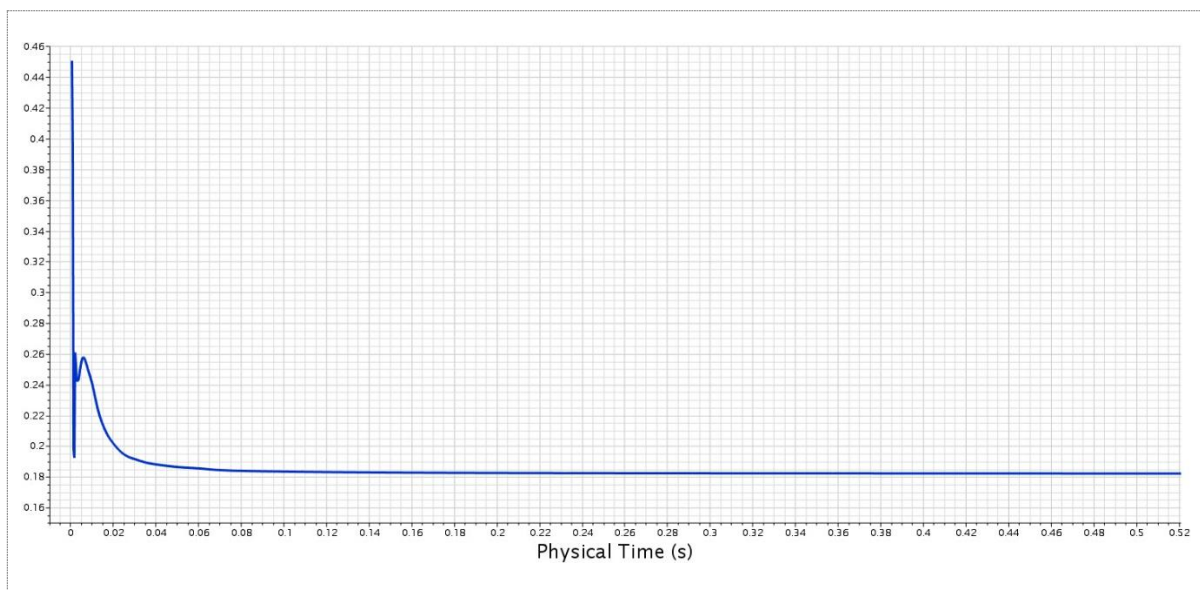
Figure 4.1 Thrust coefficient K_T of BAR 0.4, J=0.9, model scale
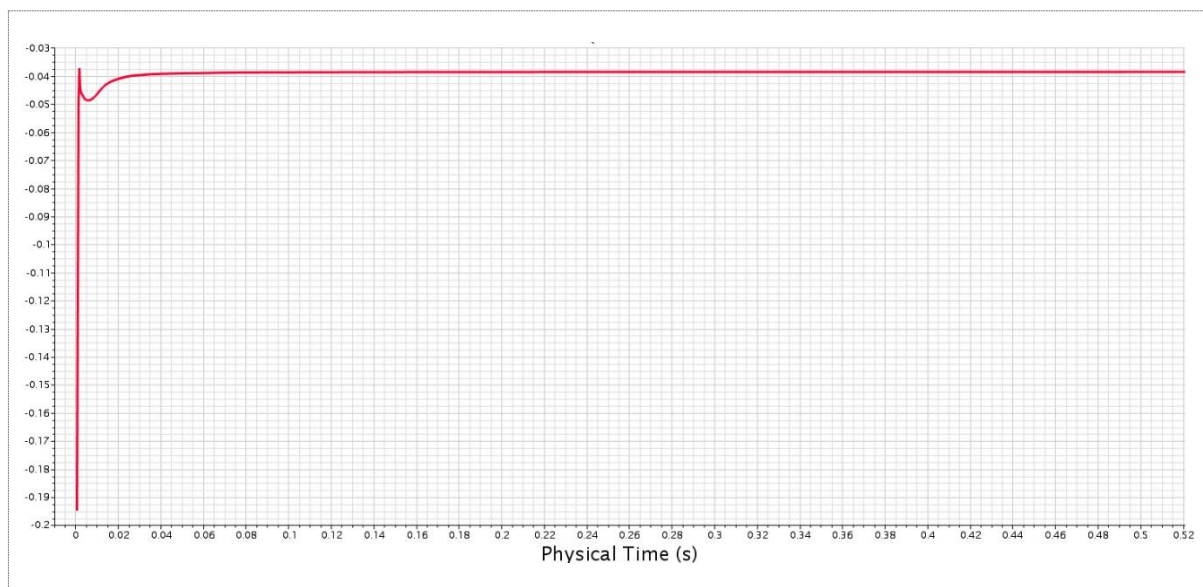
Figure 4.2 Torque coefficient K_Q of BAR 0.4, J=0.9, model scale

4.1.2 Wall y^+

Figure 4.3 and 4.4 present the y^+ distribution in model and full scale respectively. As shown, most region has the desired y^+ value, for model scale $y^+ < 5$, for full scale $5 < y^+ < 300$. It is often inevitable that a few cells have a small value of y^+, especially near stagnation or separation region, which is acceptable.
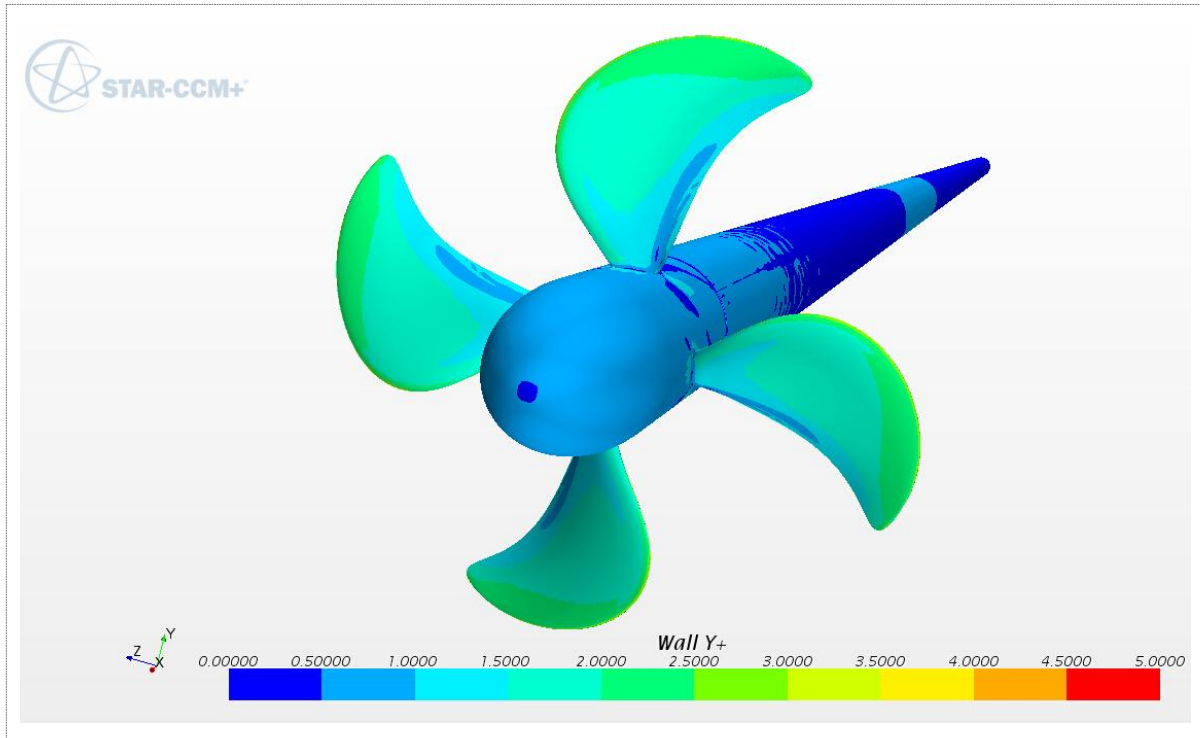
Figure 4.3 Wall y^+ distribution in model scale
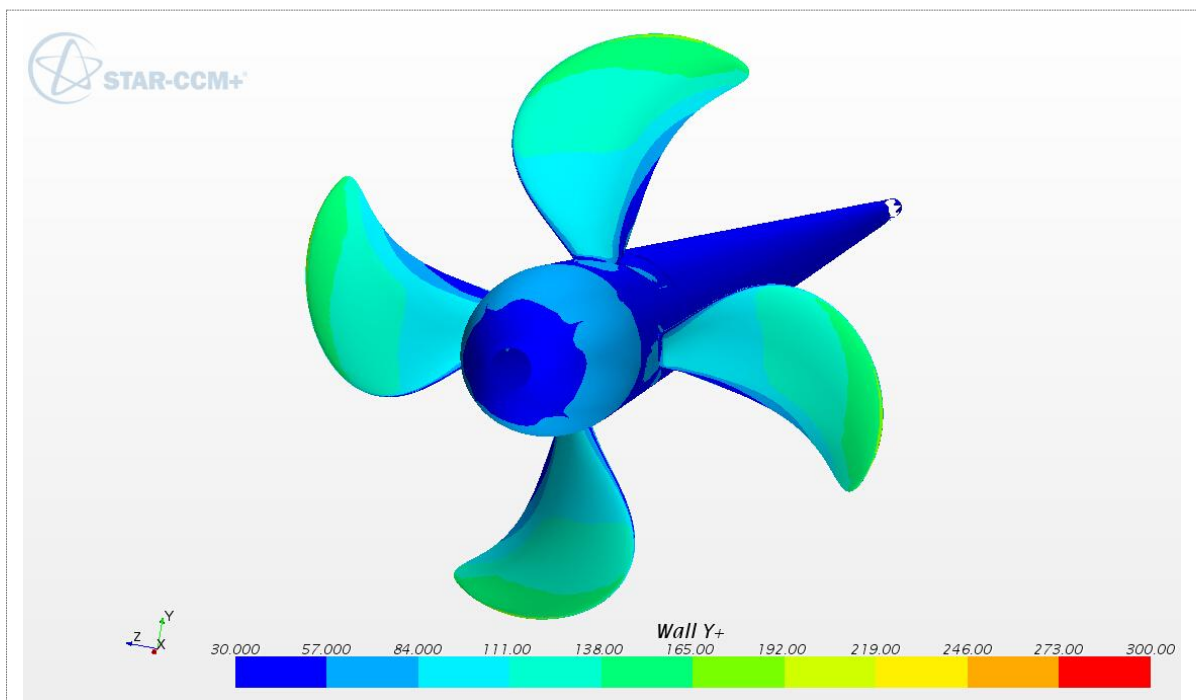
Figure 4.4 Wall y^+ distribution in full scale

4.1.3 Mesh scene in plane XOY

A mesh scene is generated by clipping the plane XOY, it's clear to see polyhedral mesh is created in the center fluid region, extruder mesh is extended from the boundary of Fluid region, which generates the Inlet and Outlet Boundary.
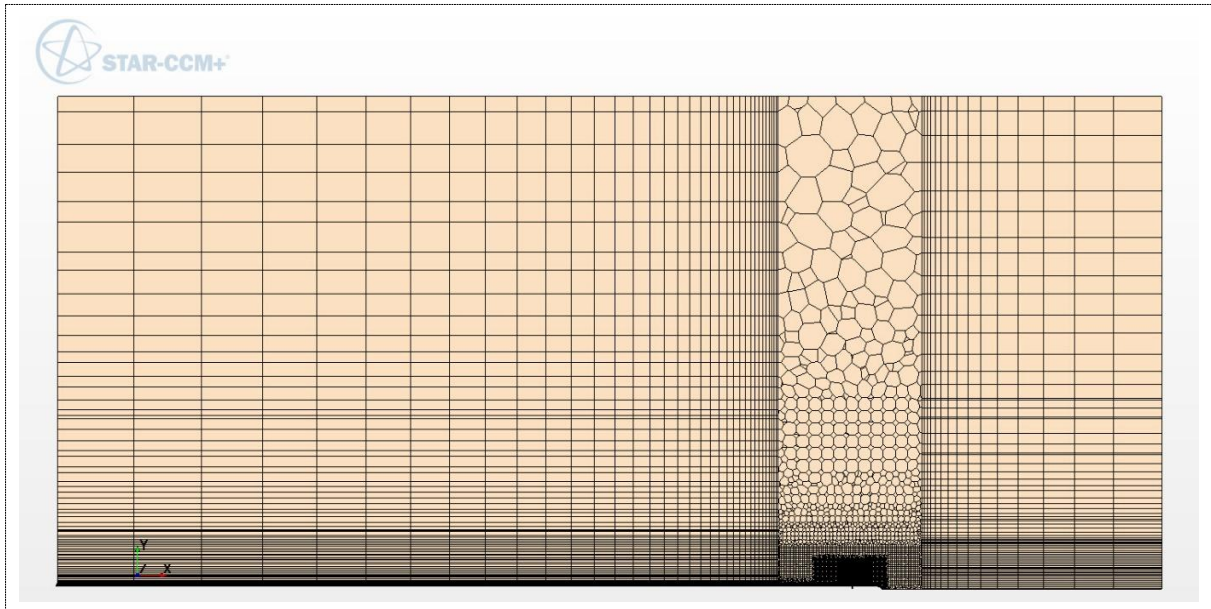
Figure 4.5 Mesh scene in plane XOY

4.1.4 Axial velocity in plane XOY

Figure 4.6 presents the axial velocity filed in plane XOY, at J=0.1. Advance velocity at this condition is -0.375 m/s (-x direction), due to the axial induced acceleration, it is evident to see axial velocity is increased behind propeller blade.
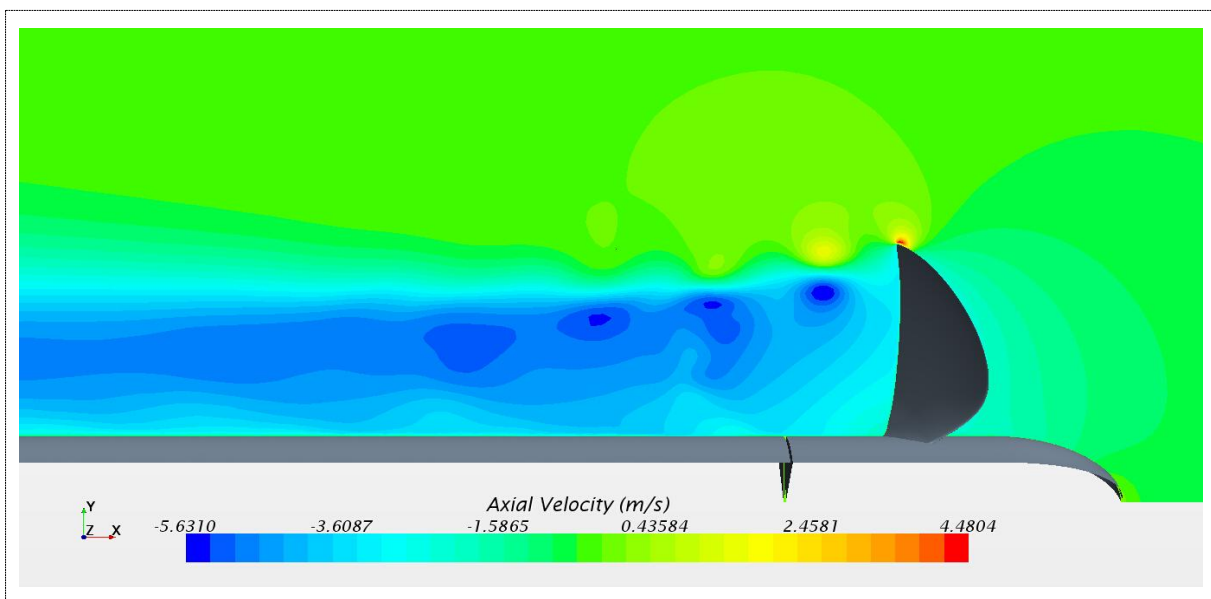
Figure 4.6 Axial velocity distribution in plane XOY, J=0.1, BAR 0.6

4.1.5 Vorticity field in varied loading condition

The group of three figures below shows the vorticity magnitude field of propeller BAR 0.4 in the plane XOY, at various loading conditions. Vorticity is composed by the three components ζ_x, ζ_y and ζ_z.

$$\zeta_x = y'(w) - z'(v)$$
$$\zeta_y = z'(u) - x'(w) \qquad (4.1)$$
$$\zeta_z = x'(v) - y'(u)$$

where u, v and w are velocity components in the x, y and z directions.
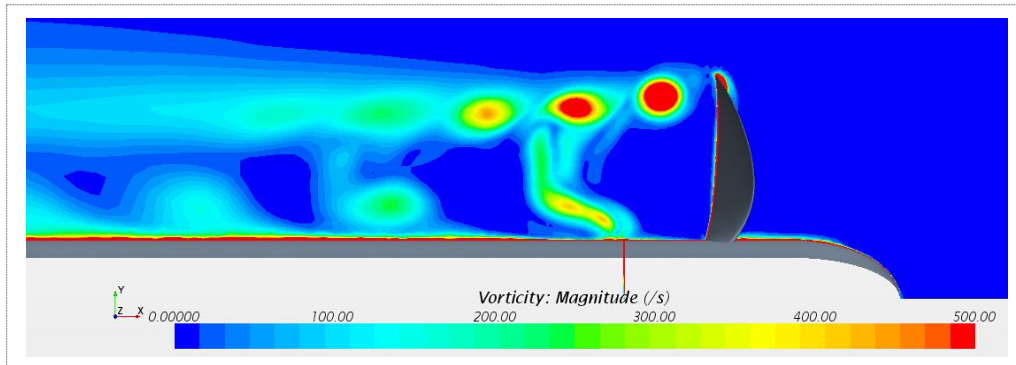
Figure 4.7 Vorticity magnitude of BAR 0.4, J=0.1, model scale
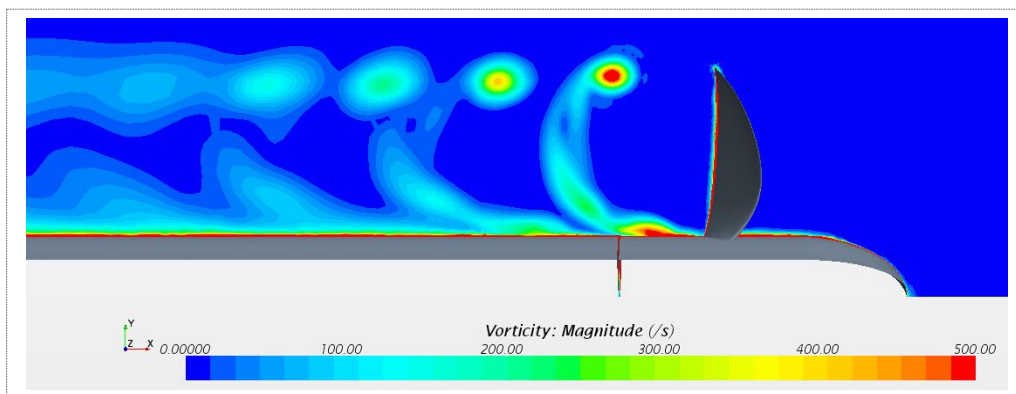
Figure 4.8 Vorticity magnitude of BAR 0.4, J=0.7, model scale
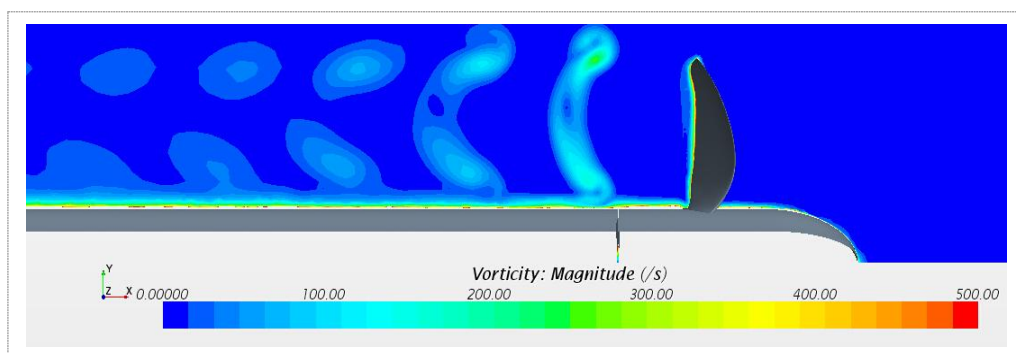
Figure 4.9 Vorticity magnitude of BAR 0.4, J=1.1, model scale

4.1.6 Tip vortex

The tip vortex flowfield in the vicinity of the tip region is a very complicated three-dimensional viscous flow phenomenon. It can significantly affect the performance of marine propeller.
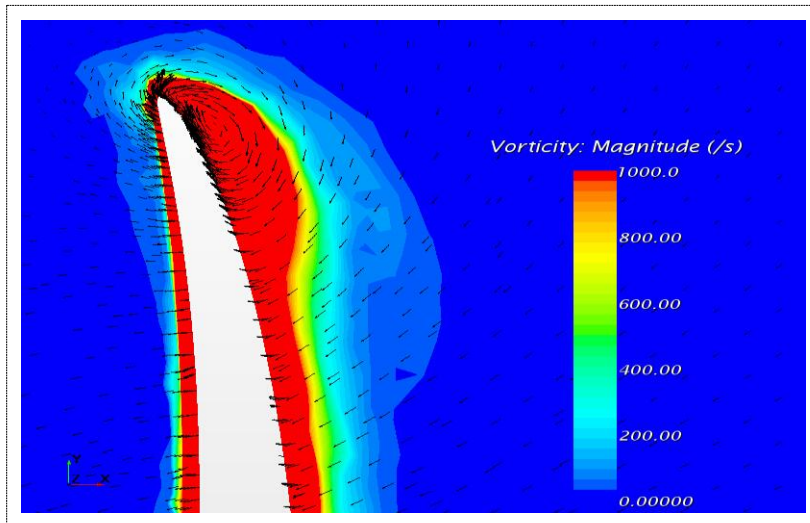
Figure 4.10 Tip vortex of BAR 0.4, J=0.1, model scale
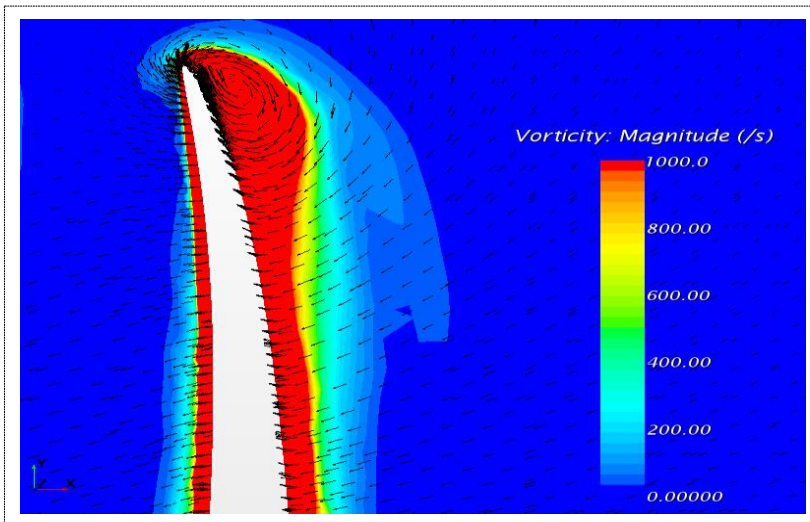
Figure 4.11 Tip vortex of BAR 0.6, J=0.1, model scale
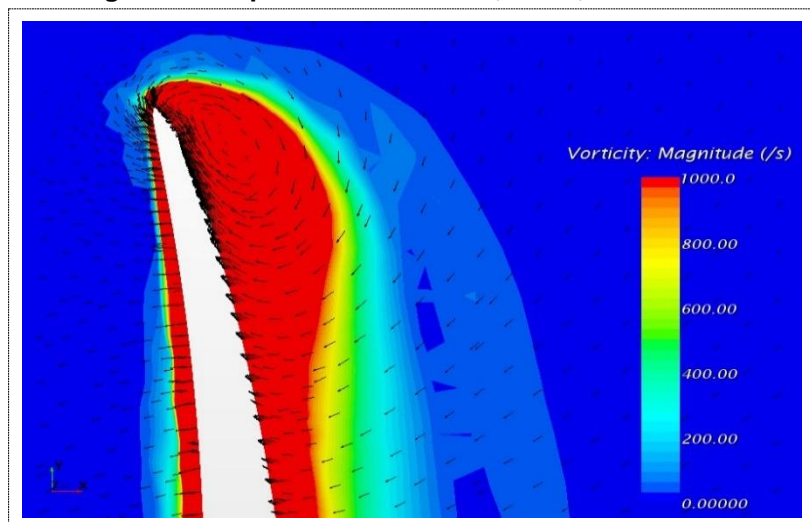
Figure 4.12 Tip vortex of BAR 0.8, J=0.1, model scale

4.1.7 Flow separation

Flow separation phenomenon occurs when the boundary layer travels far enough against an adverse pressure gradient that the speed of the boundary layer relative to the object falls almost to zero. By comparing the figures below, it can be concluded, in the present case, flow separation mainly happens at the leading edge at outer blade sections under heavy loading condition (low J value).
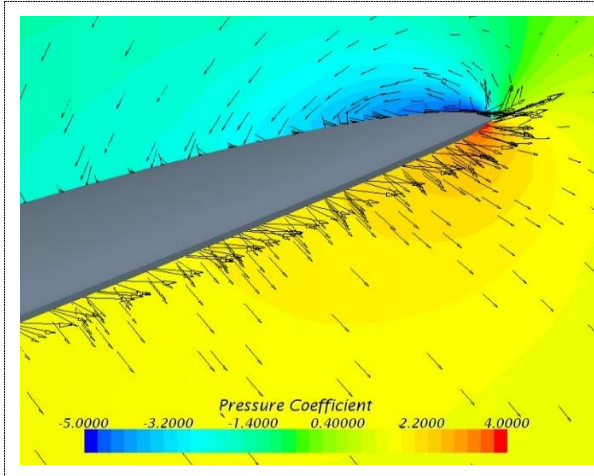
Figure 4.13 J=0.1, blade section 0.7R
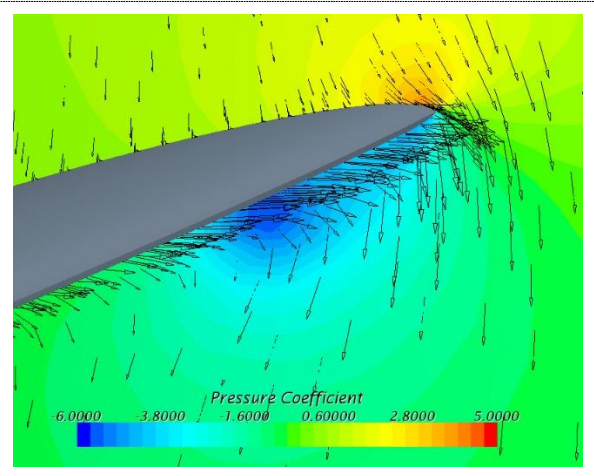
Figure 4.14 J=1.1, blade section 0.7R
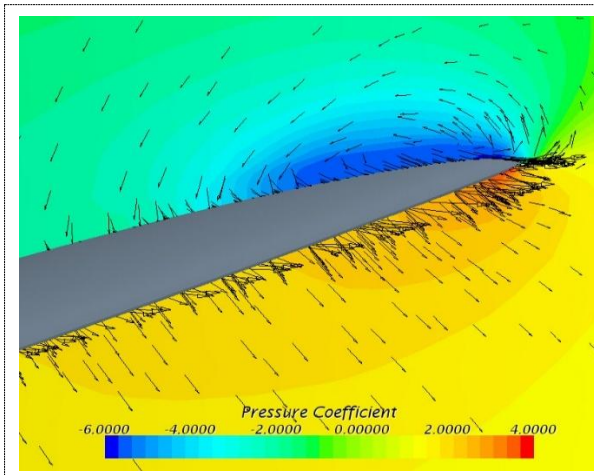
Figure 4.15 J=0.1, blade section 0.8R
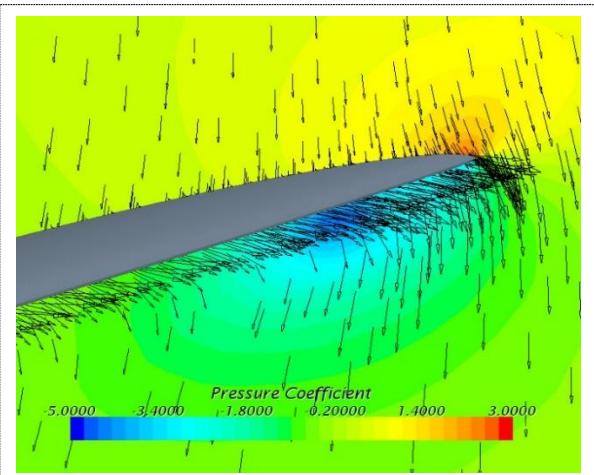
Figure 4.16 J=1.1, blade section 0.8R
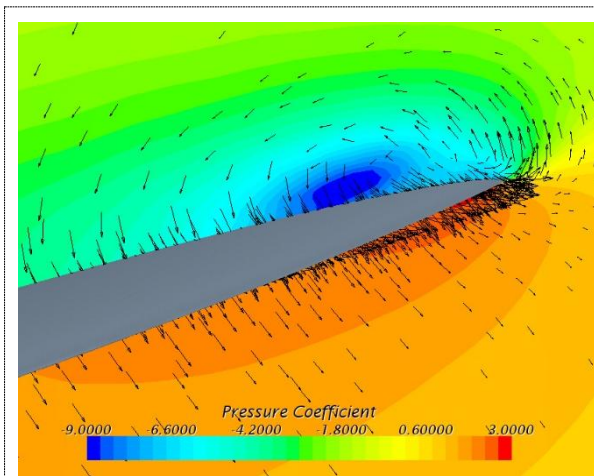
Figure 4.17 J=0.1, blade section 0.9R
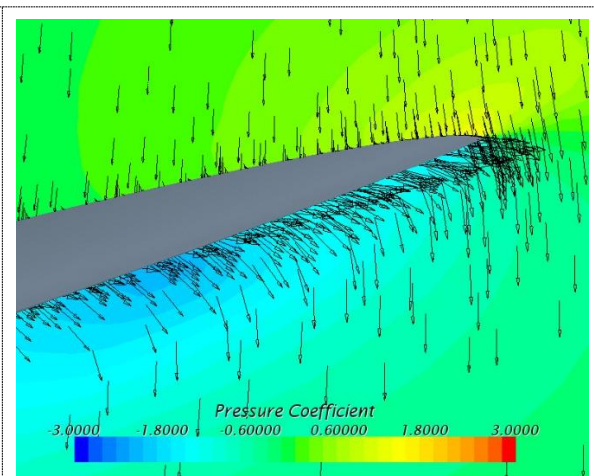
Figure 4.18 J=1.1, blade section 0.9R

4.1.8 Pressure distribution

The group of diagrams demonstrate the pressure distribution at 0.7R, at J=0.7, for studied propellers.

The non-dimensional form of pressure coefficient is defined as

$$C_P = \frac{P - P_{ref}}{1/2 \cdot \rho(nD)^2}$$

Pressure distribution at 0.9R can be found in Appendix C.
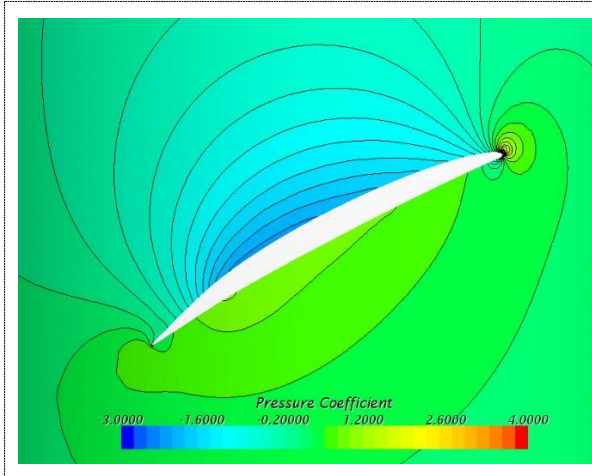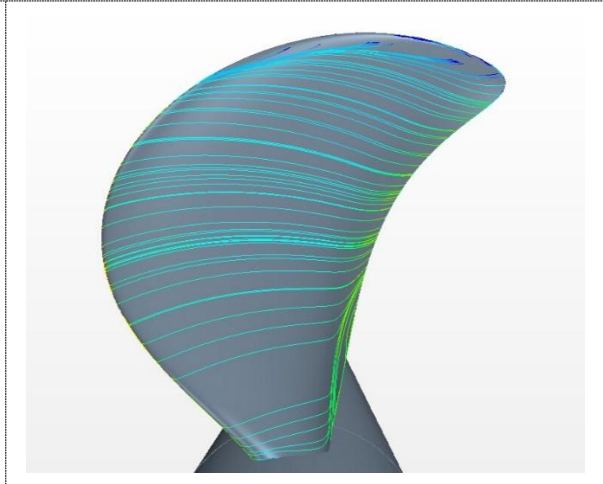

Figure 4.19 BAR 0.4, Model Scale
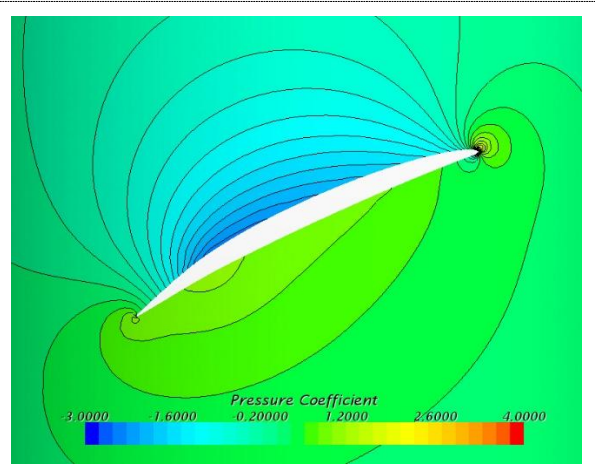
Figure 4.20 BAR 0.4, Full Scale
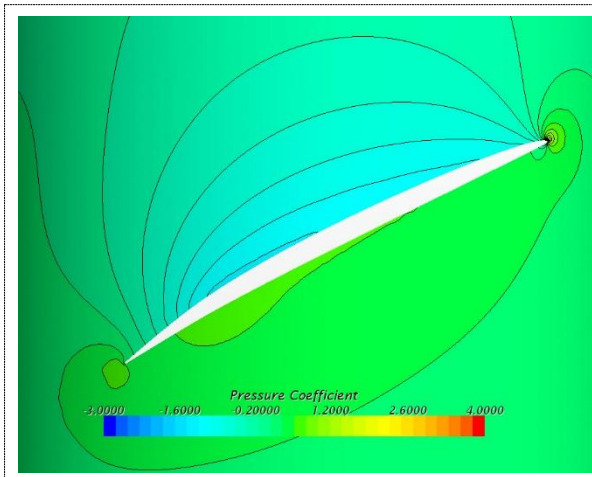
Figure 4.21 BAR 0.6, Model Scale
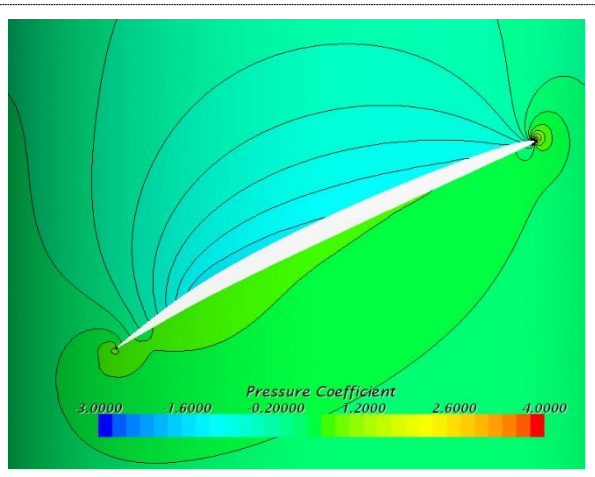
Figure 4.22 BAR 0.6, Fulll Scale
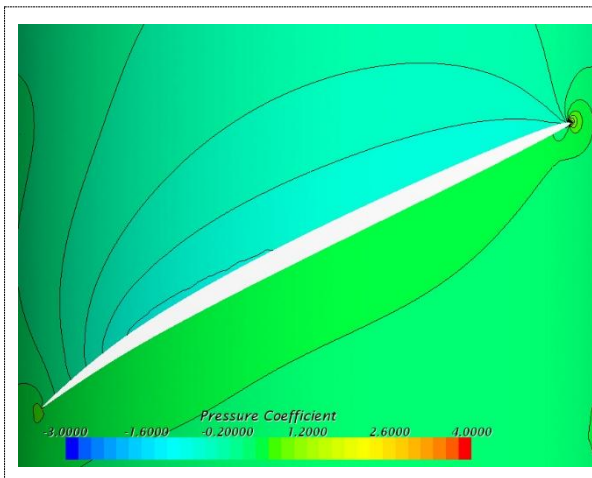
Figure 4.23 BAR 0.8, Model Scale
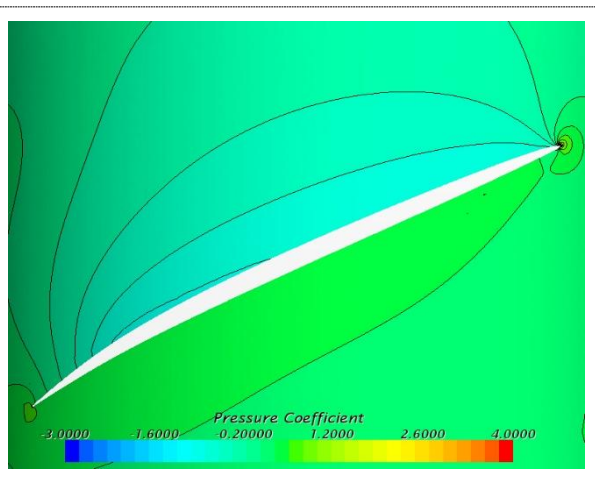
Figure 4.24 BAR 0.8, Full Scale

4.1.9 Constrained streamlines on blade

The group of figures present the pressure distribution and constrained streamlines on propeller blades for the three propellers in model and full scale, at the J=0.5. Trailing edge radial flow pattern can be compared between model and full scale.
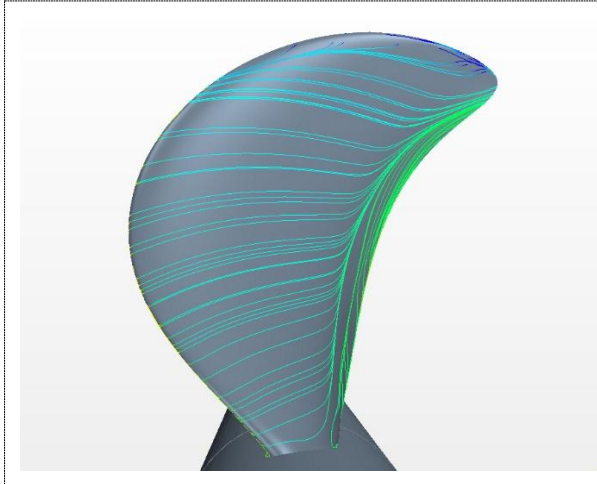
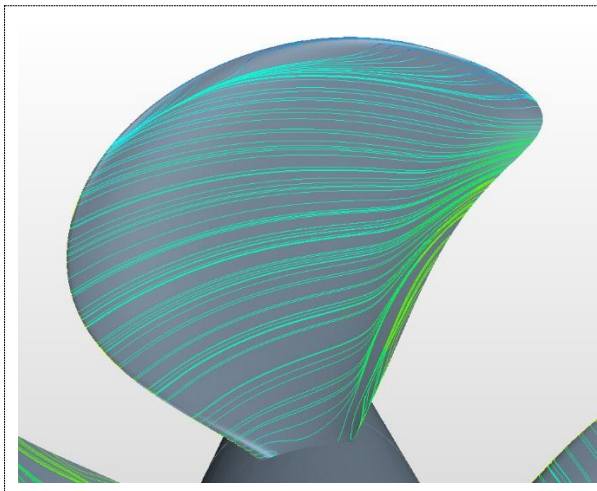**Figure 4.25 BAR 0.4, Model Scale**

Figure 4.26 BAR 0.4, Full Scale

Figure 4.27 BAR 0.6, Model Scale
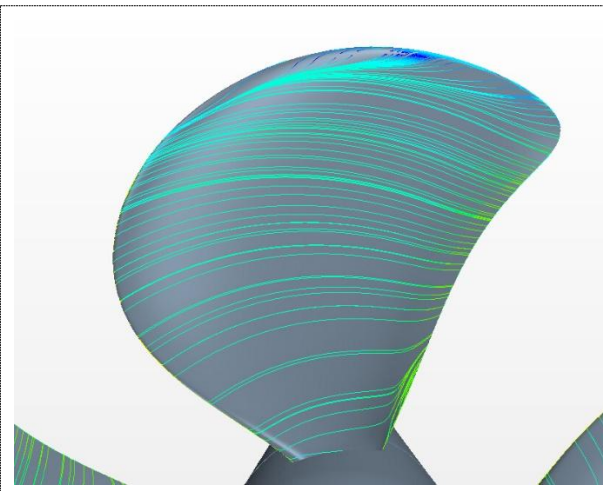
Figure 4.28 BAR 0.6, Full Scale
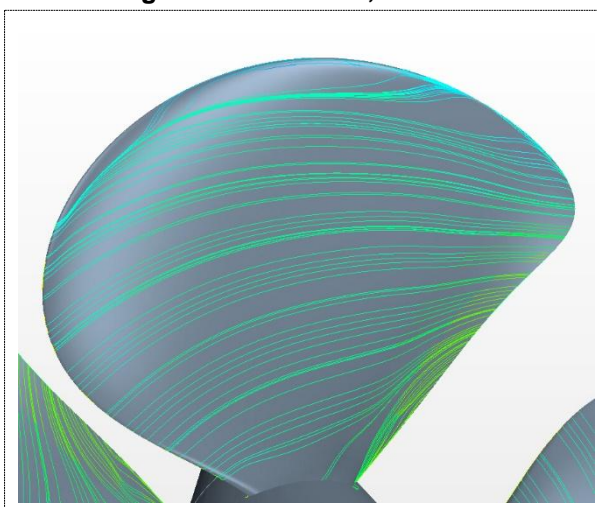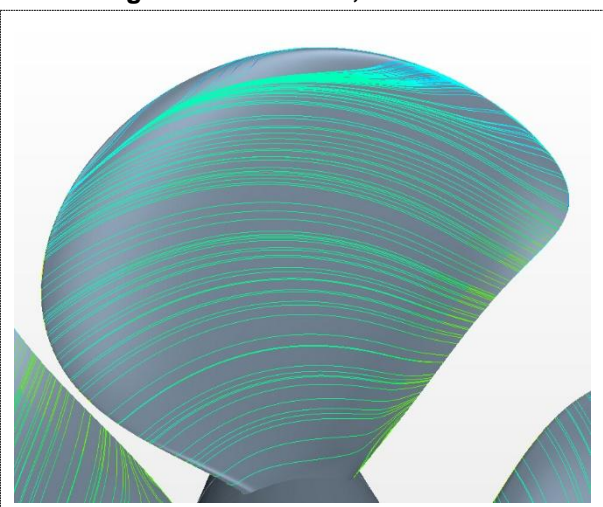

Figure 4.29 BAR 0.8, Model Scale

Figure 4.30 BAR 0.8, Full Scale

The group of figures shows trailing edge radial flow pattern at different loading condition for BAR 0.6 in model scale, it can be seen trailing edge radial flow is getting weak as J increases. It can be explained by the larger Reynolds number at higher J value (though advance velocity is normally neglected when calculating propeller Re, the actual Re is larger at higher J). At the loading condition J=0.1,and 0.3, streamline seems absent on the leading edge region, this can be explained by the separated flow.
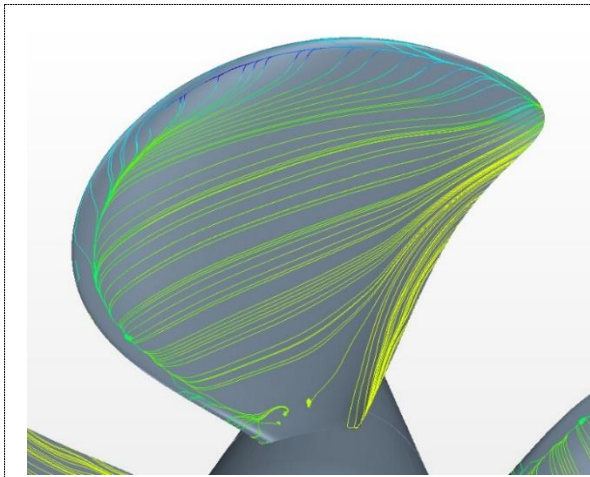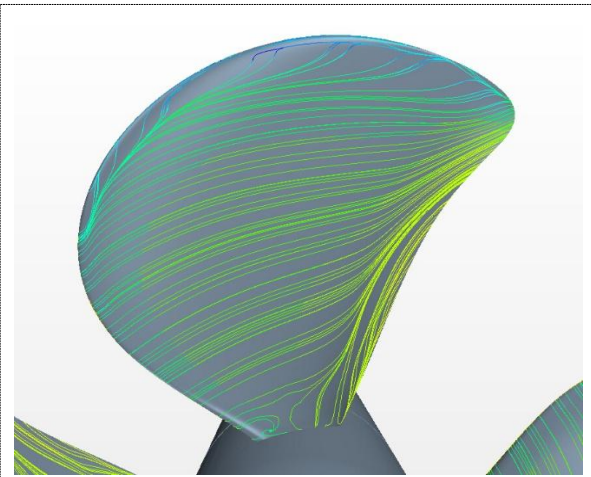

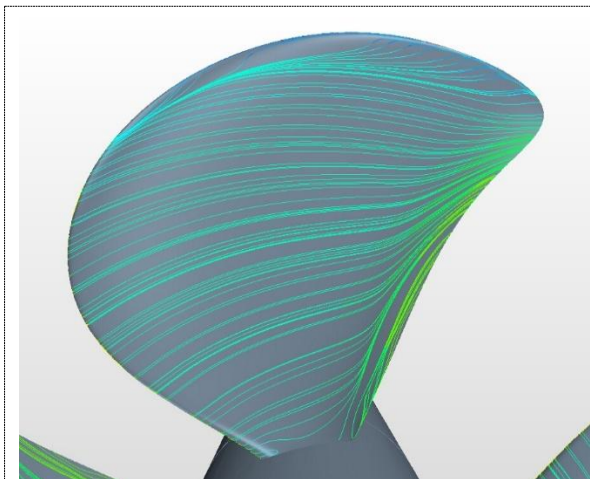**Figure 4.31 Constrained streamline at J=0.1**   **Figure 4.32 Constrained streamline at J=0.3**
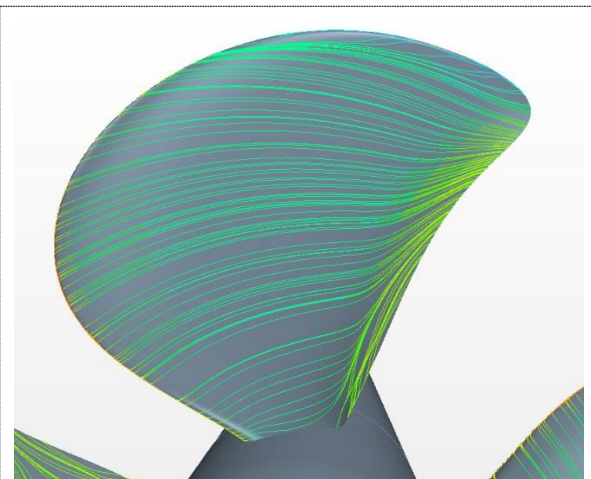
Figure 4.33 Constrained streamline at J=0.5   **Figure 4.34 Constrained streamline at J=0.7**
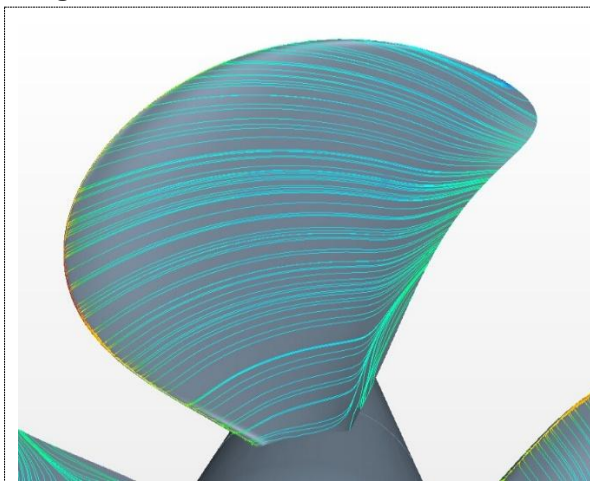
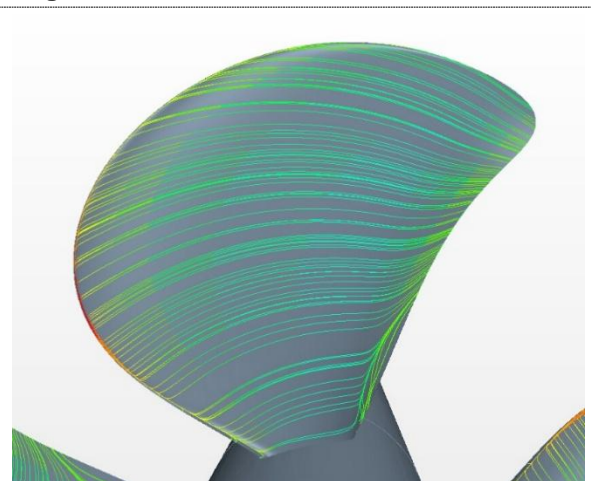**Figure 4.35 Constrained streamline at J=0.9**   **Figure 4.36 Constrained streamline at J=1.1**

4.1.10 Vorticity magnitude at section 0.7R

The vorticity magnitude in its non-dimensional form (Vorticity/n, where n is the propeller RPS) at certain foil section give an illustration of the boundary layer thickness in model and full scale. Turbulent boundary layer shows a much higher level of vorticity compared to the surrounding freestream. By virtue of this, boundary layer thickness in full scale appears to be showing a reduced thicnkess compared to model scale, and the reduction is most evident for BAR 0.4.
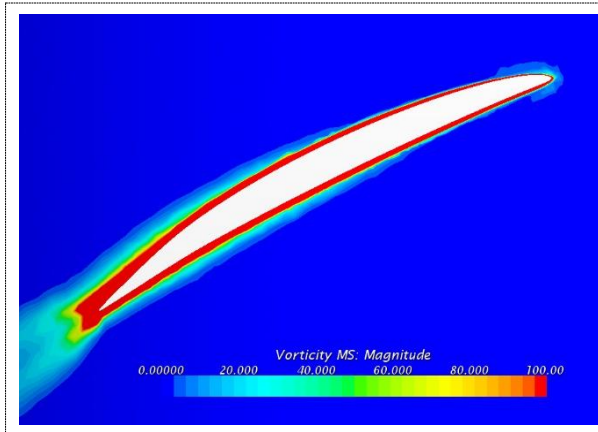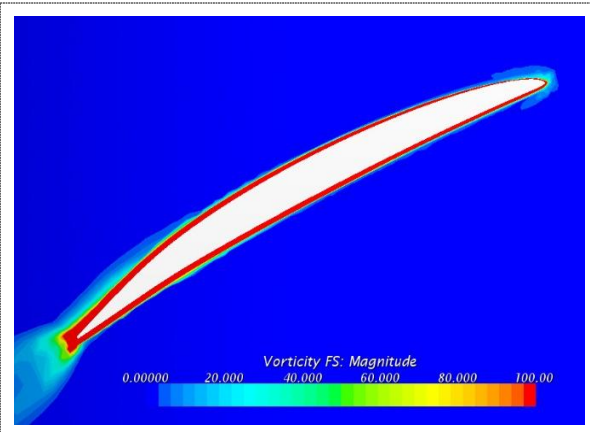

Figure 4.37   BAR 0.4, Model Scale
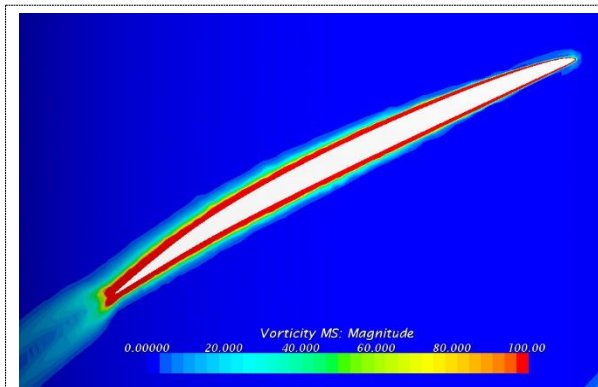

Figure 4.38 BAR 0.4, Full Scale

Figure 4.39 BAR 0.6, Model Scale
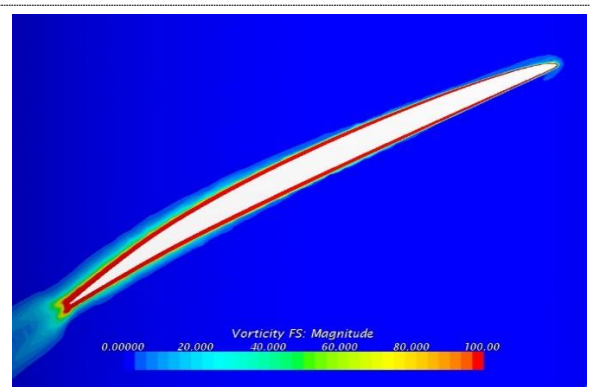
Figure 4.40 BAR 0.6, Full scale
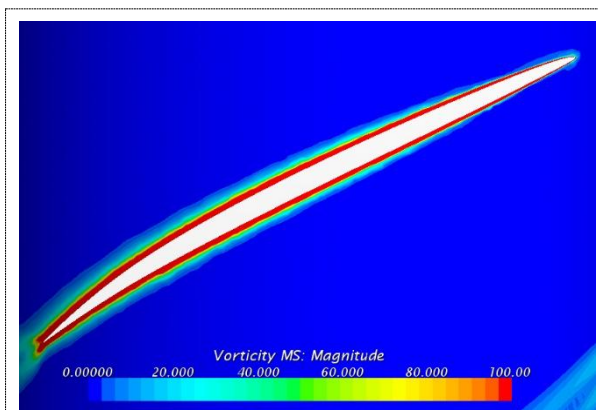
Figure 4.41 BAR 0.8, Model Scale
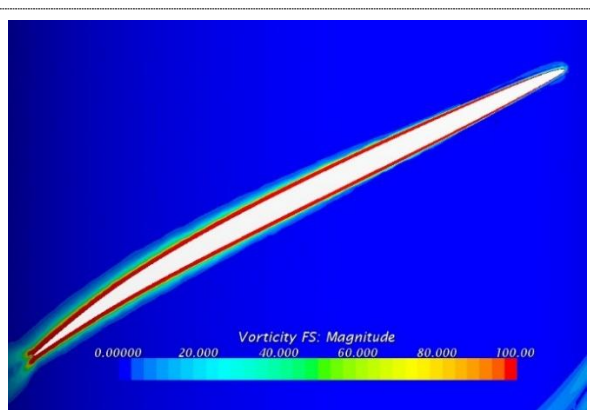
Figure 4.42 BAR 0.8, Fulll Scale

4.1.11 Trailing vortices

Trailing vortices in propeller wake is a physical phenomenon of great interest to be investigated, it is recognized to have considerable effect on propeller performance, like lift force. The present group of figures show the trailing vortices by volume rendering method in STAR-CCM+ for all studied propellers in both model and full scale. One can find the pitch of trailing vortices is larger in full scale, and it is believed to be associated with trailing edge radial flow observed on suction side.

Figure 4.43 BAR0.4, Model scale

Figure 4.44 BAR0.4, Model scale
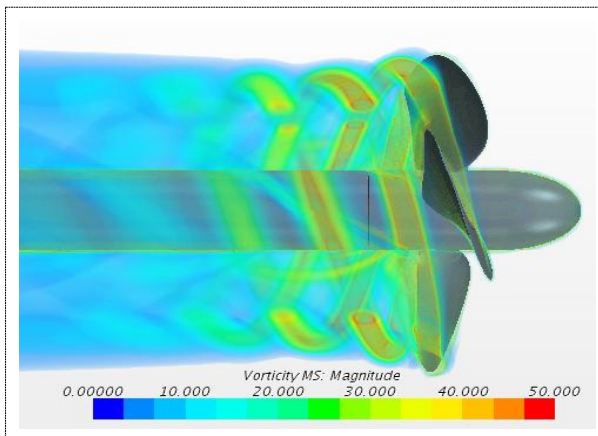
Figure 4.45 BAR0.6, Model scale
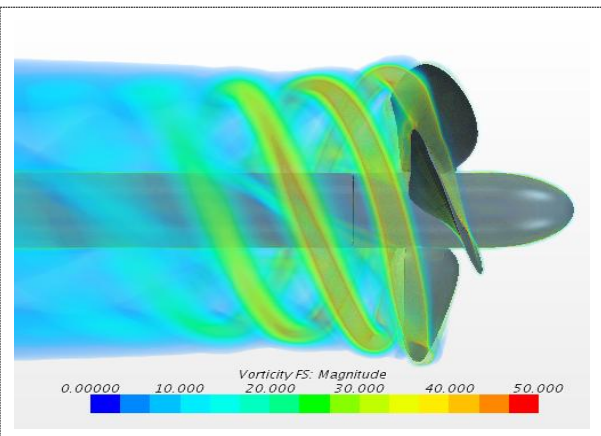
Figure 4.46 BAR0.6, Full scale
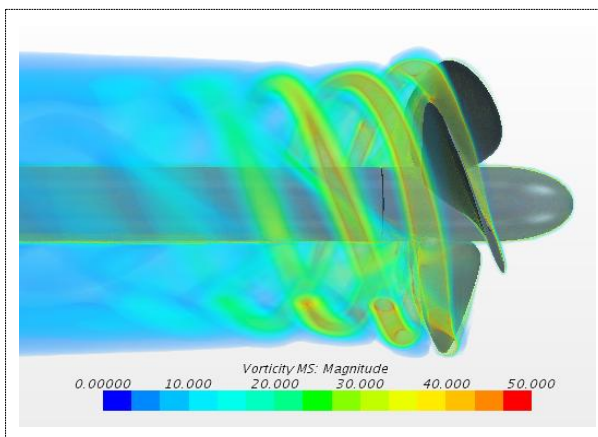
Figure 4.47 BAR0.8, Model scale
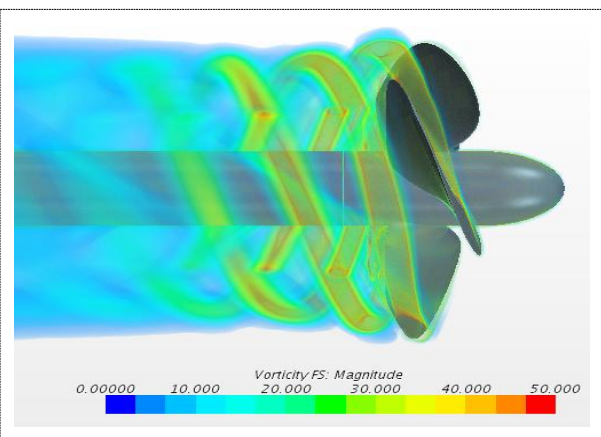
Figure 4.48 BAR0.8, Full scale

4.2 Propeller open water characteristics

Table 4.1 and Table 4.2 list the calculated open water characteristics of propeller with BAR 0.4, 0.6 and 0.8, in model scale and full scale. The numerical calculations are performed under the condition of n=15Hz.

Table 4.1 Open water characteristics in model scale (MS)

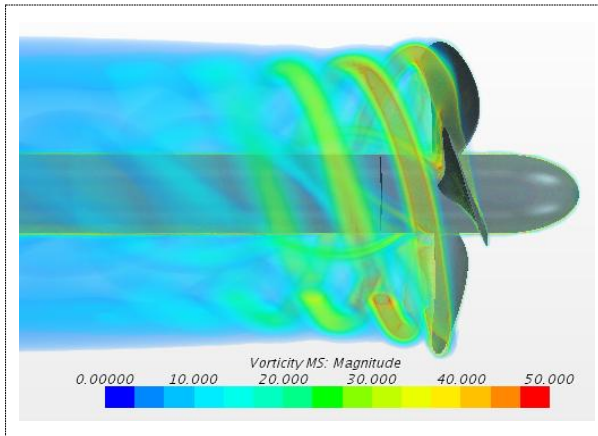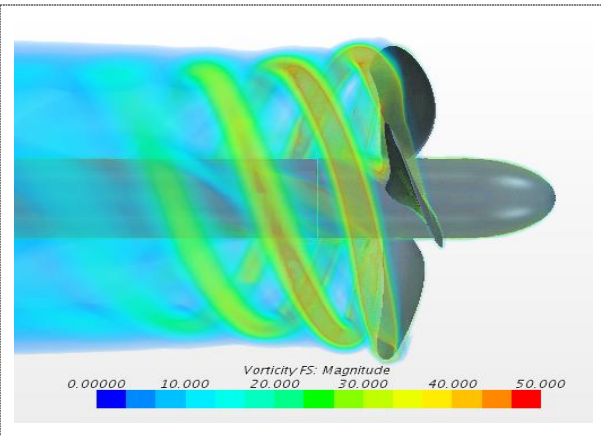|	**BAR 0.4**			**BAR 0.6**			**BAR 0.8**		
J	K_T	K_Q	η_0	K_T	K_Q	η_0	K_T	K_Q	η_0
0.1	0.5208	0.0781	0.1061	0.5843	0.0911	0.1021	0.6130	0.0975	0.1001
0.3	0.4368	0.0681	0.3063	0.4804	0.0770	0.2979	0.4964	0.0806	0.2941
0.5	0.3542	0.0591	0.4767	0.3751	0.0634	0.4708	0.3794	0.0646	0.4677
0.7	0.2713	0.0498	0.6069	0.2723	0.0501	0.6055	0.2651	0.0491	0.6016
0.9	0.1822	0.0385	0.6779	0.1725	0.0365	0.6766	0.1585	0.0341	0.6652
1.1	0.0796	0.0248	0.5619	0.0583	0.0204	0.5003	0.0391	0.0171	0.4008

Table 4.2 Open water characteristics in full scale (FS)

	BAR 0.4			**BAR 0.6**			**BAR 0.8**		
J	K_T	K_Q	η_0	K_T	K_Q	η_0	K_T	K_Q	η_0
0.1	0.5515	0.0817	0.1074	0.5965	0.0913	0.1040	0.6222	0.0969	0.1022
0.3	0.4679	0.0721	0.3099	0.4937	0.0776	0.3038	0.5041	0.0798	0.3015
0.5	0.3830	0.0628	0.4853	0.3893	0.0642	0.4825	0.3877	0.0639	0.4828
0.7	0.2974	0.0530	0.6251	0.2876	0.0510	0.6283	0.2748	0.0486	0.6297
0.9	0.2079	0.0418	0.7124	0.1868	0.0372	0.7193	0.1689	0.0337	0.7173
1.1	0.1037	0.0278	0.6531	0.0724	0.0210	0.6036	0.0504	0.0167	0.5290
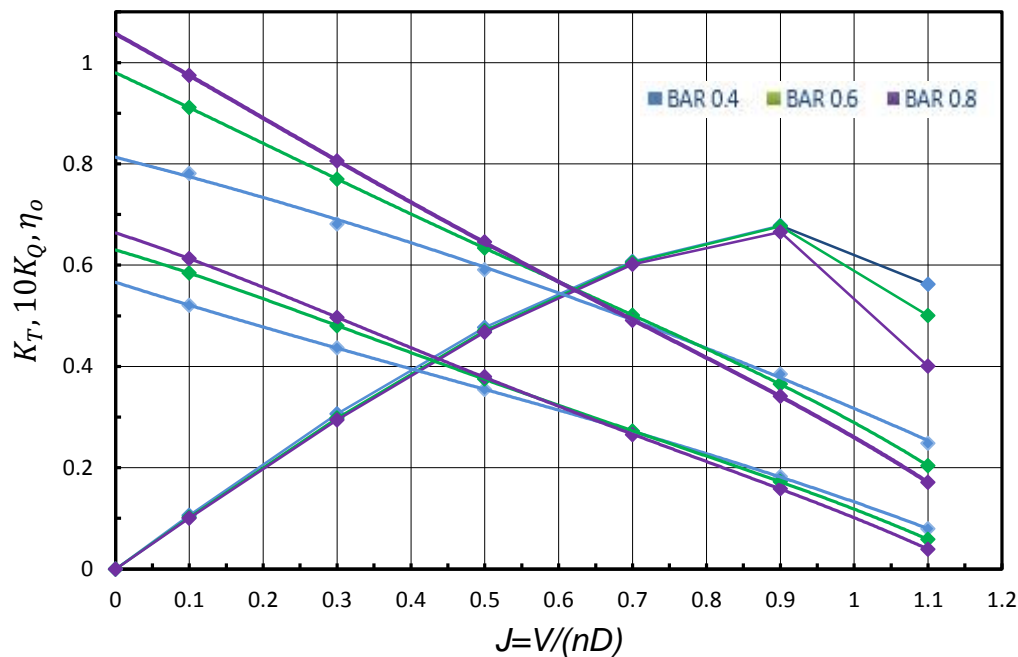
Figure 4.49 Open water characteristics of propellers with varied BAR, Model scale

Propeller 11 represents the propeller with BAR 0.6. Propeller 12 denotes the propeller 11 with alternative chord length distribution. Table 4.3 lists the open water characteristics of propeller 12, propeller 11 with two-blades-split simulation domain and propeller 11 itself.

By comparing the calculated force from one-blade-passage and two-blades-split domain, the two considered setups bring very close, practically identical results.

Table 4.3 open water characteristics of propeller 11, 12 and 11 with two-blades-split domain

J	Propeller 12(BAR 0.6)			Propeller 11(BAR 0.6)			Two-blades-split domain		
	K_T	K_Q	η_0	K_T	K_Q	η_0	K_T	K_Q	η_0
0.1	0.5532	0.0862	0.1021	0.5843	0.0911	0.1021	0.5831	0.0907	0.1023
0.3	0.4617	0.0739	0.2984	0.4804	0.0770	0.2979	0.4795	0.0767	0.2985
0.5	0.3663	0.0616	0.4731	0.3751	0.0634	0.4708	0.3744	0.0632	0.4714
0.7	0.2706	0.0492	0.6127	0.2723	0.0501	0.6055	0.2714	0.0498	0.6072
0.9	0.1732	0.0359	0.6907	0.1724	0.0365	0.6766	0.1714	0.0362	0.6782
1.1	0.0628	0.0202	0.5440	0.0583	0.0204	0.5003	0.0579	0.0202	0.5018
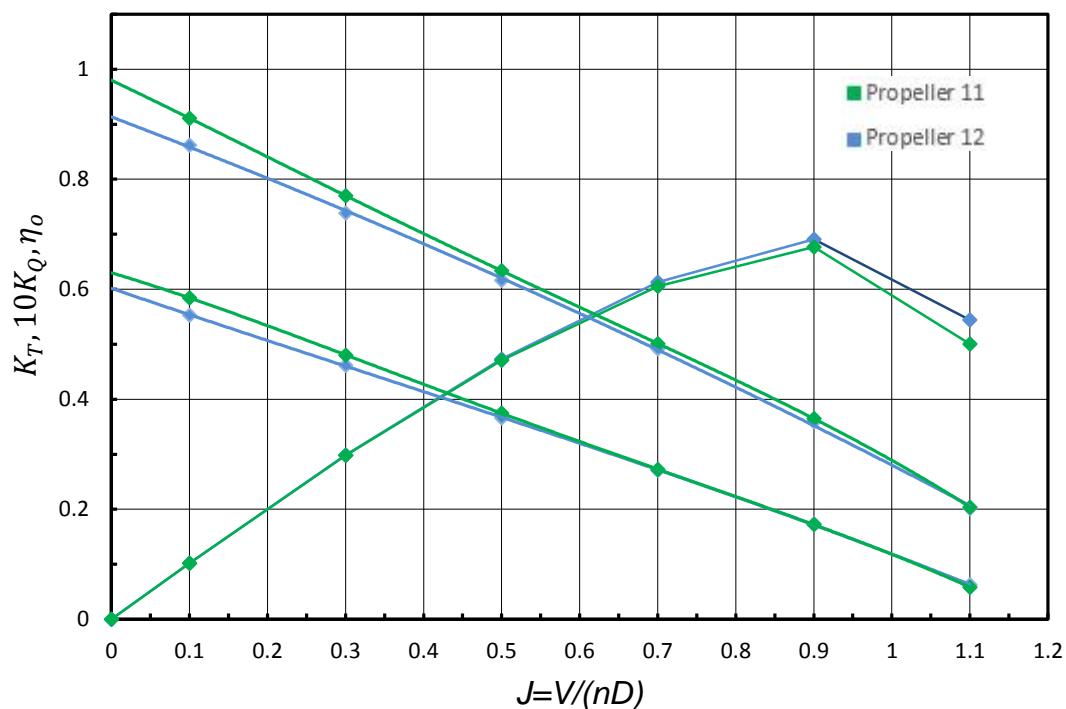
Figure 4.50 Open water characteristics of propeller 11 and propeller 12

Relative difference in propeller force

The comparison between model and full scale open water propeller characteristics was made in the form of relative difference in percent $\left((K_S - K_M)/K_M\right) \times 100$. Considered that absolute value of propeller force is relative small at J=1.1, and division by a small value will result a significantly large difference in percent. For this reason, data of J=1.1 is not included in these diagrams. Figure 4.51, 4.52 and 4.53 present relative difference between model and full scale thrust, torque and efficiency respectively, for propeller with BAR 0.4, 0.6 and 0.8.   Figure 4.54, 4.55 and 4.56 present relative difference between model and full scale thrust, torque and efficiency respectively, for propeller 11 and 12.
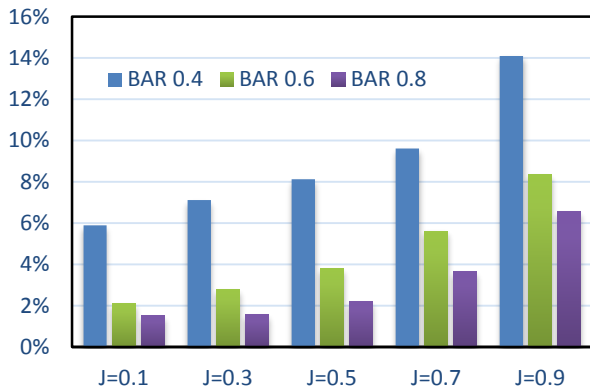
Figure 4.51 relative difference in thrust
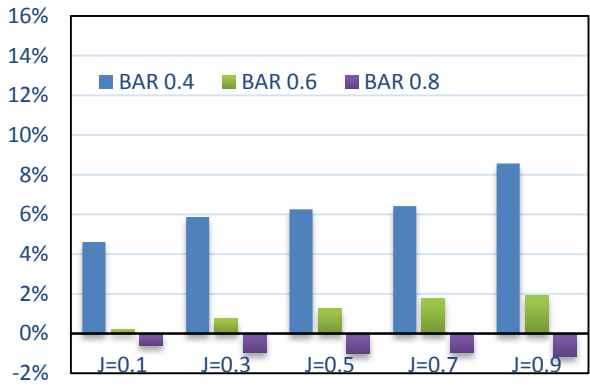
Figure 4.52 relative difference in torque
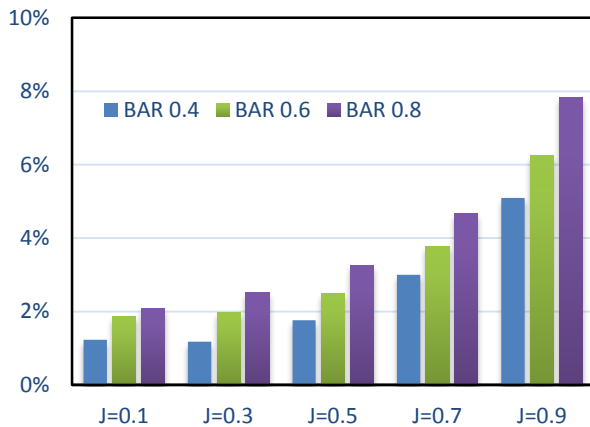
Figure 4.53 relative difference in efficiency
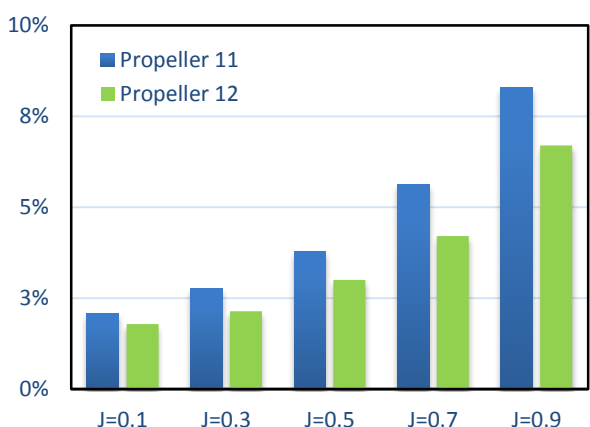
Figure 4.54 relative difference in thrust
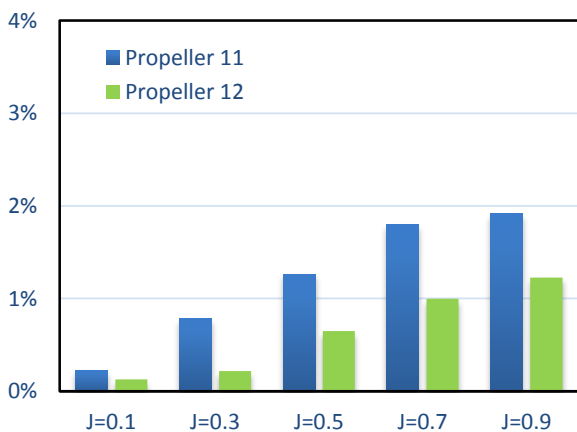
Figure 4.55 relative difference in torque
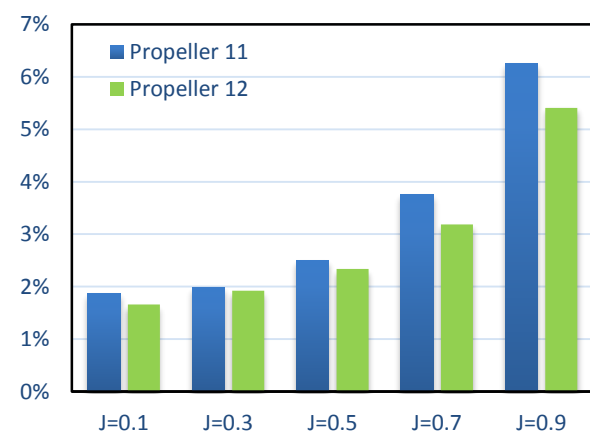
Figure 4.56 relative difference in efficiency

49

When compare the scale effect on propeller 11 and 12, it is beneficial to demonstrate the trailing edge radial flow and chordwise pressure distribution. Figure 4.57-4.60 present the difference of flow behaviors between propeller 11 and 12, in model and full scale, at selected loading condition J=0.5.

Constrained streamline on blade
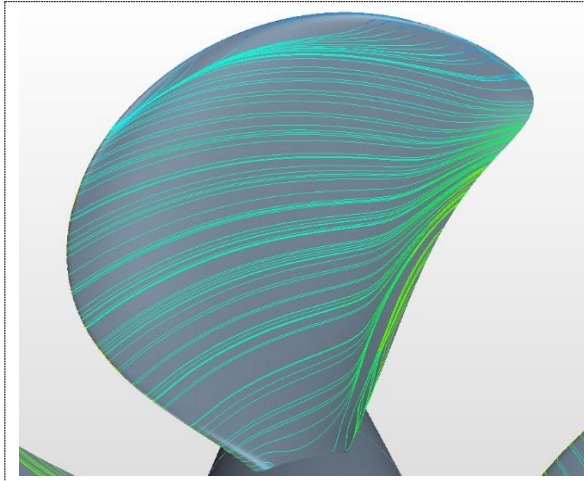
Figure 4.57 Propeller 11, Model scale
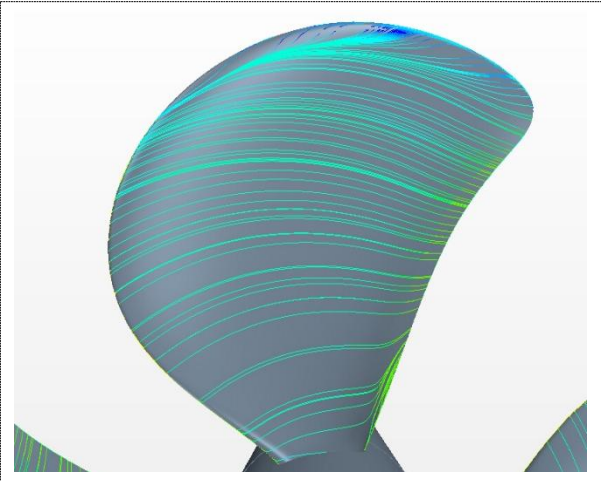
Figure 4.58 Propeller 11, Full scale
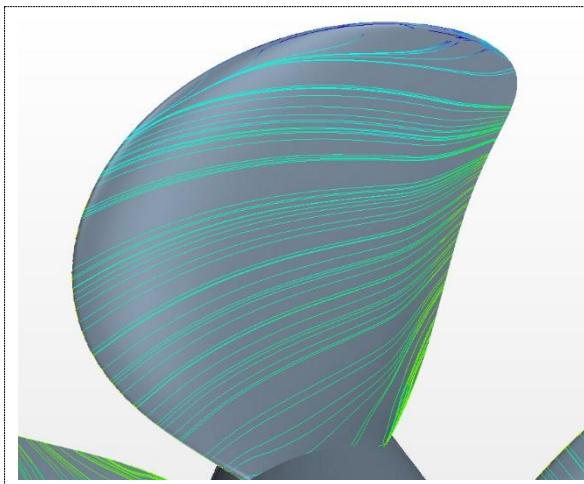
Figure 4.59 Propeller 12, Model scale
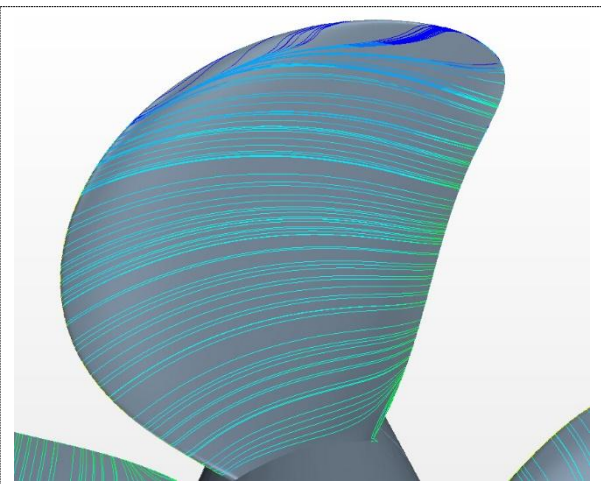
Figure 4.60 Propeller 12, Full scale

Figure 4.61-4.63 present the different chordwise pressure distribution in propeller 11 and 12, at blade section 0.4R, 0.5R and 0.95R, under the loading condition J=0.1. Information at section 0.7R and 0.9R are included in the Figure 5.10-11, Chapter 5. The pressure coefficient is in its non-dimensional form:

$$C_P = \frac{P - P_{ref}}{1/2 \cdot \rho (nD)^2}$$

where reference pressure P_{ref} is zero, n represents propeller RPS, D is propeller diameter.
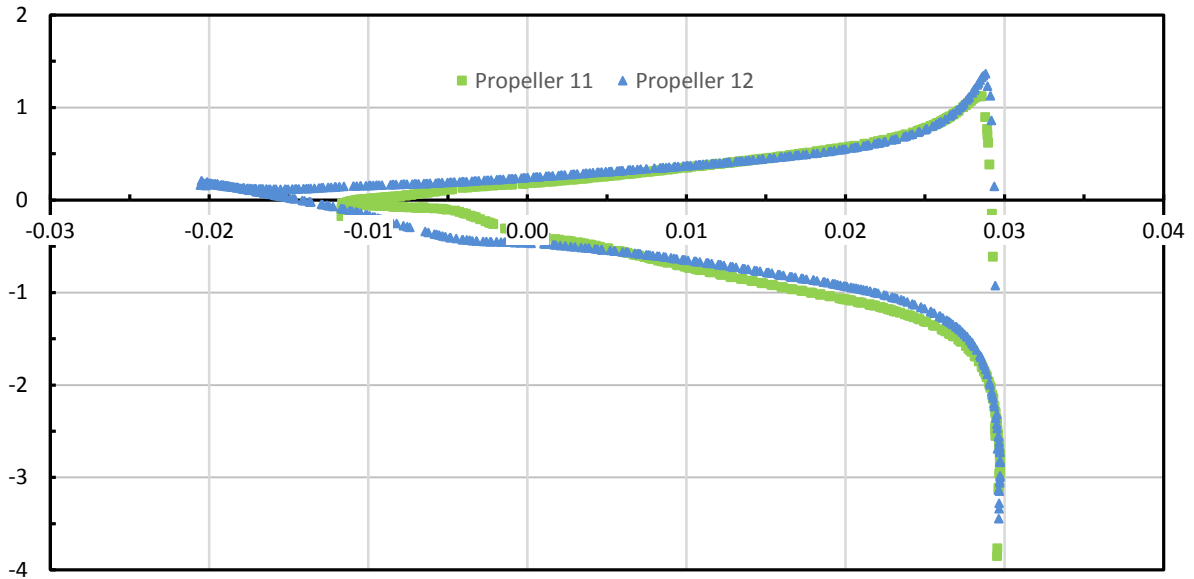
Figure 4.61 Pressure distribution along the blade section of propeller 11 and 12, section 0.4R
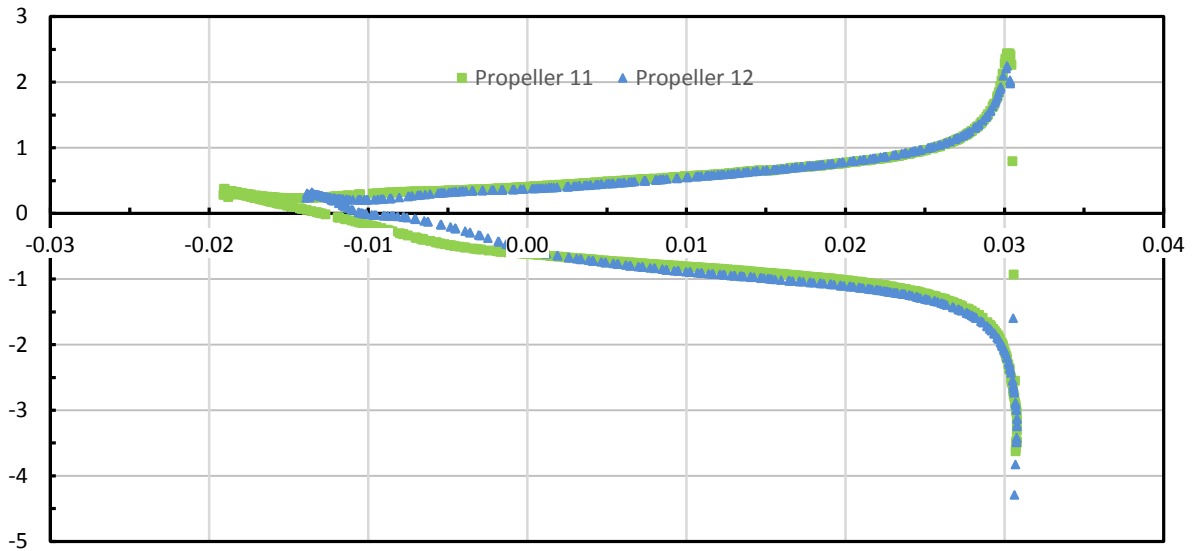
Figure 4.62 Pressure distribution along the blade section of propeller 11 and 12, section 0.5R
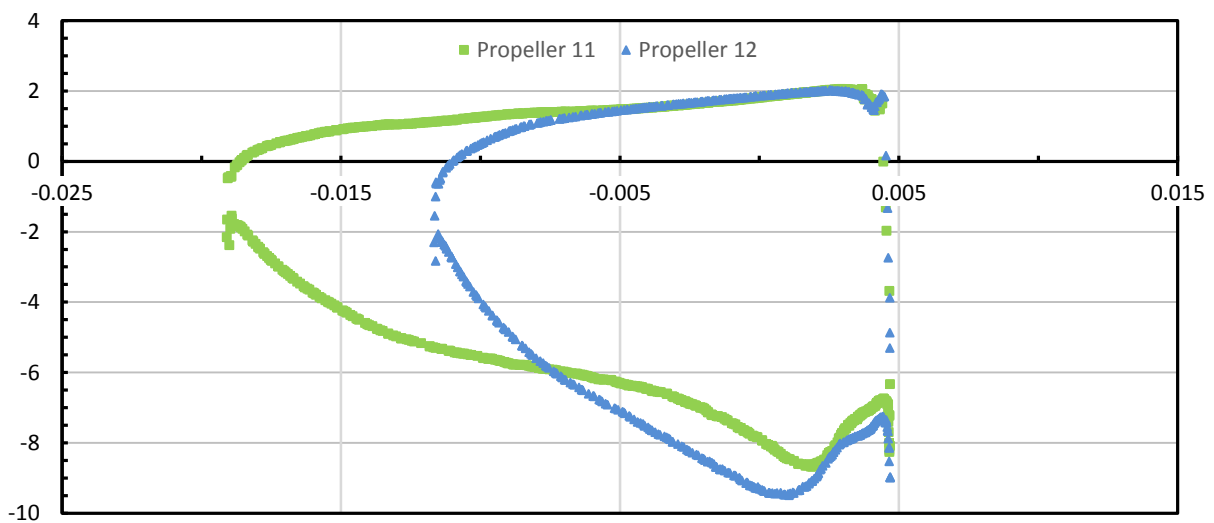
Figure 4.63 Pressure distribution along the blade section of propeller 11 and 12, section 0.95R

4.3 Experimental results VS numerical results

Towing tank test for the propeller P1374 (BAR 0.6) at model scale have been performed at April, 2014, by MARINTEK. These propellers are simulated under n=5, 9Hz. Table 4.4 lists the information of towing tank results.

Table 4.4 P1374 open water characteristics in towing tank

J	n=5 Hz			n=9 Hz		
	K_T	K_Q	η_0	K_T	K_Q	η_0
0	0.606	0.0924	0	0.611	0.0924	0
0.1	0.561	0.0867	0.103	0.568	0.0870	0.104
0.2	0.516	0.0809	0.203	0.523	0.0813	0.205
0.3	0.470	0.0751	0.299	0.475	0.0754	0.301
0.4	0.423	0.0693	0.388	0.426	0.0693	0.391
0.5	0.375	0.0635	0.470	0.376	0.0632	0.474
0.6	0.326	0.0572	0.543	0.326	0.0569	0.547
0.7	0.276	0.0507	0.608	0.277	0.0506	0.610
0.8	0.226	0.0442	0.652	0.228	0.0441	0.658
0.9	0.175	0.0372	0.673	0.178	0.0374	0.684
1.0	0.117	0.0289	0.642	0.126	0.0300	0.670
1.1	0.049	0.0191	0.450	0.069	0.0217	0.554

To validate the accuracy of numerical method, propeller P1374 at corresponding RPS were simulated. Table 4.5 lists the information of numerical results.

Table 4.5 P1374 open water characteristics from numerical simulation

J	n=5 Hz			n=9 Hz		
	K_T	K_Q	η_0	K_T	K_Q	η_0
0.1	0.561	0.0867	0.103	0.580	0.0909	0.102
0.3	0.516	0.0809	0.203	0.478	0.0770	0.296
0.5	0.470	0.0751	0.299	0.373	0.0634	0.468
0.7	0.423	0.0693	0.388	0.270	0.0500	0.602
0.9	0.375	0.0635	0.470	0.169	0.0364	0.665
1.1	0.326	0.0572	0.543	0.055	0.0204	0.472

4.4 Pressure and friction components

The three tables below list the pressure and friction component in propeller thrust and torque, respectively for propeller BAR 0.6. Data for propeller 0.4 and 0.8 can be found in Appendix D.

Table 4.6 Pressure and friction components in BAR 0.6, Model scale

J	**Thrust**	*Pressure*	*Friction*	**Torque**	*Pressure*	*Friction*
0.1	**0.5843**	0.5882	-0.00386	**0.0911**	0.08820	0.002858
0.3	**0.4804**	0.4845	-0.00409	**0.0770**	0.07396	0.003034
0.5	**0.3751**	0.3795	-0.00442	**0.0634**	0.06013	0.003251
0.7	**0.2723**	0.2770	-0.00471	**0.0501**	0.04669	0.003387
0.9	**0.1725**	0.1775	-0.00501	**0.0365**	0.03313	0.003370
1.1	**0.0583**	0.0638	-0.00550	**0.0204**	0.01699	0.003430

Table 4.7 Pressure and friction components in BAR 0.6, Full scale

J	**Thrust**	*Pressure*	*Friction*	**Torque**	*Pressure*	*Friction*
0.1	**0.5960**	0.5981	-0.00212	**0.0913**	0.08971	0.001555
0.3	**0.4937**	0.4960	-0.00230	**0.0776**	0.07590	0.001669
0.5	**0.3893**	0.3918	-0.00250	**0.0642**	0.06239	0.001801
0.7	**0.2876**	0.2903	-0.00268	**0.0510**	0.04915	0.001888
0.9	**0.1868**	0.1897	-0.00286	**0.0372**	0.03534	0.001883
1.1	**0.0724**	0.0755	-0.00312	**0.0210**	0.01911	0.001903

Table 4.8 Pressure and friction components in propeller 12, Model scale

J	**Thrust**	*Pressure*	*Friction*	**Torque**	*Pressure*	*Friction*
0.1	**0.5532**	0.5569	-0.00377	**0.08620**	0.08374	0.002436
0.3	**0.4617**	0.4657	-0.00399	**0.07387**	0.07125	0.002616
0.5	**0.3663**	0.3706	-0.00430	**0.06162**	0.05879	0.002833
0.7	**0.2706**	0.2752	-0.00462	**0.04920**	0.04625	0.002980
0.9	**0.1732**	0.1782	-0.00496	**0.03592**	0.03292	0.003005
1.1	**0.0628**	0.0682	-0.00540	**0.02021**	0.01716	0.003048

Table 4.9 Pressure and friction components in propeller 12, Full scale

	Thrust	*Pressure*	*Friction*	**Torque**	*Pressure*	*Friction*
0.1	**0.5631**	0.5651	-0.00202	**0.08631**	0.08500	0.001311
0.3	**0.4716**	0.4738	-0.00220	**0.07403**	0.07261	0.001424
0.5	**0.3773**	0.3797	-0.00239	**0.06202**	0.06047	0.001552
0.7	**0.2820**	0.2845	-0.00258	**0.04969**	0.04804	0.001645
0.9	**0.1848**	0.1876	-0.00279	**0.03636**	0.03469	0.001668
1.1	**0.0740**	0.0771	-0.00303	**0.02051**	0.01883	0.001679

The figure shows the pressure component in thrust, one can find pressure component is larger in full scale, this is the caused by the larger lift force in full scale. Friction component in thrust is negligible.
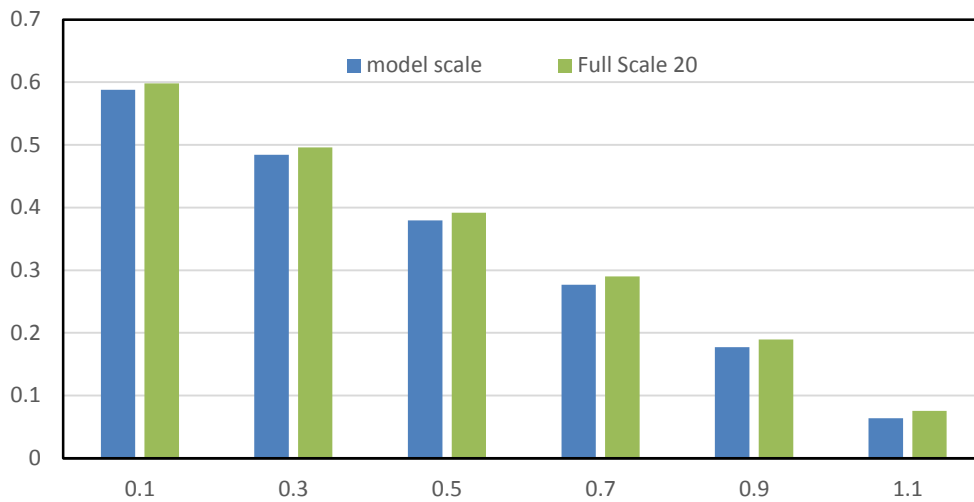

Figure 4.64 Pressure component in thrust, BAR 0.6

The figure shows the friction component in toque, one can find friction component is smaller in full scale, this is the caused by the smaller drag force in full scale, due to larger Re in full scale.
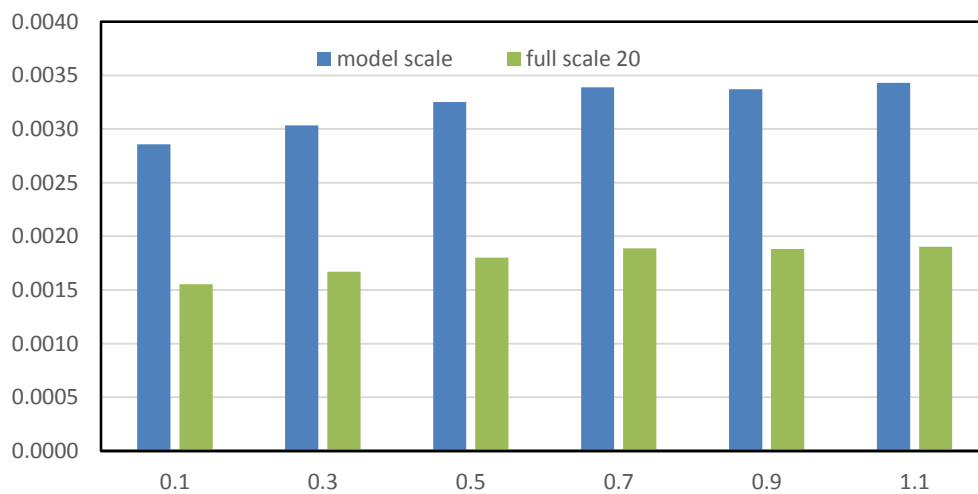

Figure 4.65 Friction component in torque, BAR 0.6

54

5. DISCUSSION

This Chapter presents the obtained numerical results and related analysis. Firstly, the CFD results will be compared with experimental data to validate the accuracy, then comes with the largest part of this chapter-the discussion of scale effects with respect to different factors.

5.1 Comparison between numerical and experimental results

The systematic simulations with propeller blade area ratio variation are performed by a RANSE method, which has already been introduced in detail in Chapter 3. The studied propellers in model scale are all simulated under n=15Hz by default. Open water tests in towing tank of parent propeller P1374 has been done by MARINTEK earlier with revolution speed n=5Hz and 9Hz, to compare the numerical results and validate its accuracy, propeller with the above two RPS are also calculated in this project with same RANSE method. The comparison between the numerical predictions and experimental data are presented below. For specific data at each J value, one can refer to the Table 4.4 and 4.5 in Chapter 4.
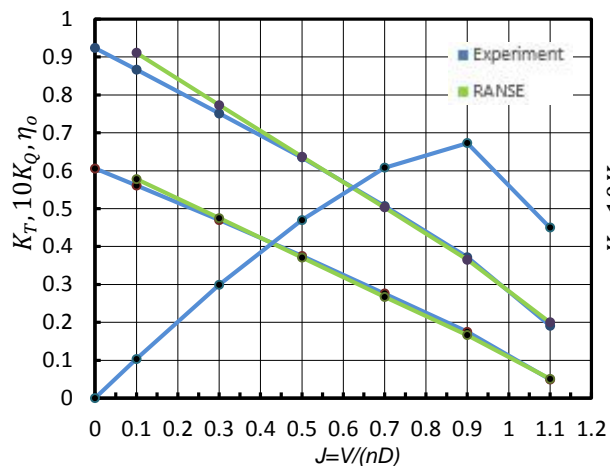
Figure5.1 Numerical and experimental results of at n=5Hz
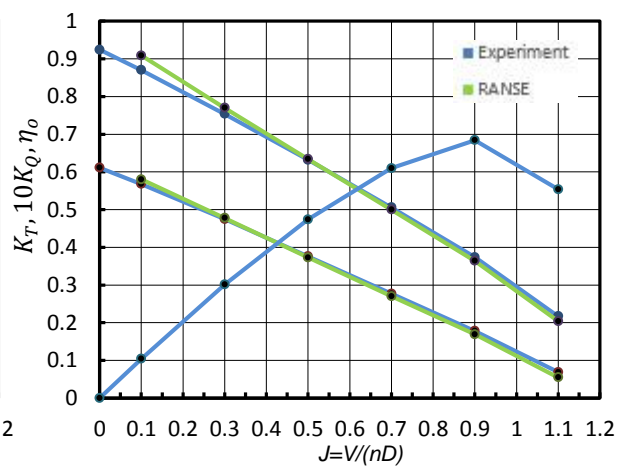
Figure5.2 Numerical and experimental results of at n=9Hz

The plots appear to be showing a good agreement between numerical and experimental results in all calculated loading conditions for both cases. Slightly larger deviation is observed at low J values with relative difference in forces listed below. Considering that maximum difference at J=0.1 in terms of torque is only about 5% and much more accurate results at higher loading conditions, the numerical results can be used with confidence.

Table 5.1 relative difference in force between numerical and experimental results

	J=0.1		J=0.3	
	ΔK_T	ΔK_Q	ΔK_T	ΔK_Q
n=5Hz	3.03%	5.07%	1.06%	2.93%
n=9Hz	2.11%	4.48%	0.63%	2.12%

The larger difference at heavy loading conditions is mainly caused by the flow separation phenomenon, which is more pronounced under heavy loading. Fig. 5.3 and 5.4 present the flow behavior at the blade section 0.9R for J=0.1 and J=1.1. It is clearly to see at the J=0.1, there is a strong flow separation region at the propeller leading edge, together with evident pressure drop. However at higher advance speed J, it is not found. From Fig.4.13-4.18, one can also find the flow separation is more pronounced at the outer blade section, under heavy loading.
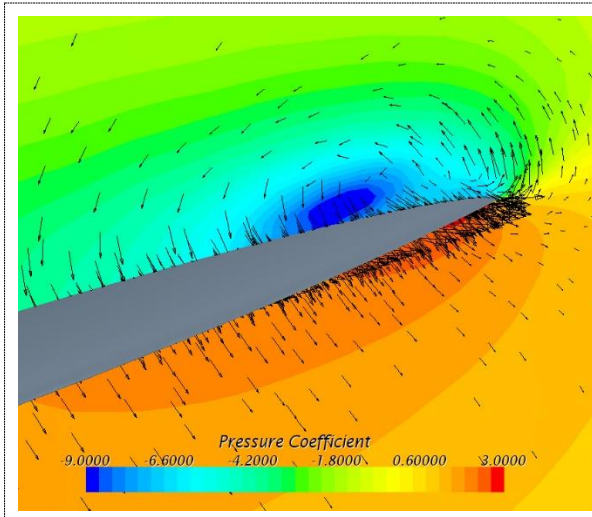
Figure 5.3 Flow field at 0.9R, J=0.1   **Figure 5.4 Flow field at 0.9R, J=1.1**
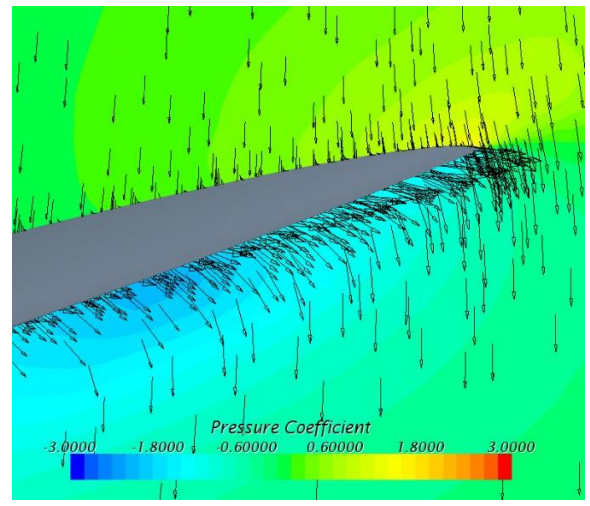
The observed physical result which gives rise to the considerable force oscillation during iteration is originated from separated leading edge vortex. It means that the flow case is essentially unsteady, and setup with periodicity conditions in the present simulation may not be sufficiently accurate (even though it was solved as unsteady, but we limit it to one blade passage domain with fully developed periodic interface). One way to improve the accuracy is to refrain from using periodicity conditions and use the whole 360 degrees domain instead. However this will be quite expensive for running systematic calculations.
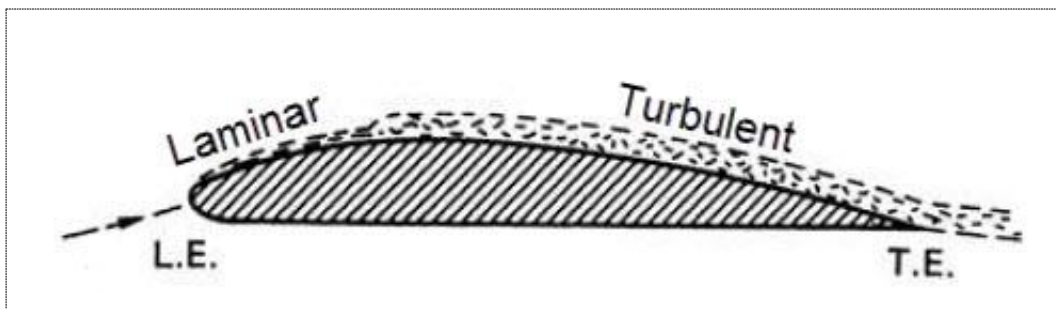
Figure5.5 Flow regime on the suction side of a propeller foil

Another factor that contributes to the difference between numerical and experimental results is laminar flow zone, which may exist on blades during towing tanks model tests as shown in Fig.5.5, while simulation with RANSE method assumes fully turbulent flow. The flow regime is determined by local Reynolds number, which varies greatly due to the complex geometry of propeller blade. As a result, it is impossible to completely avoid the transient flow regime.

5.2 General propeller open water characteristics

To investigate the scale effects with regard to blade area ratio, the systematically varied propellers with BAR 0.4, 0.6 and 0.8 were simulated in model and full scale. The rate of revolution for model-scaled propeller was 15Hz, while full-scaled propeller's revolution speed was defined by Froude number identity, resulting in n=3.3541Hz. Propeller Reynolds number is calculated using the blade width and the resultant velocity at section 0.7R, ignoring inflow.

$$R_e = 5 \cdot \frac{nD^2}{\upsilon} \cdot \frac{A_E}{A_0} \cdot \frac{1}{Z}$$
(5.1)

Table 5.2 Reynolds number of all simulated propellers

	BAR 0.4	**BAR 0.6**	**BAR 0.8**
Model scale	4.11×10^5	6.16×10^5	8.22×10^5
Full Scale	3.67×10^7	5.51×10^5	7.35×10^5

Figure 5.6 presents the obtained open water characteristics of model –scaled propellers. It can be seen at heavy loading condition, propeller with larger BAR has larger thrust and torque, and all the three propellers have comparable performance in terms of efficiency. However, at lighter loading condition, more specifically when J>0.7, propeller with BAR 0.4 generates the largest thrust, and torque. Propeller efficiency peaks at about advance coefficient J=0.9 for all the propellers. Thereafter, it falls evidently, and it is more pronounced for propeller BAR 0.8. The observed tendencies resemble those of Wageningen B-series with blade area ratio variation.
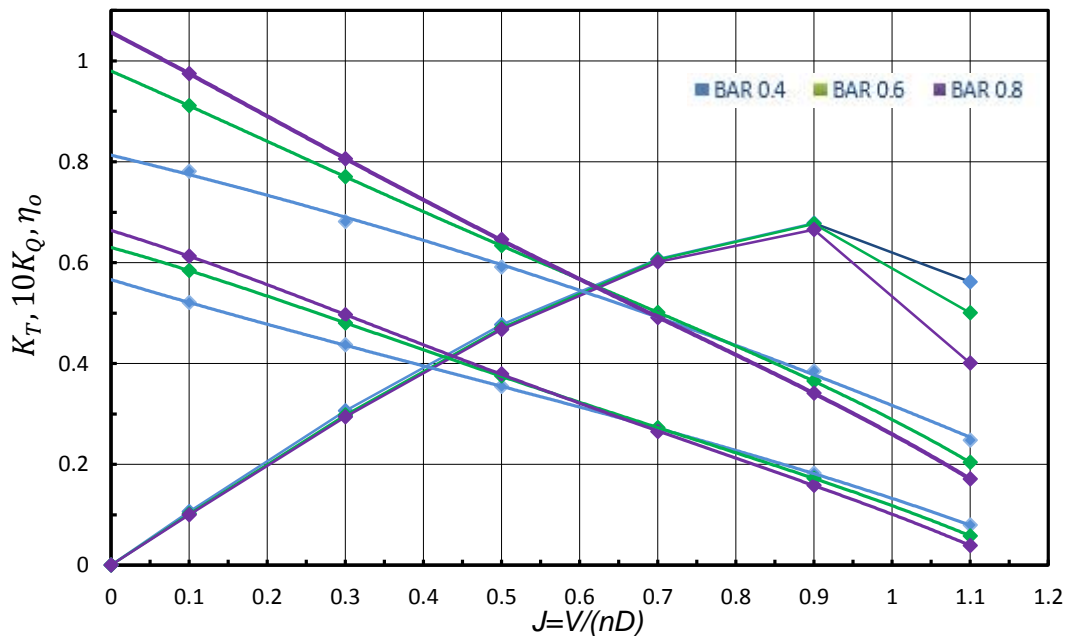
Figure 5.6 Open water characteristics of the propellers with BAR variation

Figure 4.7-4.9, in Chapter 4, presents the vorticity field in the propeller slipstream at various loading conditions, which illustrates a very logical tendency. With increasing J propeller loading becomes lighter, and propeller produces less vorticity in the flow. The figures also show that at heavier loading conditions (higher J) the rate of slipstream contraction and deformation of the vortex sheets are larger than at

lighter loading conditions. This contraction is due to the acceleration of the fluid by the propeller and, consequently, is dependent upon the thrust exerted by the propeller. The greater the thrust produced by the propeller for a given speed of advance, the more the slipstream will contract, according to John Carlton [8].

The following group of Figures 4.10-4.12 clearly illustrated that the blades of propeller with lower BAR develop a stronger tip vortex at low J values, than blades of propeller with higher BAR. This is related to the value of circulation and resulting blade loading, which are higher for propellers with lower BAR, at the same J value. Mainly this result is caused by a higher blade section thickness (relative thickness/chord length e_o/b_r was kept the same through the series). This result is also in line with experimental data on the well-known Wageningen B-series.

5.3 Scale effects

The comparison between model and full scale open water propeller characteristics was made in the form of relative difference in percent $\left((K_S - K_M)/K_M\right) \times 100$, and it is presented in Fig.5.7 and Fig.5.8, for thrust coefficient, torque coefficient respectively. One can find detailed data in Appendix B.
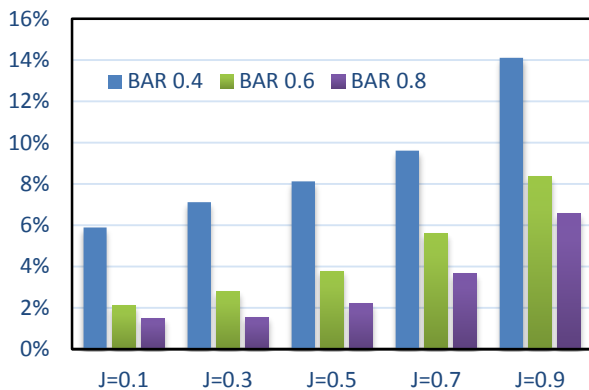
Figure 5.7 Relative difference in thrust　　**Figure 5.8 Relative difference in torque**
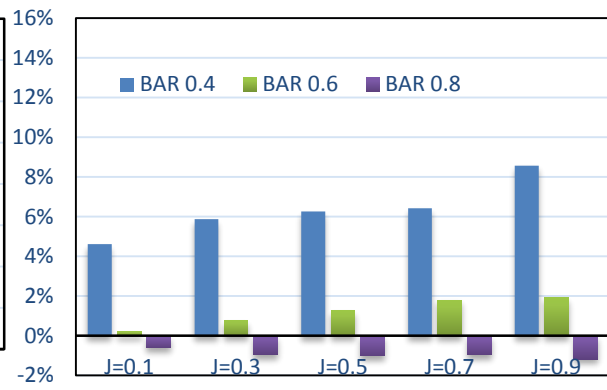
Compared the scale effects in propeller force, the following conclusions can be drawn:
Thrust coefficient of all propellers is larger in full scale, and the relative difference between model and full-scaled results is larger for smaller BAR. Propeller torque experiences the similar tendency, with the exception that the calculated torque coefficient is little bit smaller in full scale for BAR 0.8. Thus it can be concluded that the propeller with smallest BAR has the largest scale effects in open water characteristics. Meanwhile, it is obvious to see propeller torque shows a smaller scale effect than propeller thrust, and both of the thrust and torque related scale effects are larger at lighter loadings.

To investigate the above mentioned tendency, the contribution from the "pressure" and "friction" components in thrust and torque were assessed separately. The pressure component is originated from pressure differential between suction and pressure blade side, which generates the lift force. The friction component is caused by the viscosity, which forms the so called drag force. Both lift and drag force have

their contribution in propeller thrust and toque. For more information, one can refer to Part 2.1.2. Data of propeller BAR 0.6 in model and full scale are presented in Table 4.6-4.7, Chapter4.

5.3.1 Scale effects regarding propeller thrust and torque

Thrust coefficient

By comparing Table 4.6 and 4.7, Chapter 4, it can be noted both pressure and friction component in thrust have a positive effect on the thrust increase in full scale, this was caused by the increase of lift force F_L and the decrease of drag force F_D in full scale. According to the Eq. 2.1.5, the propeller thrust is affected by $(1 - \frac{F_D}{F_L} \cdot tan\,\beta_i)$, hence the described change of lift and drag force will have a co-acting effect on the thrust, which makes the scale effect more pronounced.

Torque coefficient

In the case of propeller torque, according to the Eq. 2.1.6, it is affected by $(1 + \frac{F_D}{F_L} \cdot \cot\beta_i)$, the increase of lift force F_L and the decrease of drag force F_D will have a counter-acting effect. This is why scale effect is smaller for propeller torque. Besides, propeller torque magnitude is about one order less than thrust, and relative contribution of drag forces (friction component) is much greater in torque than it is in thrust.

5.3.2 Scale effects regarding loading condition

Thrust coefficient

From Figure 5.7-5.8, it can be seen at lighter loading condition (higher J value), the relative difference of thrust and torque between model and full scale is, generally, larger. In the case of propeller thrust, since the contribution of friction component is comparatively small, it is justified to say that the greatest part of scale effects on thrust is associated with pressure component. Table 5.3 presents the absolute and relative difference of pressure component in thrust between model and full scale. It was found that the absolute increase value is comparable through all the loading conditions, however since at higher J value, we are dealing with relative smaller absolute value of pressure component, and division by a small value results in larger difference in percent. Therefore, it can be concluded, at higher J, the larger increase of thrust between model and full scale is attributed to the relative larger contribution of pressure component.

Table 5.3 Pressure component in thrust, model and full scale, BAR 0.6

J	MS	FS	Absolute increase	Relative increase
0.1	0.5882	0.5981	0.0099	1.7%
0.3	0.4845	0.4960	0.0115	2.4%
0.5	0.3795	0.3918	0.0123	3.2%
0.7	0.2770	0.2903	0.0133	4.8%
0.9	0.1775	0.1897	0.0122	6.9%

Torque coefficient

Compared to the propeller thrust, contribution of friction component is considerable larger in torque, due to the smaller value of torque. Take propeller with BAR 0.8 for example. From Table 5.4, it can be seen that at each loading condition the friction component is reduced in full scale. Due to the larger contribution of friction component, the total torque thus experiences a decrease in full scale, despite pressure component increased in full scale. At lighter loading condition, where friction contribution in the total force balance is even larger, the decrease of torque is therefore more evident.

Table 5.4 Pressure and friction component in torque, model and full scale, BAR 0.8

J	*Model scale*			*Full Scale*		
	Torque	*Pressure*	*Friction*	***Torque***	*Pressure*	*Friction*
0.1	**0.09747**	0.09391	0.003564	**0.09689**	0.09494	0.001949
0.3	**0.08060**	0.07686	0.003714	**0.07982**	0.07775	0.002076
0.5	**0.06456**	0.06061	0.003954	**0.06390**	0.06166	0.002238
0.7	**0.04909**	0.04493	0.004157	**0.04862**	0.04624	0.002375
0.9	**0.03413**	0.02994	0.004190	**0.03373**	0.03134	0.002392

For propeller with BAR 0.4 and 0.6, the increase of pressure component in full scale is larger than the decrease of the friction component, hence the resulted toque coefficient is higher in full scale. However, from Figure 5.8, one can find the increase of torque in full scale becomes less dependent on the loading condition (compared to propeller thrust), this is the direct result of larger counter-acting effect of friction component at lighter loading condition (higher J value). The conclusion is easily verified by the following analysis. As one can find from the Table 5.5, compared to J=0.3, the relative contribution of pressure component in torque at J=0.7 is augmented by the value of 1.5% (8.8%-7.3%). However, since the contribution of friction is larger at J=0.7, the scale effect in terms of torque is ultimately only increased by 0.6% (6.4%-5.8%) between J=0.3 and J= 0.7.

Table 5.5 Pressure and friction component in torque of BAR 0.4, at J=0.3, 0.7

	J=0.3			J=0.7		
	MS	*FS*		*MS*	*FS*	
Total	0.0681	0.0721	5.8%	0.0498	0.0530	6.4%
Pressure	0.06583	0.07081	7.3%	0.04725	0.05167	8.8%
Friction	0.002289	0.001236	-1.5%	0.00255	0.001360	-2.4%

In conclusion, the main difference in torque between model and full scale with varied loading condition is again attributed to pressure component. In the meantime the torque-related scale effect shows weak dependence on loading condition, this is caused by the larger contribution of drag force in torque, which also gives rise to the reduction of torque at full scale, for propeller with BAR 0.8.

5.3.3 Scale effects regarding blade area ratio

Thrust coefficient

From Figure 5.7, it is obvious to find the difference of thrust between model and full scale is larger for propeller BAR 0.4. As mentioned earlier, compared to model scale, thrust is larger in full scale, due to its larger pressure component, resulted from larger lift force in full scale. Since the thrust-related scale effect is more pronounced in BAR 0.4, it is logical to say the difference of pressure component in thrust between model and full scale should be largest for propeller with BAR 0.4. Table 5.6 below demonstrates the tendency and one can find, with higher blade area ratio, the increase of pressure component in full scale is larger.

Table 5.6 Pressure component in thrust compared with varied BAR

	BAR 0.4			BAR 0.6			BAR 0.8		
J	MS	FS	Increase	MS	FS	Increase	MS	FS	Increase
0.1	0.5236	0.5531	5.6%	0.5882	0.5981	1.7%	0.6178	0.6246	1.1%
0.3	0.4398	0.4695	6.8%	0.4845	0.4960	2.4%	0.5015	0.5069	1.1%
0.5	0.3573	0.3848	7.7%	0.3795	0.3918	3.2%	0.3848	0.3907	1.5%
0.7	0.2746	0.2994	9.0%	0.2770	0.2903	4.8%	0.2709	0.2781	2.7%
0.9	0.1859	0.2101	13.0%	0.1775	0.1897	6.9%	0.1646	0.1724	4.7%

Regarding the pressure component, the pressure distribution at cylinder section 0.7R in model and full scale are compared in Figure 4.19-4.24. It can be seen that the pressure distribution in the flow field around the target blade section undergoes much larger change for the propeller with BAR0.4 than for the propeller with BAR0.8. Hence the section lift force F_L undergoes larger change in full scale for the BAR 0.4, which explains the aforementioned tendency of pressure component in thrust. One can also find in the Appendix C, pressure distribution at cylinder section 0.9R also undergoes the same tendency, the pressure variation in full scale is largest for BAR 0.4.

Since propeller lift force is affected by the flow behaviour significantly, it is necessary to look into the flow patterns around propeller blade. Figure 4.25-30 present constrained streamlines with pressure distribution on propeller suction blade for the three propellers in model and full scale. It can be seen that in model scale all propellers have pronounced zone of flow in radial direction along the blade trailing edge. This zone is largest for propeller with BAR 0.4. In full scale, the zone of trailing edge radial flow is reduced, and the reduction is again largest for propeller with BAR 0.4. The trailing edge flow pattern affects directly the pitch of trailing vortices in propeller slipstream, as shown in Part 4.1.11. In full scale, the reduction of radial flow results in increase of trailing vortex pitch and higher lift force produced by the blade. Therefore, this is the most likely major factor contributing to the magnitude of scale effect.

Concerning the results described above, it can be concluded that due to less pronounced trailing edge radial flow region, higher lift force is produced in full scale. The increase of lift in full scale is largest for propeller with BAR 0.4, which is caused by the largest reduction of trailing edge radial flow zone.

The observed tendency in trailing edge radial flow is believed to be associated with the corresponding change of boundary layer thickness in full scale. According to the definition for turbulent boundary layer thickness over a flat plate, Reference [11], the boundary layer thickness δ is given by:

$$\delta \approx \frac{0.382 \cdot x}{Re_x^{1/5}}$$

(5.2)

where x is the distance downstream from the start of the boundary layer, $Re_x = \mu_0 x / \nu$ is the local Reynolds number. Though the definition is designed for flat plate, it does show the correlation between boundary layer thickness and Reynolds number, which can be also applied in the case of propeller. More specifically, boundary layer thickness is reduced and has a greater "fullness" of velocity profiles in full scale due to large Reynolds number, as shown in Figure 5.9. By virtue of these changes, the full scale boundary layer on propeller blades become more resistant to the action of centrifugal forces, which tend to drive the flow in the outward, radial direction, as we see in model scale. Figure 4.37-4.42 also demonstrate the tendency of change in boundary layer thickness. The boundary layer is thicker in model scale, and reduced in full scale. The reduction of thickness is more pronounced for BAR 0.4.

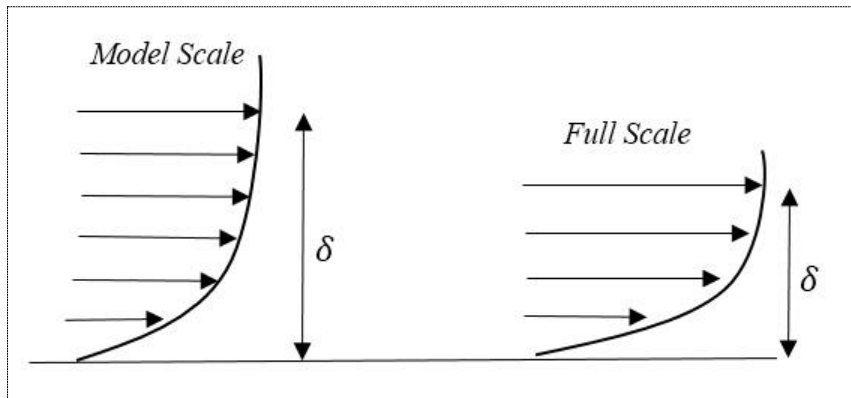**Figure 5.9 Boundary layer profile in model and full scale**
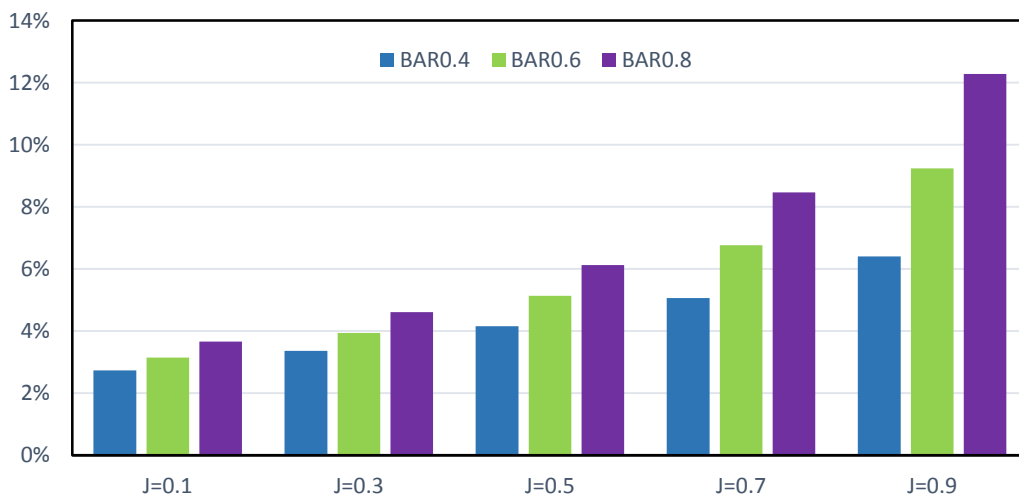
Torque coefficient

Figure 5.10 Friction component weightage (%) in propeller torque

Since lift force is larger in full scale and the increase is largest in propeller with BAR 0.4, it is logical to find the largest scale effects in terms of torque for BAR 0.4, due to the dominant contribution of lift force

in torque. However, for larger BAR, the lift increase in full scale will be smaller. Meanwhile, the counter-acting drag force will increase its weightage in torque due to larger blade area, as shown in Figure 5.10. These two coupling factors thus together make the increase of torque smaller in full scale for larger BAR. Further evolvement of this tendency in BAR 0.8 results in the decrease of torque in full scale.

5.3.4 Scale effects regarding chord length distribution

Apart from the series of blade area ratio variation, calculation were carried out for another variant propeller 12 with alternative chord length distribution. Compared to propeller 11(with BAR 0.6) used in the previous stage, the chord length distribution is altered in the new one and maximum thickness to chord length ratio e_o/b is modified slightly at the outer blade sections, in order to ensure a more realistic blade geometry. All the other geometrical elements are kept identical in Propeller 11 and Propeller 12.

The calculated open water characteristics of propeller 12 is provided in Table 4.3 and if one compare it with propeller 11 as shown in Figure.4.50, it can be noted that propeller 12 has lower thrust and torque all through the loading conditions, with exception of slightly higher thrust at J=1.1. Performance in terms of efficiency are quite close for these two propeller.
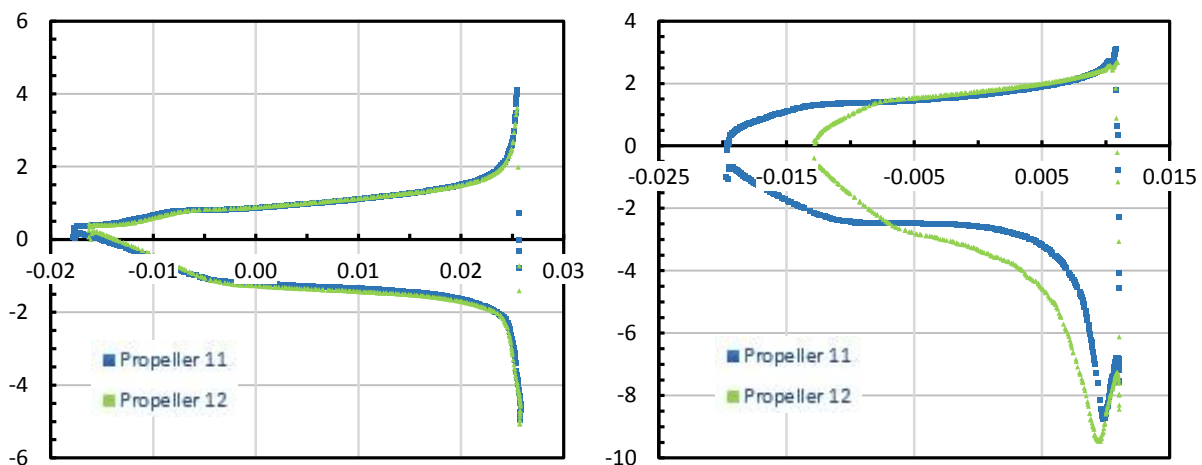
Figure 5.11 Pressure coefficient distribution along blade section 0.7R and 0.9R, J=0.1

Figure 5.11 presents the chordwise pressure distributions of these two propellers at section 0.7R and 0.9R respectively, for advance coefficient J=0.1. Data of section 0.4R and 0.5R can be found in Figure 4.61-4.63, in Chapter 4. It can be seen that the difference of pressure distribution between propeller 11 and 12 is much more pronounced at section 0.9R and 0.95R at blade tip area, when compared to other inner sections.

The blade flow pattern of these two propellers are compared in Figure 5.12, it's obvious to see apart from the pressure distribution, the alternative chord length distribution also has a direct impact on the trailing edge radial flow zone, which is reduced significantly in propeller 12. In the meantime, one can find the reduction of trailing edge radial flow zone in full scale is smaller for propeller 12 in Figure 4.57-4.60, Chapter 4. Analogous to the BAR variation, it results in less augment of lift force in full scale, hence the scale effect in terms of propeller force should be less pronounced in propeller 12.

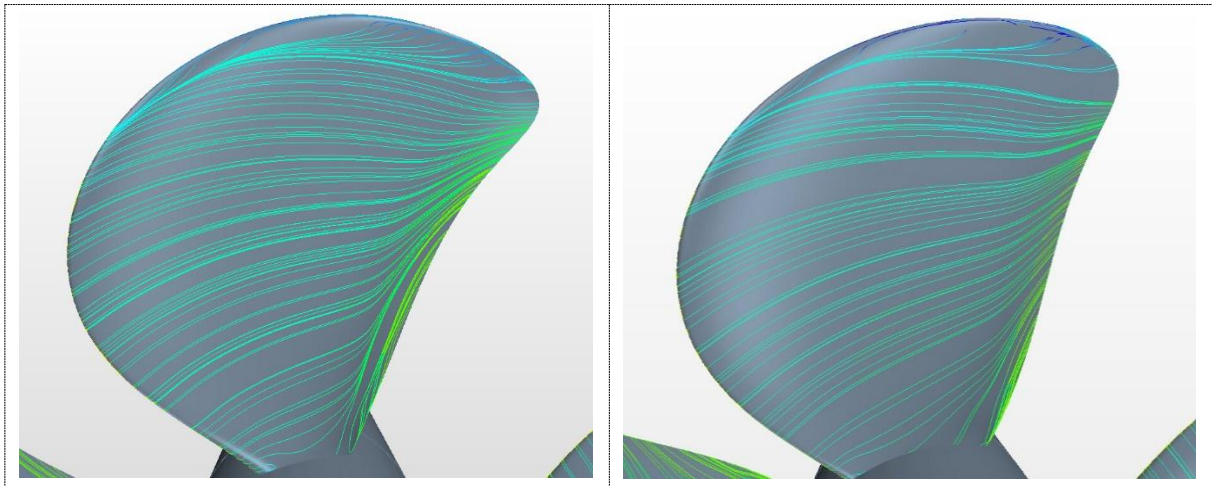**Figure 5.12 Comparison of flow pattern of propeller 11 and 12, model scale, J=0.5**

Figure 5.13 demonstrates the relative difference of thrust and torque between model and full scale, for propeller 11 and 12, and one can find the scale effect is reasonably higher in propeller 11, either for thrust or torque.
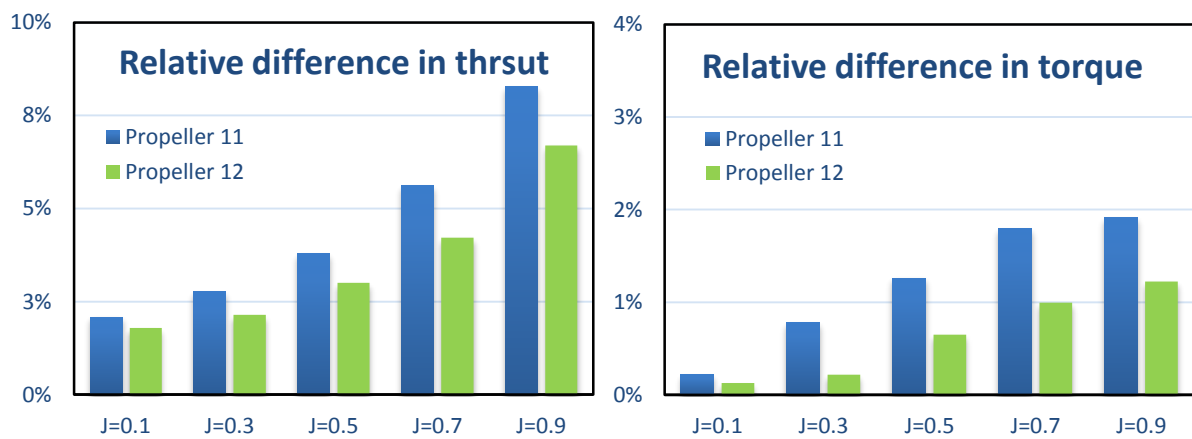

Figure 5.13 Scale effects in terms of thrust and torque coefficient for propeller 11 and 12

6. CONLUSION

To investigate the scale effect on propeller, the present study has analyzed a number of propellers with systematically varied blade area ratio, utilizing a RANS method with highly automatically generated mesh, in fully turbulent flow. Compared to experimental results, good agreement is obtained by the numerical simulation, though slightly larger difference is observed at heavy loading condition due to flow separation and laminar flow zone.

The calculated open water characteristics for propellers with BAR 0.4, 0.6 and 0.8 show the same tendencies as found in the well-known Wageningen B-series propellers with corresponding variation of blade area ratio.

The obtained scale effects is apparently larger for propeller thrust, this result is due to the counter-acting influence of lift and drag in torque, compared to co-acting influence in thrust. Besides, contribution of viscous forces in torque in much larger than in thrust, and the tendency becomes more pronounced at lighter loading conditions, which also makes the scale effect on torque less depend on loading condition, due to the larger neutralization from viscous force.

It has been shown that propeller with smallest blade area ratio has the largest scale effect, which is explained by the largest reduction of trailing edge radial flow zone in full scale for propeller BAR 0.4. It is induced by the large difference of Reynolds number in model and full scale, which implies that the full scale boundary layer on propeller blades become more resistant to the action of centrifugal forces, which tend to drive the flow in the outward, radial direction. In the case of propeller torque, the counter-acting viscous force is much larger in the total force balance, and it is more pronounced for larger blade area, which explains the even smaller scale effect on propeller torque with larger blade area ratio.

The results of propeller with alternative chord length distribution appears to be showing smaller scale effect when compared to the original one with BAR 0.6. The reduced trailing edge radial flow zone due to changed blade geometry is responsible for these results.

The study based on computational results indicates that the influence of blade area ratio on scale effects are primarily due to the Reynolds-affected trailing edge radial flow phenomenon, and it is highly dependent on the blade geometry. These make the traditional scaling extrapolation procedure significantly complicate, thus it requires further exploration into the practical CFD methods for the accurate prediction of propeller performance.

7. FUTURE WORK

The present work utilizes periodical boundary setting to represent the whole CFD domain, this setting will reduce computational cost significantly especially for the systematic calculation. However, it inevitably brings a relative larger error at heavy loading condition due to flow separation. One of works that can be done in future is to calculate the cases at low J values with the whole 360 degree domain. Estimated mesh cells will reach to about 5 million, which requires greater computational resources.

As mentioned earlier, the work was solved under the assumption of fully turbulent flow regime, in both full and model scale condition, although the latter case can, in principal, involve transient flow regime. In order to improve the accuracy of prediction in model scale, one can consider the prediction of open water propulsor characteristics with more advanced transition model, while the artificial means of flow turbulization are not applied routinely. The two-equation, isotropic SST k-ω model selected in the present project, it already provided us reasonable accuracy. However, as far as the problems described here is concerned, more advanced turbulence modelling concepts such as anisotropic turbulence models, Detached Eddy Simulation (DES) and vortex confined method appear to be more appealing. In comparison with traditional turbulence modelling methods, the latter approaches have been studied far less completely, further development of these models are deemed to have great contribution to CFD methods for marine applications.

The general recommendation that being followed in the present work for prism layer mesh setup is to aim at y^+<5 in model scale simulations, and 30<y^+<300 in full scale simulations. Using the All y^+ Treatment method to relax the above limits. This means that, if some surface areas fall in the "buffer" range (5<y^+<30), it is possible to go on with the simulation and expect reasonable results. Even for simulation with scale factor 10, this setup bring decent result, as most important outer blade sections r/R>0.6 are well in the range of y^+>30. However, what if, for example, we do a calculation at the scale factor 5? One can expect that, in such a case, most of the blade will be in the buffer layer. Whatever we believe about the All y^+ Treatment method, this is the situation better to be avoided. Hence, it would be constructive to derive a more general recommendation for setting up the boundary layer mesh valid for all scales.

REFERENCES

67

[1]   Krasilnikov,V.I., Sun, J., and Halse, K.H. CFD investigation in scale effect on propellers with different magnitude of skew in turbulent flow. In: First International Symposium on Marine Propulsors, Trondheim, Norway, 2009.

[2]   Abdel-Maksoud, M., and Heinke, H.-J. Scale effects on ducted propellers. In: Proceedings of the 24th ONR Symposium on Naval Hydrodynamics, Fukuoka, Japan, 2002.

[3]   Krasilnikov,V.I., Sun, J., Zhang, Z., and Hong, F. Mesh generation technique for the analysis of ducted propellers using a commercial RANSE solver and its application to scale effect study. In: 10th Numerical Towing Tank Symposium, Hamburg, German, 2007.

[4]   AB VOLVO PENTA. *Inboard propellers and speed calculation*

[5]   John D. Anderson. *Computational fluid dynamics (the basics with applications)*

[6]   Krasilnikov,V.I. *First introduction into computational fluid dynamics for marine application, Lecture notes*, Ålesund University College, 2011

[7]   http://en.wikipedia.org/wiki/SST_%28Menter%E2%80%99s_Shear_Stress_Transport%29

[8]   http://www.cd-adapco.com/products/star-ccm%C2%AE

[9]   CD-adapco, STAR-CCM+ User Guide version 10.02, 2015

[10]   http://www.arc.vt.edu/ansys_help/flu_th/flu_th_sec_rotate_equations.html

[11]   http://en.wikipedia.org/wiki/Boundary_layer_thickness#99.25_Boundary_Layer_thickness

APPENDIX

Appendix A   Geometrical characteristics of propeller (BAR 0.6) with alternative chord length distribution

Table A1 Chord length and maximum thickness distribution of propeller (BAR 0.6) with alternative chord length distribution

r/R	b_r/R	b_r/b(0.7)	e_o/R	e_o/b_r
0.240	0.4171	0.5574	0.0761	0.1824
0.250	0.4311	0.5761	0.0750	0.1739
0.300	0.4972	0.6644	0.0694	0.1395
0.350	0.5569	0.7442	0.0640	0.1149
0.400	0.6098	0.8149	0.0588	0.0964
0.500	0.6932	0.9263	0.0490	0.0706
0.600	0.7420	0.9915	0.0400	0.0539
0.700	0.7483	1.0000	0.0312	0.0416
0.800	0.6973	0.9318	0.0228	0.0326
0.900	0.5541	0.7404	0.0144	0.0259
0.950	0.4133	0.5523	0.0100	0.0241
0.975	0.2999	0.4008	0.0080	0.0266
0.990	0.1926	0.2573	0.0069	0.0358
0.995	0.1368	0.1829	0.0064	0.0467
1.000	0.0500	0.0668	0.0060	0.1200

Appendix B   Relative difference in thrust and torque

Table D1 Relative difference in thrust and torque between model and full scale

	Relative difference in thrust			Relative difference in torque		
J	BAR 0.4	BAR 0.6	BAR 0.8	BAR 0.4	BAR 0.6	BAR 0.8
0.1	5.9%	2.1%	1.5%	4.6%	0.7%	-0.56%
0.3	7.1%	2.8%	1.6%	5.9%	1.2%	-0.94%
0.5	8.1%	3.8%	2.2%	6.3%	1.6%	-1.02%
0.7	9.6%	5.6%	3.7%	6.4%	2.4%	-0.96%
0.9	14.1%	8.4%	6.6%	8.6%	2.8%	-1.17%

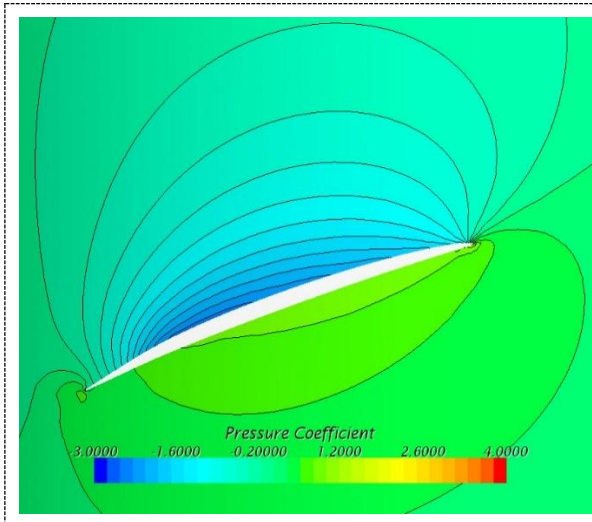Appendix C   Pressure distribution at cylinder section 0.9R

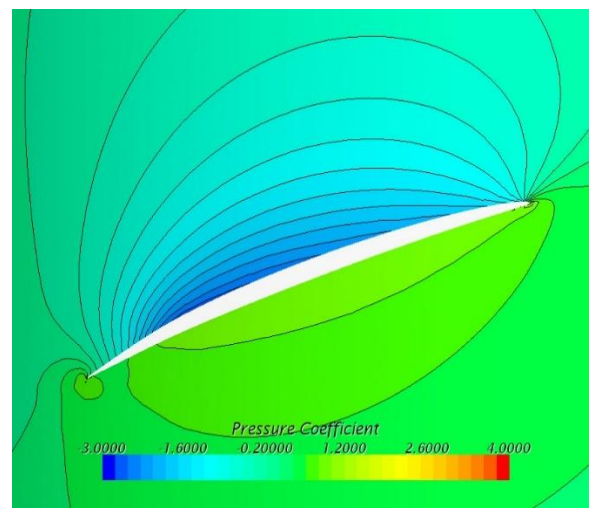
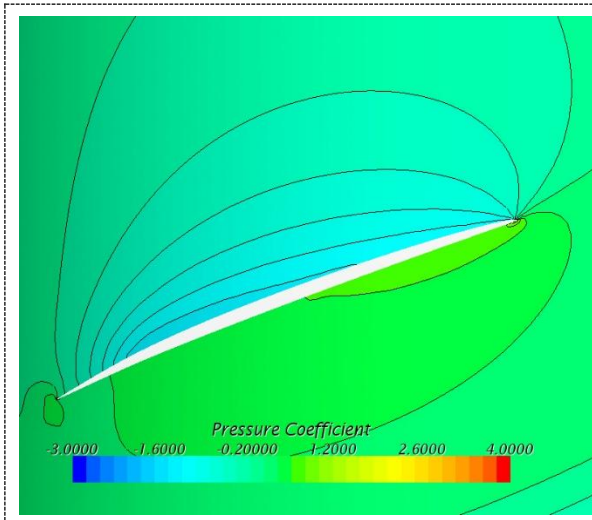**Figure B1 BAR 0.4, Model Scale**

Figure B2 BAR 0.4, Full Scale

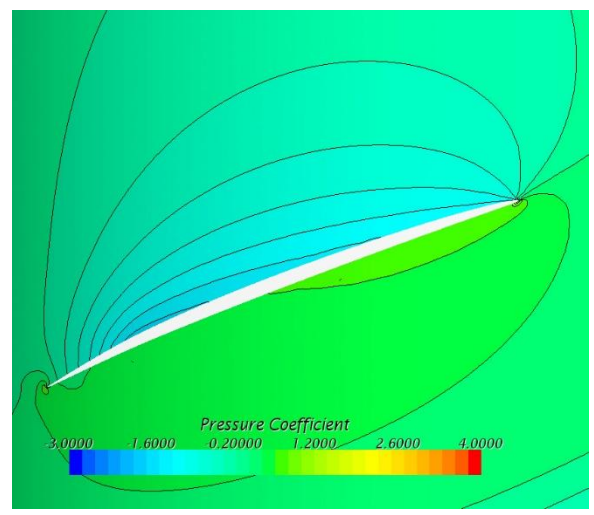**Figure B3 BAR 0.6, Model Scale**

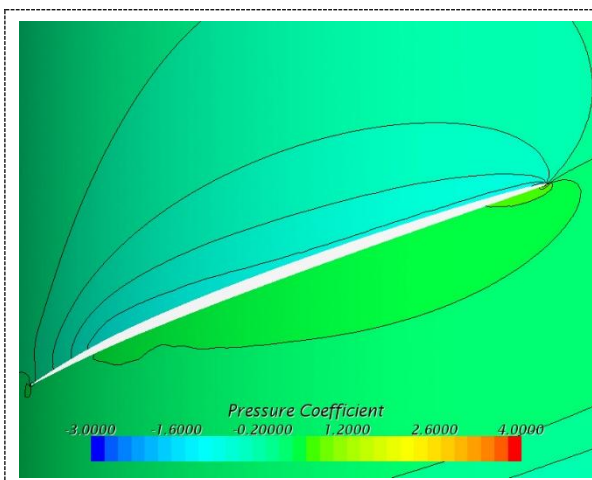**Figure B4 BAR 0.6, Full Scale**

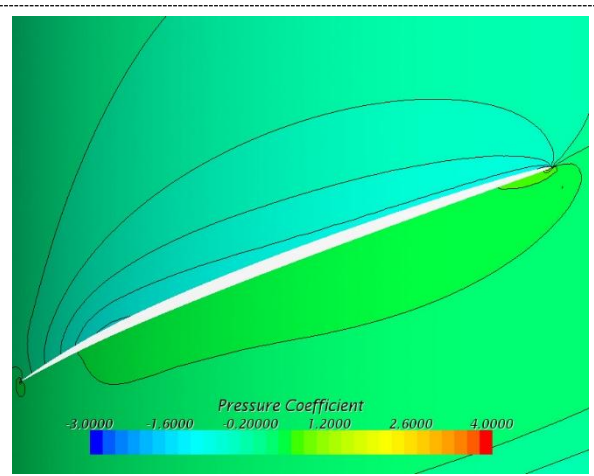**Figure B5 BAR 0.8, Model Scale**

Figure B6 BAR 0.8, Full Scale

Appendix D   Pressure and friction component in model and full scale, for BAR 0.4 and 0.8

Table C1 Pressure and friction components in BAR 0.4, Model scale

J	**Thrust**	*Pressure*	*Friction*	**Torque**	*Pressure*	*Friction*
0.1	**0.5208**	0.5236	0.00276	**0.0781**	0.07598	0.002132
0.3	**0.4369**	0.4398	0.00294	**0.0681**	0.06583	0.002289
0.5	**0.3542**	0.3573	0.00319	**0.0591**	0.05669	0.002456
0.7	**0.2713**	0.2746	0.00337	**0.0498**	0.04725	0.002519
0.9	**0.1822**	0.1859	0.00370	**0.0385**	0.03608	0.002463
1.1	**0.0796**	0.0837	0.00411	**0.0248**	0.02239	0.002397

Table C2 Pressure and friction components in BAR 0.4, Full scale

J	**Thrust**	*Pressure*	*Friction*	**Torque**	*Pressure*	*Friction*
0.1	**0.5515**	0.5531	0.00153	**0.0817**	0.08055	0.001149
0.3	**0.4679**	0.4695	0.00165	**0.0721**	0.07081	0.001236
0.5	**0.3830**	0.3848	0.00181	**0.0628**	0.06150	0.001330
0.7	**0.2974**	0.2994	0.00196	**0.0530**	0.05167	0.001360
0.9	**0.2079**	0.2101	0.00216	**0.0418**	0.04047	0.001341
1.1	**0.1037**	0.1061	0.00239	**0.0278**	0.02652	0.001310

Table C3 Pressure and friction components in BAR 0.8, Model scale

J	**Thrust**	*Pressure*	*Friction*	**Torque**	*Pressure*	*Friction*
0.1	**0.6130**	0.6178	0.00484	**0.09747**	0.09391	0.003564
0.3	**0.4964**	0.5015	0.00508	**0.08060**	0.07686	0.003714
0.5	**0.3794**	0.3848	0.00544	**0.06456**	0.06061	0.003954
0.7	**0.2651**	0.2709	0.00581	**0.04909**	0.04493	0.004157
0.9	**0.1585**	0.1646	0.00615	**0.03413**	0.02994	0.004190
1.1	**0.0391**	0.0458	0.00673	**0.01708**	0.01271	0.004372

Table C4 Pressure and friction components in BAR 0.8, Full scale

J	**Thrust**	*Pressure*	*Friction*	**Torque**	*Pressure*	*Friction*
0.1	**0.6220**	0.6246	0.00262	**0.09689**	0.09494	0.001949
0.3	**0.5041**	0.5069	0.00281	**0.07982**	0.07775	0.002076
0.5	**0.3877**	0.3907	0.00308	**0.06390**	0.06166	0.002238
0.7	**0.2748**	0.2781	0.00331	**0.04862**	0.04624	0.002375
0.9	**0.1689**	0.1724	0.00351	**0.03373**	0.03134	0.002392
1.1	**0.0504**	0.0542	0.00383	**0.01668**	0.01421	0.002471